

Universitas Carolina
Facultas Mathematica Physicae

DOCTORAL THESIS



RNDr. Daniel Duda

Quantum turbulence in superfluid helium studied by particle tracking velocimetry visualization technique

Department of Low Temperature Physics

Supervisor: prof. RNDr. Ladislav Skrbek, DrSc.

Field of Study: Physics

Specialization: Condensed Matter and Material Research

Praha 2017

Prohlašuji, že jsem tuto disertační práci vypracoval samostatně a výhradně s použitím citovaných pramenů, literatury a dalších odborných zdrojů.

Beru na vědomí, že se na moji práci vztahují práva a povinnosti vyplývající ze zákona č. 121/2000 Sb., autorského zákona v platném znění, zejména skutečnost, že Univerzita Karlova v Praze má právo na uzavření licenční smlouvy o užití této práce jako školního díla podle §60 odst. 1 autorského zákona.

V dne

Podpis autora

Název práce: Kvantová turbulence v supratekutém héliu studovaná vizualizačními metodami

Autor: RNDr. Daniel Duda

Katedra: Katedra fyziky nízkých teplot

Vedoucí: prof. RNDr. Ladislav Skrbek, DrSc.

Abstrakt: Oscilační proudění v supratekutém a normálním héliu byla zkoumána vizualizační metodou *sledování trasovacích částic* pevného deuteria o mikrometrové velikosti se zaměřením na míru podobnosti či rozdílnosti mezi He I, které je klasickou viskózní kapalinou, a He II, jež je supratekuté a jehož cirkulace je kvantovaná. V práci jsou popsány výsledky trojice experimentů: úplav za relativně pomalu kmitající překážkou s relativně velkým rozkmitem (srovnatelným s velikostí překážky), stacionární proudění (*angl.*: „streaming“) v okolí rychle kmitající křemenné ladičky s nízkou amplitudou (vzhledem k její velikosti) a kavitace v okolí jiné rychle kmitající křemenné ladičky. Hlavním výsledkem je pozorování, že odpovídající proudění v He I a II si jsou na velkých měřítkách vzájemně podobná, zatímco na malých vykazují naprosto rozdílné statistické vlastnosti. Navíc v případě He II jsou tyto statistické vlastnosti *univerzální* ve smyslu nezávislosti na druhu zkoumaného proudění a jsou stejné jako v případě *tepelného protiproudu* supratekuté a normální složky He II, což je kvantový druh tepelné konvekce nepřípodobitelný k žádnému druhu konvekce kapalin klasických.

Klíčová slova: Experiment Hélium Kvantová turbulence Supratekutost Vizualizace proudění Kmitající překážka Pseudovířivost Délková měřítka Univerzalita Stacionární část oscilačního proudění Křemenná ladička Kavitace Oscilační úplav

Title: Quantum turbulence in superfluid helium studied by particle tracking velocimetry visualization technique

Author: RNDr. Daniel Duda

Department: Department of Low Temperature Physics

Supervisor: prof. RNDr. Ladislav Skrbek, DrSc.

Abstract: The Particle Tracking Velocimetry visualization technique using micrometer size solid deuterium particles as tracers has been applied to study oscillatory flows of He II, which is a quantum fluid with quantized vorticity, as well as flows of He I, which is a classical viscous liquid, focusing on the similarities and differences between the quantum and classical flows. Three experiments are described: the flow past a large-amplitude low-frequency oscillating obstacle in the form of a prism; the steady streaming flow due to a small-amplitude large-frequency oscillating quartz tuning fork - a widely used tool to study quantum turbulence; and the production of *cavitation* in the vicinity of a fast-oscillating tuning fork. The main outcome is the observation that these flows are similar in He I and in He II at large length-scales, whereas at small scales, they exhibit totally different statistical properties. Moreover, in He II, these small scale statistical properties are universal in that they do not depend on the type of the imposed mean flow of the superfluid and normal component and are the same as in thermal counterflow – a pure quantum type of thermal convection with no classical counterpart.

Keywords: Experiment Helium Quantum turbulence Superfluidity Flow visualization Oscillating obstacle Pseudovorticity Length-scale Universality Streaming Quartz tuning fork Cavitation Oscillation wake

Acknowledgments

The author thanks to prof. Ladislav Skrbek, DrSc. whose wisdom attracted the author to quantum turbulence, and to his consultant Dr. Marco La Mantia for his patience with the author's stubbornness. Then the author thanks to all his colleagues in the laboratory, namely to doc. RNDr. Miloš Rotter, CSc., Mgr. Patrik Švančara and Petra Hrubcová for a nice collaboration. From „the second laboratory“ the author thanks to RNDr. David Schmoranzner, PhD., Mgr. Emil Varga, Dr. Martin James Jackson, MPhys. PhD. AMInstP., Bc. Tamara Skokánková and RNDr. Hana Divišová for fruitful discussions. He also thanks to willing Ing. Bohumil Vějr and to all crew of the liquifier, because all cryoliquids are always ready, when we need them.

We acknowledge the support of Charles University under grant GAUK 1968214.

Special great thanks belongs to Eva Dudová for motivating the author and for her patience with the author's long study. At the same time, the author apologizes to Adela and Václav for spending their early childhood in small flat in overgrown city of Prague far from all grandparents and other relatives and without any significant space for play.

Contents

1	Introduction	3
1.1	Helium	3
1.2	Length-scale depending description	4
1.2.1	From particles to waves	4
1.2.2	Quantized vortices and vortex tangle	5
1.2.3	Two-fluid model	7
1.3	Particles in fluid	9
2	Experimental setup	13
2.1	Cryostat with optical access	13
2.2	Accessing and measuring low temperatures	13
2.2.1	Pumps	14
2.2.2	Temperature measurement	14
2.2.3	Pressure measurement	15
2.3	Seeding system	17
2.4	Moving obstacle	19
2.5	Quartz tuning fork	21
2.6	Laser and camera	24
2.7	Data acquisition procedure	25
2.8	Image processing	25
2.9	Data processing	26
2.9.1	Custom-made particle tracking algorithm	26
2.9.2	Evaluation of our tracking algorithm	27
2.9.3	Statistics over trajectories	28
2.10	PTV-based pseudovorticity	29
2.10.1	Regular vorticity	29
2.10.2	Definition of pseudovorticity	30
2.10.3	Convergence	31
2.10.4	Discussion of conditions	32
3	Table of parameters	35
4	Oscillating obstacle	39
4.1	Introduction	39
4.1.1	Brief setup description	40
4.2	Observations	41
4.2.1	Phase averaging	41
4.3	Macroscopic vortices	45
4.3.1	Vortex model	45

4.3.2	Vortex circulation profiles	48
4.4	Behavior of $\langle v^2 \rangle$	51
4.4.1	Dependence on Reynolds number	52
4.4.2	Length scales	54
4.4.3	The quantum signature	55
4.5	Discussion	56
4.5.1	Choice of integration area radius	58
4.6	Conclusion of the chapter	59
5	Streaming flow	61
5.1	Introduction	61
5.2	Results	63
5.2.1	Data sets	63
5.2.2	Observations	64
5.2.3	Summary of observations	71
5.3	Discussion	71
5.3.1	Number of streaming cells	71
5.3.2	Quantum length scale	73
5.3.3	Choice of R_m	73
5.3.4	Resonance stability	74
5.3.5	Thermal counterflow	75
5.3.6	Bubble in He I	76
5.4	Conclusion of the chapter	76
6	Cavitation	79
6.1	Introduction	79
6.2	Experimental setup	80
6.3	Observations	81
6.4	Conclusion	83
7	Small-scale similarity in quantum turbulence	85
7.1	Introduction	85
7.2	Experimental setup	86
7.3	Length-scales	86
7.3.1	Probed length-scale	86
7.3.2	Flow length-scale	87
7.4	Results	88
7.5	Conclusions of the chapter	91
8	Conclusion	93
8.1	List of publications	94
8.2	List of conference presentations	96

Preface

This Thesis mainly follows the author's work on the 3-years project of GAUK (Grantová Agentura Univerzity Karlovy) number 1968214: *Studium oscilačních proudění a kavitace v kapalném heliu vizualizačními metodami* solved during his 4-year doctoral study at the Faculty of Mathematics and Physics of the Charles University. The Thesis does not track the entire work performed by the author - it rather attempts to provide a comprehensive report on experimental studies of mechanically driven oscillatory flows in both normal viscous liquid ^4He and in superfluid ^4He , focusing on the similarities and differences between the classical and quantum flows. It is motivated, among others, by questions if macroscopic vortices can exist in the wake (we found that *yes*), if the mechanically driven coflow of both components mimics the classical turbulence up to such a level that they are indistinguishable (we found that *no*) and additionally, if higher order effects such as *viscous streaming* can take place in superflows (we found that *yes*).

The structure of the Thesis is as follows: in the Introduction the reader finds a short story about the helium itself, then three widely used descriptions of superfluid hydrodynamics are introduced, and, finally, a short discussion of the particle-based visualization methods follows. As a short introduction in the corresponding classical hydrodynamics is a part of each of following experimental chapters, we skip this in the Introduction. The second chapter describes the used apparatus and methods: a large space is devoted to those parts of the apparatus that were built by the author personally (namely the driving mechanism of the obstacle) and to the data analysis, which has been developed mainly by the author, especially to the idea of the PTV-based pseudovorticity. It is followed by a short chapter summarizing and comparing the experimental conditions of presented experiments including the dimensionless numbers used in this thesis and their definitions. Next three chapters describe the experiments: the wake flow past an oscillating obstacle of a shape of a prism, the viscous streaming due to the oscillating quartz tuning fork and the cavitation due to the fast oscillating fork. The last chapter presents one of the most interesting results achieved jointly by the entire research group of the visualization Laboratory – the universality of quantum flows observed at small length-scales.

Author's contribution

The author began working in the Prague Flow Visualization Laboratory under the guidance of prof. Ladislav Skrbek at the end of 2010. The early measurements have been used as a part of his Diploma thesis and are therefore not discussed here. The presented work is a result of the joint effort of the entire research group working on visualization of various types of flows of all forms of cryogenic helium.

The author was involved mostly in the technical aspects of the experiments: preparation of the electrical circuits measuring the supporting quantities, programming the data acquisition and experiment control in the LabView programming interface. The actual measurements were performed by all members of the research group in the laboratory under leadership of Marco La Mantia. The following image data processing were performed by various people including the author. The author developed a program used for statistical data analysis, advanced filtering, smoothing and trajectory repairing (also described here) and performed the analysis of the presented experiments. Several methods have been suggested and introduced by the author (phase averaging, vortex profiles, PTV-based pseudovorticity and effective bubble radii). The published articles, although on several of them the author of this thesis is written as the first author, were mainly written by Marco La Mantia and Ladislav Skrbek, the author usually initiated them, took part in designing and preparation of the experiment, data acquisition, subsequent analyzes and discussions and supplied the figures.

Chapter 1

Introduction

1.1 Helium

Helium is the second most abundant element in the Universe, most of it born together with the entire Universe in the *recombination age* short after the Big Bang, the rest was produced inside cores of massive short living stars, which already finished their lives before the Solar System was formed. According to the spectroscopic observations of both, the solar photosphere¹ and the CI-type carbonaceous meteorites², it is though that the helium abundance in the nebula, Solar System was build of, i. e. a protosolar abundance, was 0.27 [1].

The estimation of the primordial helium abundance is much more complicated. According to spectroscopic observations of very distant low-metallicity galaxies close to the *surface of last scattering*, its primordial abundance has been estimated to be about 0.24, see, among others, Izotov et al. [2].

Helium exists in the form of 2 stable isotopes, ³He and ⁴He, containing in the core 2 protons and 1 neutron, ³He, and 2 neutrons, ⁴He, respectively. In the shell it has 2 electrons filling the orbital 1s, thus in this system there are 5, ³He, or 6 particles, ⁴He, with spin. The total absolute value of spin is then 1/2, ³He, or 0, ⁴He, (considering no excitations) and the system of helium atoms is consequently governed by the *Fermi-Dirac statistic*, ³He, or by the *Bose-Einstein statistic*, ⁴He respectively. These different statistical distributions are responsible for the fact that ³He and ⁴He have different properties at low temperatures, although at high temperatures they are very similar, because the high temperature limit of both statistics is the *Boltzmann statistics*.

The protosolar ratio of two main helium isotopes ³He and ⁴He is determined from the Jupiter's atmosphere to be $n_3/n_4 = (1.66 \pm 0.05) \cdot 10^{-4}$ [3].

Although helium is generally not rare, on Earth it is. In addition, all helium, which is available now, is a product of α -decay or it came with impacting meteorites, where it had been implanted into the surface materials by solar wind. As helium is a *noble gas*, it does not create compounds and, as it is lighter than all other gases in Earth's atmosphere, free helium goes up, until it leaves Earth

¹Contemporary photosphere is depleted due to the sedimentation of heavier elements, on the other hand, helium amount increases with time due to thermonuclear reactions, therefore a solar model has to be used to properly correct this effects.

²These meteorites contain only little amount of helium, but the ratios of other elements is believed to be the protosolar one.

being blown away by the solar wind [4].

${}^3\text{He}$ is instead the product of the decay of tritium with the decay half-time of 12 years, which is mostly an artificial product used for the thermonuclear weapons,



and, as ${}^3\text{He}$ has a large cross section for trapping neutrons, it brakes the chain reaction, therefore its attendance is unwanted and has to be periodically removed³. For the same reason, ${}^3\text{He}$ is industrially used for neutron detectors⁴.

Helium was discovered in 1868 in the spectral decomposition of the sunlight as an element not previously known. It was called *hélium* from the word $\acute{o}^c\eta\lambda\iota\omicron\varsigma$, which means *the sun* in Greek.

Both isotopes *do not* form the solid state, at atmospheric pressure, until the temperature reaches the absolute zero; both become liquid at few Kelvin, 4.215 K for ${}^4\text{He}$ and 3.19 K for ${}^3\text{He}$, [5], and both have the *superfluid phase*, which is however generated by different mechanisms. The isotope ${}^4\text{He}$ has the transition to the superfluid phase, called λ -transition, at the temperature $T_\lambda = 2.1768\text{ K}$, at the saturated vapor pressure [6], while ${}^3\text{He}$, being a *fermion*, has to form *Cooper pairs*, which have an integer absolute value of spin (equal to one). Its superfluid transition temperature is 1000 times lower, 0.93 mK, at the saturated vapor pressure [7].

1.2 Length-scale depending description

Depending on the length-scale, matter can be described by various ways, highlighting the lack of detailed understanding of this very important part of Nature and hence the need of further research looking not only for the answers, but also for a new exciting questions. This section freely follows the excellent article of Barenghi, L'vov and Roche [8].

1.2.1 From particles to waves

A classical description of a gas is a model of *billiard balls* displaying molecules as a solid balls (or of other shape), which collide one with each other and between the collisions move ballistically, being influenced by a longer-distance potential of other molecules. According to the quantum-mechanical approach, each object can be seen at the same time as a *particle* and as a *wave*. The corresponding wavelength λ of such a wave is

$$\lambda = \frac{h}{p} \approx \frac{h}{\sqrt{mk_B T}} \sim T^{-\frac{1}{2}}, \quad (1.2)$$

where $h = 6.6 \cdot 10^{-34}\text{ Js}$ is the Planck's constant [9], p is the momentum, which, in thermal equilibrium, corresponds to $\sqrt{mk_B T}$, m denotes the particles mass, T is

³It is not the aim of this Thesis to discuss politics, but the pleasing politics of disarm has also another side: the lack of ${}^3\text{He}$ leading to incredibly huge price and, naturally, to limiting the research of this fascinating material.

⁴A large demand of this devices also increases the price of ${}^3\text{He}$.

the temperature and $k_B = 1.4 \cdot 10^{-23}$ J/K is the Boltzmann's constant [9]. Equation 1.2 is, roughly speaking, the reason why low temperatures are so interesting: with decreasing temperature, the wavelength of particles in a thermodynamic system increases until the waves overlap and start to interfere creating a single macroscopic wave of matter displaying macroscopic quantum effects. It happens when the wavelength 1.2 is larger than the mean interparticle distance d , which can be estimated simply as $d \sim n^{-1/3}$, where $n = \rho/m$ is the numerical density of the system of density ρ consisting of particles of mass m (of course, if the particles are identical). Then, by setting

$$d \approx \lambda \Rightarrow T_q \sim \frac{\hbar^2 \rho^{2/3}}{k_B m^{5/3}}, \quad (1.3)$$

which, explicitly, for liquid helium gives $T_q \sim 10^1$ K, while for electrons in metal it suggests $T_q \sim 10^6$ K and for matter of a *neutron star* $T_q \sim 10^{11}$ K [10].

The equation 1.3 is not able to determine the exact temperature of transition into quantum regime, but the correct order of magnitude suggests that the above described explanation is not entirely wrong.

The macroscopic wave of weakly interacting bosonic gas is usually described via the so called *Gross-Pitaevskii* equation [11] for the *macroscopic order parameter* $\Psi(\vec{x}, t)$:

$$-i\hbar \frac{\partial \Psi}{\partial t} = \frac{\hbar^2}{2m} \nabla^2 \Psi - V_0 |\Psi|^2 \Psi + \mu \Psi, \quad (1.4)$$

where V_0 is the strength of interbosonic interaction and μ is the chemical potential. Other symbols have standard meaning [11]. Of course, this is an approximation of 1st order of the so called *generalized non-linear Schrödinger equation* [12], which represents the nonlocal two-body interaction potential as a function $V(|\vec{r}_1 - \vec{r}_2|)$ of the distance of two points \vec{r}_1 and \vec{r}_2 , for which it can be installed, e. g., the Lenard-Jones potential⁵ [13]. The 3rd order polynomial expansion of the *equation of state* installed into 1.4 (i. e. with terms up to $|\Psi|^6$) has been used in mathematical studies of instability of vortices and of *cavitation* at negative pressures [14], showing qualitative agreement with experiment [15].

Equation 1.4 at non-zero temperatures can be qualitatively enhanced to a *dissipative Gross-Pitaevskii equation* [16]:

$$i\hbar \frac{\partial \Psi}{\partial t} = (1 - i\gamma) \left(-\frac{\hbar^2 \nabla^2}{2m} + V_0 |\Psi|^2 + \mu \right) \Psi. \quad (1.5)$$

This equation was originally suggested phenomenologically by Pitaevskii [11], although it is oversimplified, Proukakis [16] used this phenomenological model to study the Kolmogorov spectrum [17, 18] showing that 1.5 can capture key features relevant to the turbulence [19].

1.2.2 Quantized vortices and vortex tangle

The Gross-Pitaevskii equation 1.4 can be solved numerically in two or three dimensions [12], but, due to the non-linearity of the interaction term, it is not soluble analytically (not talking about the enhanced versions just mentioned). Moreover, the experimental access to these length-scales is limited only for trapped

⁵ $V(r) = (b_1 + b_2 r^2 + b_3 r^4) e^{-B^2 r^2}$, $r = |\vec{r}_1 - \vec{r}_2|$ for the values of phenomenological parameters $b_{1,2,3}$ and B see [13].

atomic condensates [20], whose *healing length*, $\xi = \hbar/\sqrt{2m\mu}$, where μ is the chemical potential [10], is naturally larger than that of helium. Exact solution of the Gross-Pitaevskii equation 1.4 can explain the existence of *quantized vortices* [21] including their internal structure on a length-scale of the healing length ξ , but the basic idea of quantization of vorticity can be judged from the basic fact, that the order parameter Ψ has to be *continuous* and *unequivocal*, and from the *Madelung transformation* relating $\Psi = |\Psi| e^{i\phi}$ with local condensate density ρ_s and velocity v_s ,

$$\begin{aligned}\rho_s &= m |\Psi|^2, \\ v_s &= \frac{\hbar}{m} \nabla \phi.\end{aligned}\tag{1.6}$$

Therefore from the identity $\nabla \times \nabla \phi \equiv 0$ we get that the *vorticity*

$$\nabla \times v_s = 0\tag{1.7}$$

everywhere in the bulk, except for the *topological singularities* called *quantized vortices*, whose circulation Γ is quantized

$$\Gamma = n \frac{\hbar}{m} = n \kappa \cong n 9.98 \cdot 10^{-8} \text{ m}^2/\text{s},\tag{1.8}$$

where κ is the *quantum of circulation* and $n \in \mathbb{N}$. From energetic considerations⁶ it can be derived that in ⁴He the system prefers containing more vortices of $n = 1$ instead of single multiply quantized one. The size of quantized vortex core can be estimated to be of order of the *healing length* ξ .

At scales much larger than the healing length, but still microscopic compared with scales experimentally accessible in liquid ⁴He, the quantum turbulence is usually described via so called *vortex filament model* [23].

The equation 1.6 for velocity \vec{v}_s leads to $v_s(r) = \kappa/2\pi r$ at the distance r from the vortex in the plane perpendicular to it. More generally, the *Biot-Savart law* [24] around the quantized vortex represented as a infinitesimally thin line reads:

$$\vec{v}_s(\vec{r}, t) = \frac{\kappa}{4\pi} \int \vec{s}' \times \frac{\vec{s} - \vec{r}}{|\vec{s} - \vec{r}|^3} d\zeta,\tag{1.9}$$

where $\vec{s}(\zeta)$ is the vortex filament parametrized by arc length ζ , $\vec{s}'(\zeta) = d\vec{s}/d\zeta$ is the unit tangent vector and the line integration is along all the vortices. The Biot-Savart law expresses the Euler dynamics in integral form by assuming a fluid of constant density [25].

In numerical modeling, the vortices are usually considered to be thin and the mass of the vortex core of diameter of the order of the healing length is neglected [23]. Therefore, at zero temperature, vortices move according to the local superfluid velocity \vec{v}_s , but at non-zero temperature, the effect of the normal fluid is included phenomenologically by adding mutual friction coefficients α and α' to the equation of filament motion [23]:

$$\vec{v}_L = \frac{d\vec{s}}{dt} = \vec{v}_s + \alpha \vec{s}' \times (\vec{v}_n - \vec{v}_s) - \alpha' \vec{s}' \times [\vec{s}' \times (\vec{v}_s - \vec{v}_n)],\tag{1.10}$$

⁶Lets look into the author's diploma thesis [22] or into [10].

where v_n is the normal component velocity, which is, usually in the numerical studies prescribed artificially [26] in such a way that it obeys the classical Kolmogorov $k^{-5/3}$ scaling [27].

When two vortices approach, they can *reconnect*, changing the overall topology of the vortex tangle. The detailed mechanism of reconnection is a subject of, mostly numerical, studies on the level of order parameter dynamics [12] and, in the studies of the vortex tangle, they have to be prescribed artificially [23].

The statistical numerical studies of vortex tangle [27] show that the superfluid energy spectrum is consistent with Kolmogorov [17] scaling between the quantum length scale ℓ and the large length scale [28]. This result holds down to zero temperature in agreement with the numerical studies of the Gross-Pitaevskii equation [23].

It is found that the vortices are often not randomly distributed, but they form local bundles of corotating vortices [29], which are associated with the Kolmogorov spectrum. It is possible to decompose the vortex tangle into the *polarized* part of *vortex line density* L_{\parallel} and the *random* part L_{\times} [30], where just the L_{\parallel} seems to be responsible for the $k^{-5/3}$ scaling [8], while L_{\times} exhibits a different k^{-1} scaling [31].

1.2.3 Two-fluid model

It has been already mentioned above without any comprehensive statement that, at non-zero temperatures, there exists a *dissipative part* of the superfluid helium, which affects the behavior of He II significantly. It is formed of thermal excitations – phonons, whose energy $E \sim k$ at small k . An *icon* of the *ballistic regime* at very low temperatures is the *Andreev scattering* [32] of excitations (quasiparticles and quasiholes) on quantized vortices, which is a useful tool for studies of superfluid ^3He [33].

At larger temperatures and/or length-scales, the coarse-grained look on phonons is smoothed creating the so called *normal component* of He II described as a continuous fluid with non-zero viscosity coexisting with the *superfluid component*. The existence of two more-or-less independent components of He II is responsible for the wide range of strange experimental observations (such as flow through very small holes – superleaks, the existence of superfluid film, the mechanocaloric effect, fountain effect, different viscosity if measured in bulk or in a capillary, reduction of momentum of inertia, enormous heat conductivity), which played significant role in the history of superfluidity.

Similarly, at larger length-scales the individual vortex lines are no more distinguished, rather they are considered as a continuum of vortices, so it is possible to define a macroscopic vorticity field $\vec{\omega}_s$ by taking a small volume larger than the mean intervortex distance ℓ . This approach leads to the so called *Hall-Vinen-Bekarevich-Khalatnikov coarse-grained* equations for two considered velocity fields \vec{v}_s and \vec{v}_n of He II [10]:

$$\begin{aligned} \rho_s \left[\frac{\partial \vec{v}_s}{\partial t} + (\vec{v}_s \cdot \nabla) \vec{v}_s \right] &= -\frac{\rho_s}{\rho} \nabla p + \rho_s S \nabla T - \rho_s \vec{f}_{ns} \\ \rho_n \left[\frac{\partial \vec{v}_n}{\partial t} + (\vec{v}_n \cdot \nabla) \vec{v}_n \right] &= -\frac{\rho_n}{\rho} \nabla p - \rho_n S \nabla T + \rho_s \vec{f}_{ns} + \rho \nu \nabla^2 \vec{v}_n, \end{aligned} \tag{1.11}$$

where $\rho_{n,s}$ are the densities of normal and superfluid component, S is the entropy per unit volume, T is temperature and \vec{f}_{ns} is the *mutual friction force* usually defined as

$$\vec{f}_{ns} = \alpha \vec{\omega}_s^0 \times (\vec{\omega}_s \times \vec{v}_{ns}) + \alpha' \vec{\omega}_s^0 \times \vec{v}_{ns} - \frac{\rho_n}{2\rho} \nabla v_{ns}^2, \quad (1.12)$$

where $\vec{v}_{ns} = \vec{v}_n - \vec{v}_s$ is the counterflow velocity, $\vec{\omega}_s = \nabla \times \vec{v}_s$, $\vec{\omega}_s^0 = \vec{\omega}_s / |\vec{\omega}_s|$, the coefficients α and α' are the same as in equation 1.10 and their temperature dependent values together with the whole form of equation 1.12 is adapted for the experiments in rotating cryostat [21]. The last term in equation 1.12 is usually neglected, a stronger simplification of 1.12 is just $\vec{f}_{ns} = -\alpha \kappa \vec{v}_{ns} / \ell^2$ [8].

The second term on the right hand side of equation 1.11 corresponds to a very interesting type of thermal convection with no classical counterpart – the *thermal counterflow* of the normal and the superfluid component of He II. Only the normal component carries the entire entropy of the fluid, hence the heat transfer q is

$$\vec{q} = \rho S T \vec{v}_n \quad (1.13)$$

and, from the continuity equation, it is possible to determine the corresponding velocity of the superfluid component (omitting vectors, in a narrow channel)

$$v_s = -\frac{\rho_s}{\rho_n} v_n. \quad (1.14)$$

Thermal counterflow is not a subject of this Thesis, for more details we direct the reader to [34].

Still, we mention here another interesting phenomenon connected with the two-fluid nature and with the opposite reaction on thermal gradient – the *second sound*. Second sound is a wave of temperature, or, in other words, of relative normal fluid density, which can be excited by a heater or by a moving membrane with superleak⁷, which is found to be a very useful tool for direct measurement of the vortex line density L thanks to the attenuation by a tangle of quantized vortices, as can be judged from equation 1.10 or from the literature [35].

It is important to bear in mind that the equation 1.11 has physical meaning only at length-scales significantly larger than the quantum length-scale represented by the intervortex distance ℓ .

Direct numerical simulations of equation 1.11 show evidence of strong locking of the superfluid and normal fluid ($\vec{v}_s \approx \vec{v}_n$) at large scales [36]. It was found that even if one single fluid is forced at large scales, the locking is still very efficient. Indeed, a clear $k^{-5/3}$ spectrum for both fluid components at large scales is found at all temperatures [8].

Here we point out that the famous Kolmogorov scaling [18] is valid only for a homogenous isotropic three-dimensional turbulence, therefore another cascades [37] exist even in the classical turbulence, e. g., in a two-dimensional system the so-called *inverse cascade* [38] is observed, which can, among others, explain the existence of large-scale zonal flows observed on gaseous planets [39] (if they are shallow, which is not known yet [40]).

To summarize, turbulence in He II can be easier to understand, in such a way that the quantized vortices, which the turbulence is built of, are clearly defined

⁷It means a porous membrane, through which only the superfluid component can pass.

objects with constant circulation and quite „simple“ rules of behavior (equations 1.9 and 1.10). On the other hand, at stronger forcing, both components become turbulent influencing each other via the still mysterious mutual friction force resulting into one of the most challenging objects of study ever.

1.3 Particles in fluid

Particle Image Velocimetry (PIV) and *Particle Tracking Velocimetry* (PTV) are standard methods in classical hydrodynamic research based on suspending *small* particles into the fluid and believing that these particles follow the motion of the fluid. PIV can estimate the fluid velocity in a section of the flow field, by assuming a single, smoothly varying velocity field, i. e. the *Eulerian* point of view is native for this technique. PTV allows the measurement of *Lagrangian* quantities [41], i. e., the velocity and its derivatives [42], along the individual trajectories of the tracked particles.

In both techniques, small particles are suspended in the fluid. They reflect the light of an appropriate source, e. g., a laser beam, and their time-dependent positions are captured by suitable sensors, e. g., a digital camera, and processed by purpose made software. PTV allows determining the Lagrangian trajectories of the visualized particles, while PIV, which requires a larger number of particles, does not allow the direct calculation of the velocity of each visualized particle but provides a statistical estimate of the *Eulerian* velocity field in chosen locations, called interrogation areas, with a small number (~ 10) of particles.

Considering a small spherical particle in a classical liquid, the two main contributions are the inertial forces depending on mass, i. e. $\sim r^3$, and the viscous forces depending on the surface, i. e. $\sim r^2$, therefore the smaller particle is better follower of the flow. The *shear* of the flow also affects a smaller particle less than a bigger one and it vanishes at the Kolmogorov length-scale.

The movement of small spherical particle in the flow-field can be numerically modeled [43] via so-called Maxey-Riley equation [44], which, among others, contains the added mass effect [45], the history of vortex separation, the Saffman lift force and Faxén corrections⁸. The inverse solution of such a complicated equation is nearly impossible, hence the interpretation of experimentally obtained particle movement data considers the dominance of the viscous term, i. e. that the particle follows the flow, although some higher order effects are well known (e. g. the settling or the *preferential concentration* effect).

On the other hand, for practical purposes the particle should be observable by the used camera. The experience suggests that it ought to cover few pixels of the acquired image [46], which, for example, is not fulfilled in majority of the standard PIV measurements in air, where so small particles (droplets of oil or glycerin) have to be used, that they are unobservable – only the inhomogeneous density patterns are correlated [46].

In the case of He II, which is a superfluid quantum liquid containing quantized vortices and described by the two-fluid model, the situation is more complicated [47]. In the first order approach, the particle moves with the viscous *normal*

⁸We apologize for not reproducing here the entire equation, an interested reader can find in the original form in [44] or in an improved form in [43].

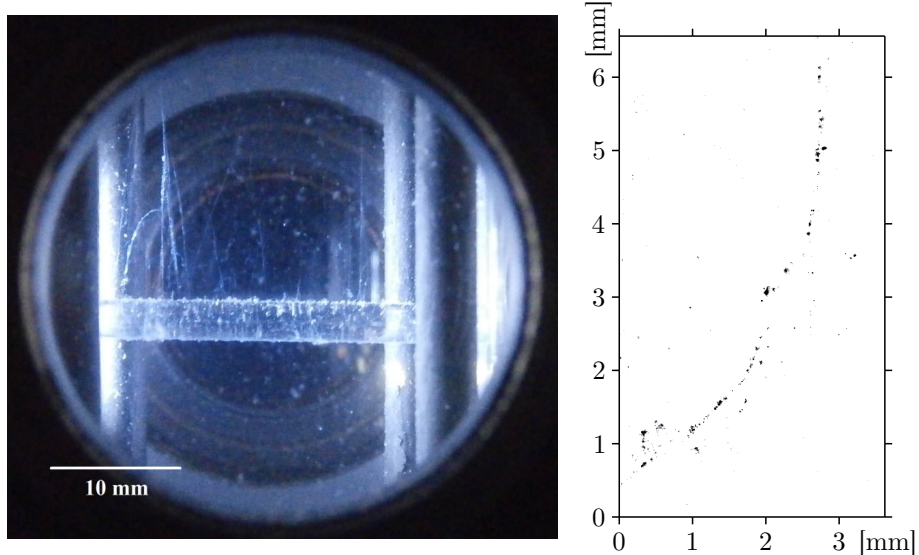


Figure 1.1: **Left:** the photograph of the transparent cylinder used in the experiment [50] taken by a digital camera, the length scale is approximately valid in the focused plane, temperature 2.16 K, H₂ particles, note the filaments. **Right:** negative of image of a filament structure, which might be a quantized vortex, temperature 2.15 K, H₂ particles.

component, while the *superfluid component* affects the particle motion only via its shear due to the *D'Alembert paradox*. Additionally, the particle can be *trapped* onto a quantized vortex [48], which allows direct vortex visualization [49], see figure 1.1.

The energy of quantized vortex line can be expressed as the kinetic energy of superfluid component of He II orbiting the quantized vortex core,

$$\begin{aligned}
 E &= \int \frac{1}{2} \rho_s v_s^2 d^3x = 2\pi \frac{1}{2} \rho_s \int v_s^2 r dr d\zeta = \pi \rho_s Z \int_{\xi}^R \frac{\kappa^2}{r} dr = \\
 &= \pi \kappa^2 \rho_s Z \ln \frac{R}{\xi},
 \end{aligned} \tag{1.15}$$

where ζ is the length element of the vortex, Z is the considered length saved by passing through the particle (i. e. $Z \approx 2R$), R is the radius of the particle and ξ is the *coherence length* considered to be the vortex core radius. The passing of the vortex core through the particle is energetically favorable and the particle can be trapped on the vortex core. The latter depends on the previous velocity of particle and on the drag force due to the normal component of He II acting on the particle. The dissipative mechanisms, reducing the kinetic energy of particle moving relatively to the vortex core and thus enabling the trapping, are not entirely understood [51]. It is not known, for example, why the particles trapped onto vortices are positioned equidistantly. In the experiment, it is not possible to determine, if any particular particle is trapped or not. Note that the particle is huge compared to the quantized vortex core ($\xi \sim 10^{-10}$ m, $R \sim 10^{-5}$ m, see section 2.3), but it can be larger *or* smaller than the intervortex distance ℓ in dependence on the flow conditions.

In the article [50], we have shown that the use of PIV technique in He II [52] can give not fully trustworthy results, especially in thermal counterflow, where both components move in opposite directions. We have imposed the thermal counterflow by a heater placed at the bottom of optical cryostat (see following chapter for more technical details about the apparatus) and we placed a cylinder of diameter 3mm into the channel far from the walls and the heater. Both techniques were applied on the same data giving very different results – the PIV results obtained by the *Dantec Dynamic Studio* displays a smooth velocity field with few macroscopic vortical structures, while, in the trajectory image, those are not distinguishable, see figure 1.2.

Explanation of this discrepancy is that only one peak in the image correlation space calculated during the PIV processing is used to calculate the resulting velocity vector, others are classified as noise. If it corresponds to the particles carried by the normal component, or to those trapped on quantized vortices, is random, which can easily lead to spurious sheer or vortical patterns. On the other hand, the backward recirculation of normal component is suggested also by numerical simulations [53], suggesting that the results of [52] are correct, due to the dominance of viscous drag due to the normal component on the bigger particles⁹.

To conclude, the use of particle-based visualization is very useful tool [47], it especially shows the similarities and differences between classical and quantum flows, but enormous care has to be taken when interpreting the results, namely when we try to obtain spatially smooth quantities. It depends on the imposed flow type – the mechanically driven flow, which is main topic of this Thesis, exhibits *coflow* of the normal and the superfluid component, therefore the use of PIV technique might work properly in two distant limits: intervortex distance comparable to the probed volume, when the particle is carried by the normal component only (this is a hypothetical case, as just the planetary rotation produces decent number of vortices [19]), or very small intervortex distance, when the vortex tangle behaves as a continuum, which, due to the mutual friction force, locks the two components more rigidly. In between, even in the case of coflow, the particle generally moving with the normal component is affected by the quantized vortices and their reconnections. Hence, anomalous particle behavior might not be observed on the trajectory shape, but velocity statistics can clearly display the quantum nature of the flow [54].

⁹Viscous drag depends on particle surface, while the trapping potential on the diameter, equation 1.15, therefore smaller particles better maps the quantized vortices, while bigger ones do the normal component.

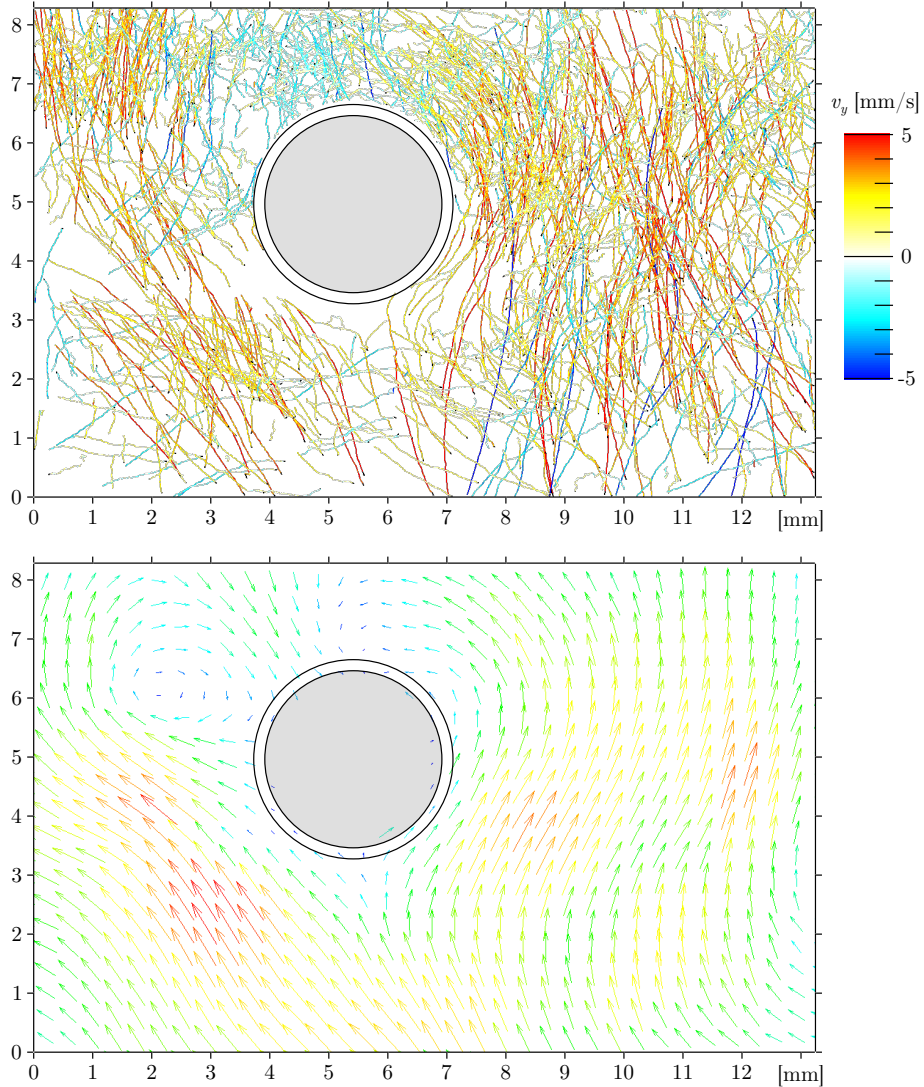


Figure 1.2: Top: Hydrogen particle tracks obtained at temperature $T = 2.02$ K and heat flux $q = 477$ W/m² (transparent cylinder, heater on bottom, switched on). Only trajectories longer than 50 points are displayed. Note minority of particles going in opposite direction than the majority, which is a typical effect observed in thermal counterflow. 2000 images taken at camera frequency 100 Hz; field of view 13.2×8.2 mm. **Bottom:** PIV results of the same data set. The square interrogation areas have 75% overlap. The vector sizes and colors are proportional to the velocity magnitude, whose maximum, shown is red, corresponds to about 4 mm/s. Note the *clear vortex* at coordinates $\sim [2; 6]$.

Chapter 2

Experimental setup

2.1 Cryostat with optical access

In order to keep helium in the liquid phase a *cryostat*, i. e., a suitable thermal insulating vessel, is needed. In our laboratory we use a cryostat with 5 optical ports: it was designed at MFF UK and assembled by Precision Cryogenic Systems. This device is well described in the previous work of my colleagues [55].

The cryostat can store more than 50 dm^3 of liquid helium, which is enough for a typical experimental run. It is usually not refilled during the experiment as this would most likely decrease the quality of images, due to increasing number of spurious particles made of frozen air or water. Care is taken to ensure that helium is as clean as possible, by flushing the cryostat with purified helium gas, before each experiment.

The inner volume of the cryostat is thermally shielded by a cylindrical volume of liquid nitrogen N_2 , as this reduces the radiant component of heat flow according to the *Stefan-Boltzmann law* $P \sim \Delta T^4$. There is an additional evacuated volume, which reduces thermal conduction. This volume is regularly pumped by a turbomolecular pump before each experiment, keeping the pressure in it typically between $5 \cdot 10^{-6}$ and $1 \cdot 10^{-5}$ Torr¹.

There are 3 windows for each of the 5 optical ports; the innermost windows are made of sapphire, while the others are made of quartz. The cross-section of the optical tail is square with side of 50 mm, while the largest part of the cryostat has a cylindrical shape with inner diameter equal to 200 mm. The windows have circular cross-section with diameter equal to 25 mm, see the draft of the bottom part of the cryostat in figure 2.1.

2.2 Accessing and measuring low temperatures

After liquid helium is transferred into the cryostat the helium bath has a temperature of 4.2 K, which is the boiling temperature of helium at atmospheric pressure. To decrease the temperature we decrease the bath pressure along the *saturated vapor pressure curve* (see figure 2.2). The pressure is monitored and

¹ Torr is not a SI unit, $1\text{ Torr} = 133.322387415\text{ Pa}$, 1 Torr is the hydrostatic pressure of a column of height 1 mm of pure Hg in a *standard* gravity field of Earth $g = 9.80655\text{ m/s}^2$ (exactly) [56].

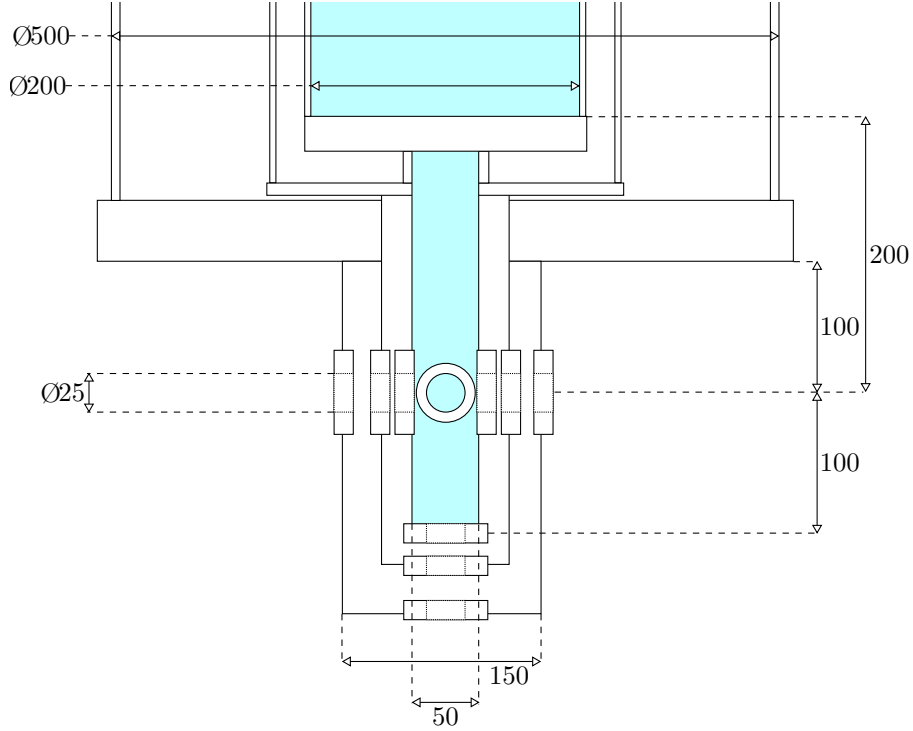


Figure 2.1: Draft of the bottom part of the cryostat used in the visualization laboratory at MFF UK and assembled by Precision Cryogenic Systems. The volume filled with helium is highlighted by the *blue* color. Units are in mm. The vessel for liquid nitrogen, thermally connected to the middle layer in order to shield parasitic thermal radiation, is positioned higher up and not visible in the displayed part of the cryostat.

used to determine the bath temperature, see below.

2.2.1 Pumps

In order to pump the helium bath, we use two pumps connected in series: the first one is a Roots pump, with maximum pumping rate of $324 \text{ m}^3/\text{h}$, the other is a mechanical rotary pump, with a maximum pumping rate of $36 \text{ m}^3/\text{h}$. At higher pressures, the automatic electronic control unit switches on the rotary pump only, while at lower pressures it adds the Roots pump. The pumps are connected to the cryostat via a bellows tube of 50 mm in diameter, via a computer-controlled „butterfly valve“ with a manually controlled bypass. The vibrations produced by the pumps are reduced by a purpose-made bellows T-piece. To avoid spurious electrical currents, the bellows tube is electrically insulated from the cryostat by a plastic o-ring. The output of the pumps either enters the *helium return line* or is open to the air, depending on the situation (cooling down the helium bath, the former case, evacuating the cryostat, the latter case).

2.2.2 Temperature measurement

Temperature is an *intense* quantity, which makes sense only for a thermodynamic system of large number of atoms or molecules. Mathematically, temperature is a parameter of the energy distribution in the system, which is represented

at higher temperatures by the *Planck's radiation law* for the *absolutely black body*, which at the same time serves as the definition of temperature:

$$dI(\omega; T) = \frac{\hbar}{\pi^2 c^2} \frac{\omega^3}{e^{\frac{\hbar\omega}{k_B T}} - 1} d\omega. \quad (2.1)$$

Here $dI(\omega; T)$ is the radiation intensity element as the function of angular frequency $\omega = 2\pi f$ of the radiated light and at certain temperature T of the black body. \hbar , c and k_B are all constants with recommended values according to [9]: Planck's constant $\hbar = 1.055 \cdot 10^{-34}$ Js, the speed of light in vacuum $c = 299792458$ m/s and Boltzmann constant $k_B = 1.381 \cdot 10^{-23}$ J/K. The radiation intensity is important only for higher temperatures. At temperature 2 K the total intensity is

$$I_{\text{tot}}(T) = \int \frac{dI}{d\omega} d\omega = \frac{\pi^2 k_B^4}{60 \hbar^3 c^2} T^4 = \sigma T^4 = 0.9 \mu\text{W}/\text{m}^2. \quad (2.2)$$

For comparison, the radiation intensity at room temperature 300 K is 460 W/m² and at the melting point of gold 1337 K it reaches 180 kW/m². The definition 2.1 is useful and practical at higher temperatures, while at low temperatures it is nearly impossible to use.

Therefore the *Bureau International des Poids et Mesures*² published the *international temperature scale ITS-90* [6], where the *saturated vapor pressure* of ⁴He vapor over the liquid bath is recommended as the primary thermometer for the temperature range from 1.25 up to 5.0 K. The relation between the saturated vapor pressure and the absolute temperature is unequivocal, but there is no simple theoretical relation between them, hence the definition 2.3 in ITS-90 is rather complicated.

The conversion between the temperature T and the saturated vapor pressure P according to [6] is

$$T = A_0 + \sum_{k=1}^8 A_k \left(\frac{\ln P - B}{C} \right)^k, \quad (2.3)$$

where the coefficients A_0 to A_8 , B and C are tabulated 2.1 (copied from *tabelau III* in [6]). The total dependence is shown in figure 2.2.

2.2.3 Pressure measurement

The pressure is measured by the Barotron MKS 690A sensor connected to the cryostat by a capillary of 8 mm inner diameter. According to the manufacturer, the used sensor measures the pressure absolutely. It is connected to the signal conditioner MKS 670, which communicates with the computer via a GPIB bus.

It is assumed that the measured pressure is not affected by the state of helium gas in the tube. The difference in height between the sensor and level of liquid helium in the cryostat is around 0.8 m. The level of liquid helium is, however, changing during the experiment, as the temperature is lowered by pumping the vapor, thus reducing the amount of liquid helium inside the cryostat. The difference

²Abbreviation BIPM.

Table 2.1: Table of coefficients used in formula 2.3 copied from [6] and used in our measurements to calculate temperature from the known saturated vapor pressure.

	from 1.25 K up to 2.1768 K	from 2.1768 K up to 5.0 K
A_0	1.392408	3.146631
A_1	0.527153	1.357655
A_2	0.166756	0.413923
A_3	0.050988	0.091159
A_4	0.026514	0.016349
A_5	0.001975	0.001823
A_6	-0.017976	-0.004325
A_7	0.005409	-0.004973
A_8	0.013259	0
B	5.6	10.3
C	2.9	1.9

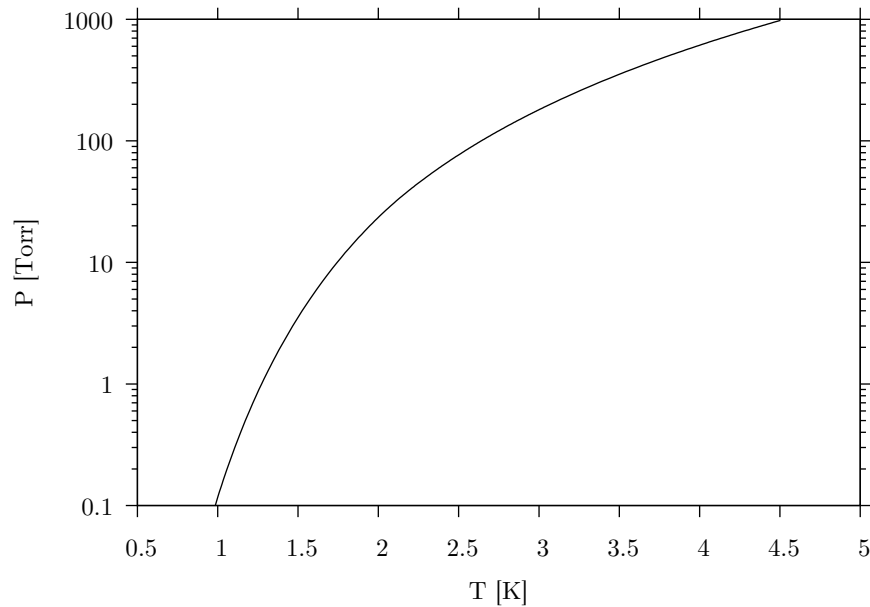


Figure 2.2: Saturated vapor pressure according to the formula 2.3 from [6].

in height of the level of liquid helium is deemed not to affect significantly the measured pressure due to the low density of gaseous helium, which is about 1.2 kg/m^3 [57], hence the shift in pressure is approximately $\Delta P = \rho g \Delta h \approx 0.07 \text{ Torr}$.

The data on pressure, resistance of thermometers (used for estimating the temperature during precooling) and heater power (used for thermal counterflow experiments) are recorded by programs written in LabView, which also enables us to switch on and off the heater, the fast needle valve for the injection of particles (see below section 2.3), as well as control of the rotation speed of the motor used for moving the obstacle (see below section 2.4). These programs were developed in our laboratory by several people working here during the implementation of the experimental set-up, including the author of this Thesis.

2.3 Seeding system

As liquid helium is a colorless and transparent substance, to visualize its motion small flow tracers are added to it. For this purpose we use solid hydrogen and deuterium particles, which are generally of sizes of few μm (see figure 2.4). To obtain these particles we inject a mixture of helium, hydrogen and/or deuterium gases into the bath at a pressure larger than that of the bath, typically 1.5 – 2.0 bar.

The density of solid hydrogen is 88 kg/m^3 [58], which is less than that of liquid helium (146 kg/m^3 at temperatures between 1.0 and 2.5 K), and solid deuterium has larger density 200 kg/m^3 [58]. The initial idea was to mix this two isotopes to obtain particles matching the density of liquid helium. It was found, however, that this is not possible, due to the fact that hydrogen isotopes have different crystallization temperatures: particles made of hydrogen and particles made of deuterium were observed, as they have different settling velocities, and it does not seem that in the ranges of used parameters buoyant particles of suitable size can be obtained. This issue has recently been solved by adding a small bottle with deuterium hydride HD, which has density in solid phase much closer to that of liquid helium. The HD particles will be used in future experiments. The presented experiments were performed by using deuterium particles, as they appeared more suitable than hydrogen for visualization purposes as they gradually settle on a bottom of the cryostat and can be reused simply by stirring them up. Hydrogen particles float on the surface of the bath and stay attached on the walls while the liquid helium is consumed for cooling, and therefore their amount rapidly decreases.

There are four high-pressure gas bottles mounted on the seeding system metallic support: the first one is filled with helium gas, the second one with hydrogen gas, the third one with deuterium gas and the last one with deuterium hydride, see figure 2.3. In the small mixing volume it is possible to mix gases at various ratios. The obtained gaseous mixture is then diluted in the big mixing volume by helium gas. This step is mainly needed to prevent the creation of a plug of solid mixture in the tube. The ratio of helium gas in the final mixture also affects the size of the obtained solid particles, together with other parameters, such as the mixture pressure and the injection velocity. Various combinations of these parameters were used and the ratio of 1 : 100 of D_2 to He yields the most suitable sized particles used in the majority of our experiments. Practical experience dic-

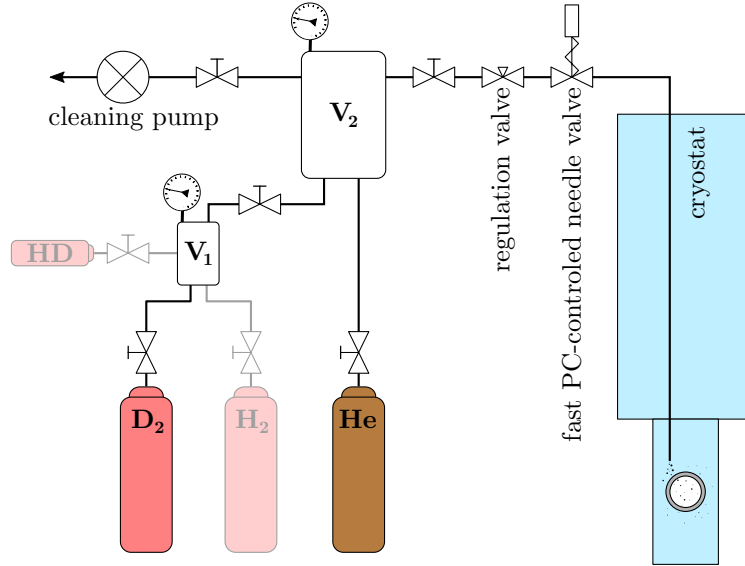


Figure 2.3: Sketch of the seeding system. The small volume V_1 is filled with deuterium D_2 (or with H_2 or HD , but these gases are not used in the presented experiments) at chosen pressure (usually 0.75 bar), then it is moved into the $50\times$ bigger volume V_2 , where the deuterium is diluted by helium, in the molar ratio $\approx 1 : 100$, i. e. the pressure has to be $2\times$ higher than in the small volume. This mixture is injected into the cryostat via regulation valve and fast computer-controlled needle valve with pulse duration of 100 ms.

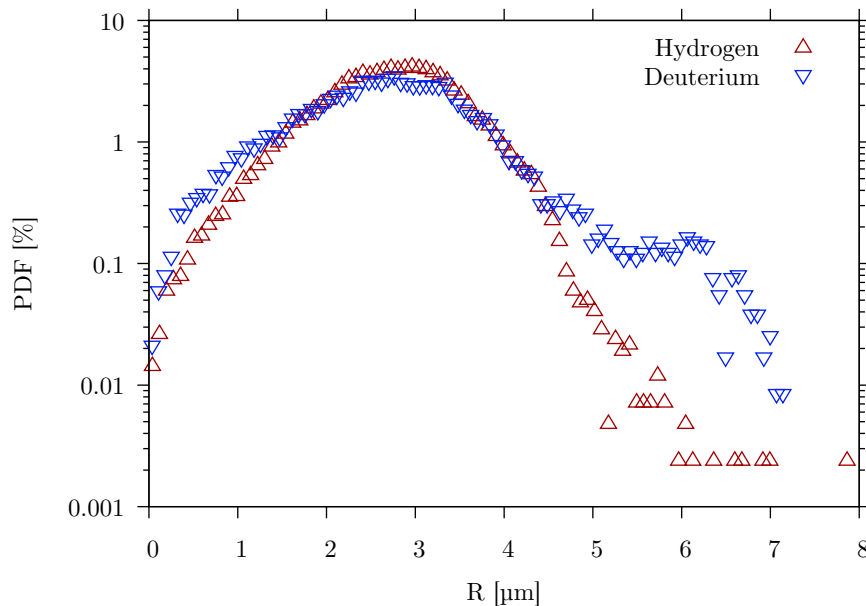


Figure 2.4: Example of distribution of particle radii obtained by their settling velocities, see equation 2.5. The red triangles pointing up represent hydrogen particles at temperature 1.65 K, while the blue triangles pointing down stand for deuterium particles measured at temperature 1.77 K, of course, in both cases the injection was done in He I at temperature about 2.2 K.

tates that the injection has to be done in He I, because, if the injection is done in He II, the particles are much bigger. Explanation of this effect is not clear, but it seems that, if injected into He II, the mixture freezes inside the injection tube, while, if injected into He I, it freezes in the bulk of liquid helium.

The size of the particles can be estimated from their settling velocities, assuming that the particles are spherical and that the *gravitational force* F_g and *buoyancy force* F_{vz} are balanced by the *Stokes drag force* F_S , due to the viscosity of the normal component of He II, i. e.

$$\begin{aligned} F_S &= F_{vz} - F_g \\ 6\pi\mu R_p v_y &= \frac{4}{3}\pi R_p^3 (\rho_{\text{He}} - \rho_p) g. \end{aligned} \quad (2.4)$$

Here μ is the dynamic viscosity of the normal component of He II, R_p indicates the radius of the particle and v_y denotes its settling velocity; ρ_{He} is the density of helium, while ρ_p denotes the density of the particle and g indicates the acceleration due to the gravity. The radius of the particle is finally obtained as

$$R_p = \sqrt{\frac{9\mu v_y}{2(\rho_{\text{He}} - \rho_p)g}}. \quad (2.5)$$

An example of distribution of particle radii calculated in this way is shown in figure 2.4.

2.4 Moving obstacle

The flow pattern past a relatively *big* and relatively *slowly* moving obstacle (chapter 4) was studied by using the obstacle in the shape of a prism, of dimensions $3 \times 10 \times 27$ mm, with the longest length perpendicular to the studied plane. It is made of plexiglass³ in order to make it transparent for laser-light illuminating the tracer particles, because in one of our previous experiments [50] we found that a non-transparent material is appreciably heated by the illuminating light, producing a *thermal counterflow* in the vicinity of the obstacle. This effect might become so strong as to interfere with and affect the studied flow.

The laser-plane crosses the prism approximately in a half of its length such that from the camera's view it looks like a rectangle. The obstacle moves parallel with its shortest (3 mm) side with amplitude of 5 or 10 mm. The prism is connected on its farther (from the camera) end to the brass support of shape of Γ , which is at its top end connected to the stainless steel thin wall tube of diameter 5 mm. At the top of the cryostat this tube is filled and passes through a pair of spring-tightened o-rings, which are at the nearly room temperature. The space between these o-rings is filled by slightly pressurized helium gas in order to avoid air going inside this volume and eventually into the cryostat⁴.

The movement of the obstacle is realized by using an accurate stepper motor made in Switzerland, whose rotational motion is transformed to the sliding motion

³Poly(methyl 2-methylpropenoate) or simplified name poly(methyl methacrylate), summary formula $(\text{C}_5\text{O}_2\text{H}_8)_n$.

⁴Air would freeze creating unexpected additional particles with different density and sizes than the used deuterium particles have.

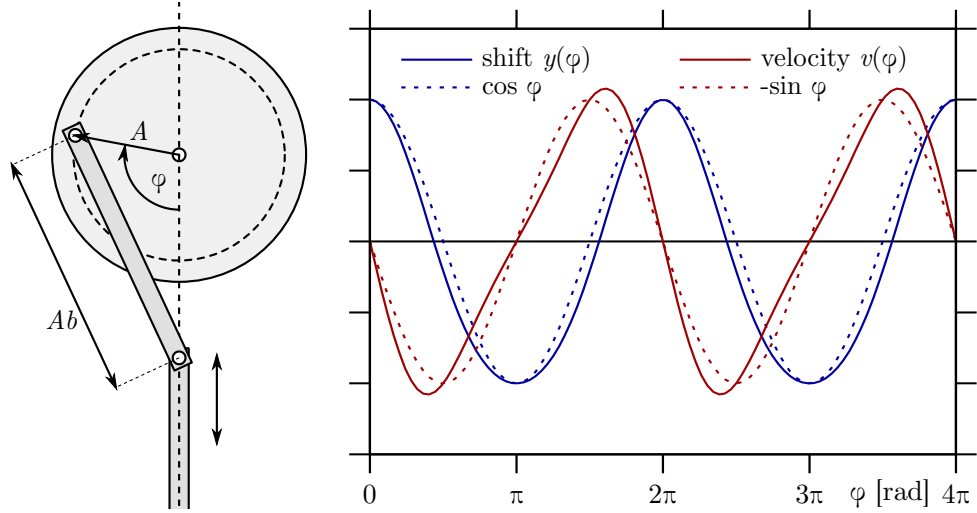


Figure 2.5: The connecting rod used for transforming the rotational motion to the sliding motion. **Left** panel: sketch of the connecting rod, $A = 5$ or 10 mm is the amplitude of the oscillations and $Ab = 25$ mm is the length of the connecting rod. **Right** panel: comparison of the ideal harmonic motion (dashed lines) with that produced by the mechanism on the left hand side (solid lines), blue color denotes the shift, while the red one the velocity.

of the obstacle by a connecting rod of fixed length of 25 mm. This mechanism transforms the ordinary rotation to the nearly harmonic slide motion. The time (phase) dependence of its vertical shift is

$$y(\varphi) = A \left(\cos \varphi + \sqrt{b^2 + \sin^2 \varphi} - b \right), \quad (2.6)$$

where φ is the current phase of the motion $\varphi(t) = \Omega t$ with the angular frequency Ω , b is the ratio of the length of the connecting rod, in our case 25 mm, and the distance of the connecting point to the axis A , which is in our case $A = 5$ or 10 mm respectively, hence $b = 5$ or 2.5 . The corresponding vertical velocity v is

$$v(\varphi) = -A\Omega \sin \varphi \left(1 + \frac{\cos \varphi}{\sqrt{b^2 + \sin^2 \varphi}} \right). \quad (2.7)$$

The comparison of functions 2.6 and 2.7 with $\sin \varphi$ and $\cos \varphi$ for the case $b = 2.5$ is shown in figure 2.5.

The motor is computer controlled, which allows us to compensate this slightly anharmonic behavior by changing the prescribed angular frequency Ω in real time in dependence on the actual phase φ read out by the sensor, which is a part of the motor. Then the motion ought to be harmonic. This option was prepared by the author of this Thesis, but in fact rarely used, because this solution is strongly dependent on the exact setting of the initial phase – a slightly incorrect initial phase causes the real motion to be more away from the ideal harmonic one than without this correction.

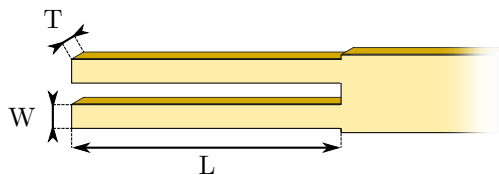


Figure 2.6: The meaning of the dimensions of the quartz tuning fork. Length $L = 9.0$ mm, width $W = 0.9$ mm and thickness $T = 0.4$ mm, for the fork used in the streaming experiment, chapter 5, the fork used for cavitation experiment has dimensions: $L = 19.7$ mm, $W = 2.2$ mm and $T = 0.8$ mm.

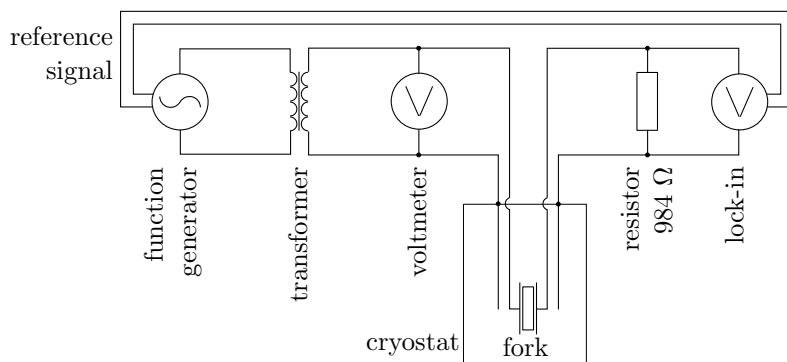


Figure 2.7: The scheme of the fork electrical connection. The alternating signal is provided by a function generator, transformed up and checked by a voltmeter. The current through the fork is measured by using a phase sensitive lock-in amplifier as a voltage drop on a $984\ \Omega$ resistor.

2.5 Quartz tuning fork

The fork used in the streaming flow experiment (chapter 5) has length $L = 9.0$ mm, width $W = 0.9$ mm and thickness $T = 0.4$ mm, see figure 2.6. The fundamental resonant frequency is $f_s = 8295$ Hz at 2.2 K, while at lower temperature 1.3 K it is $f_s = 8302$ Hz.

In the cavitation experiment (chapter 6) we have used a bigger fork with length $L = 19.7$ mm, width $W = 2.2$ mm and thickness $T = 0.8$ mm, its resonant frequency is $f_c = 4186$ Hz at 2.1 K. In none of our measurements we use higher harmonic modes.

The fork is driven electrically by using the Agilent 33210A function generator with maximum sinusoidal output voltage $7.07 V_{\text{rms}}$. This voltage is transformed up and the exact value has to be checked by using a voltmeter. The achieved transformed maximum voltage is $U_s \cong 77.5 V_{\text{rms}}$ and $U_c \cong 130 V_{\text{rms}}$ valid for the streaming experiment (chapter 5) and for the cavitation experiment (chapter 6) respectively. The shielding of coaxial cables is connected to the metallic body of the cryostat and a low-temperature coaxial cable is used also inside the cryostat and it shields each wire separately. The current through the fork is measured as a voltage drop on a $984\ \Omega$ resistor by the phase-sensitive lock-in amplifier, see figure 2.7.

The fork motion is based on the piezoelectric effect: the applied electric volt-

age U causes a mechanical tension (described as a force F), the mechanical deformation causes an electrical charge, hence the velocity of deformation v causes an electrical current I . The electromechanical properties of the fork are characterized by a so-called *fork constant* $a = \frac{2\Delta F}{\Delta U} = \frac{I}{v}$. Its knowledge is important for determining the real force F acting on the fork prongs and for estimating the approximate velocity v of the fork prong tip as

$$F = \frac{1}{2}a \cdot U, \quad (2.8)$$

$$v = \frac{I}{a}. \quad (2.9)$$

By using this formulae we can estimate the velocity only with the accuracy of around 20%, still, this is a commonly used method, see e. g. [59], [60] and many other references. Hence the maximum obtained forces in our measurements are $F_s \cong 42 \mu\text{N}_{\text{rms}}$ and $F_c \cong 2.2 \text{mN}_{\text{rms}}$, respectively.

The fork constant a is measured to be $a_s = 1.1 \cdot 10^{-6} \text{C} \cdot \text{m}^{-1}$ for the fork used in the *streaming experiment* and $a_c = 3.4 \cdot 10^{-5} \text{C} \cdot \text{m}^{-1}$ for the fork used for *cavitation experiment* by using the standard methodology [60], [61], i. e. by measuring the fork resonant curve in vacuum (an ideal case would be to measure in vacuum at low temperatures). By fitting this curve by the *Lorentz curve* we have got the resonant peak. An example resonant peak of the fork used for the *streaming experiment* is shown in the figure 2.8 with width $\Delta f = (87.6 \pm 0.2) \cdot 10^{-3} \text{Hz}$, and the current in resonance $I_{\text{res}} = (4921 \pm 6) \cdot 10^{-12} \text{A}$ (only the real part has been fitted) at the driving voltage $1 \cdot 10^{-2} \text{V}_{\text{rms}}$, hence the resistance at the maximum is $R_{\text{res}} = (2032 \pm 3) \cdot 10^3 \Omega$. Then the fork constant is calculated by using the formula

$$a = \sqrt{\frac{4\pi \cdot m \cdot \Delta f_{\text{res}}}{R_{\text{res}}}}, \quad (2.10)$$

where m is the effective mass of the fork prong and it is calculated as $m = 0.25 \cdot \rho \cdot LWT$ [61], where ρ is the density of quartz $\rho = 2659 \text{kg} \cdot \text{m}^{-3}$ and LWT is the volume of one prong by using dimensions mentioned above. Analogically for the second discussed fork.

In the *cavitation experiment* the fork velocity was determined also directly. As the fork is illuminated from its side, some point-like surface features are clearly visible. By measuring the elongation of such features when the fork moves we can estimate the amplitude of the motion, hence the velocity, see figure 2.9. The correlation coefficient is 84% with systematic dependence $v_{\text{el}} \sim 0.74v_{\text{opt}}$. We refrain from declaring which method is better.

In the streaming flow experiment, the fork is situated inside the cryostat horizontally, prongs pointing towards the camera in such a way that they are visible as a pair of rectangles, see figure 2.10. The laser sheet crosses the prongs perpendicularly close to their ends, see again figure 2.10, unfortunately, we are not able to set this distance very accurately.

In the cavitation experiment, the fork is oriented almost vertically, slanted by about 13° , prongs pointing up and the illumination laser sheet *touches* the fork from the side closer to the camera, see the left panel of figure 2.9.

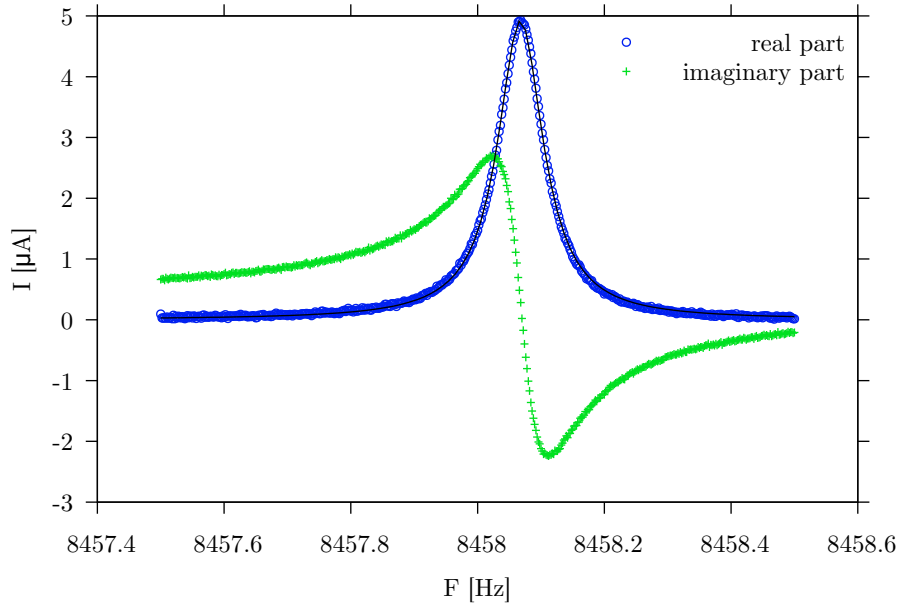


Figure 2.8: The electrical current through the fork as a function of the frequency used for the calculation of the fork constant, the applied driving voltage is $U = 10 \text{ mV}_{\text{rms}}$. The plot shows both the real (circles) and the imaginary (crosses) part of the response, where only the real part is fitted (black line) and used for calculating the fork constant.

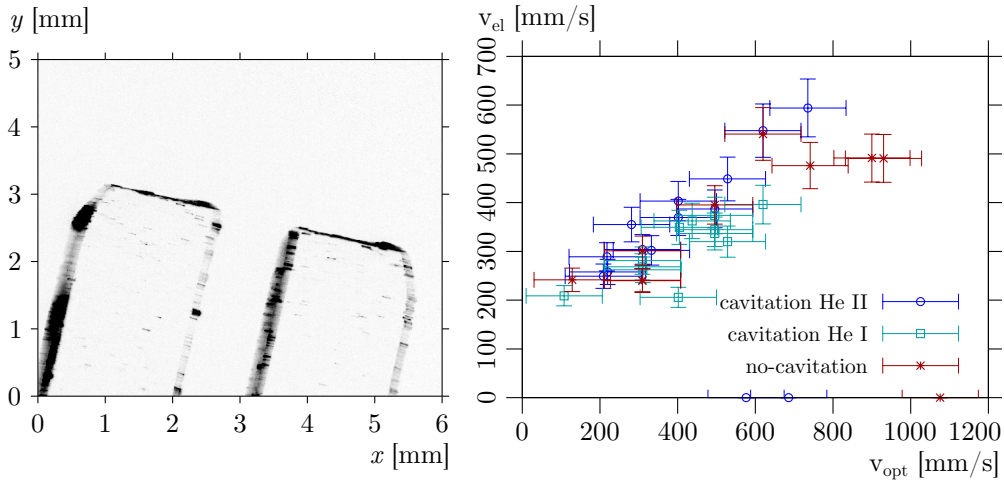


Figure 2.9: **Left:** Photograph of the fork illuminated by the laser sheet from the side, when the fork moves, which elongates the surface features in the direction parallel with the motion. **Right:** the correlation of the velocity measured by using the electrical current through the fork and the equation 2.9 v_{el} and the velocity measured optically v_{opt} . The symbols represent cases when a bubble was observed, for details see chapter 5.

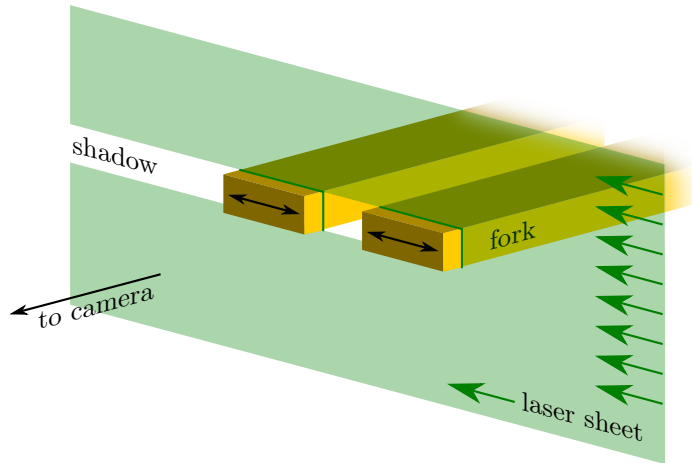


Figure 2.10: Sketch of the fork illuminated by the laser sheet in the streaming flow experiment. The thickness of the laser sheet is approximately 1 mm and it is produced from a laser beam defocused by using a cylindrical diverging lens, as described in section 2.6.

2.6 Laser and camera

To illuminate the experimental volume, a continuous wave solid state laser with tunable power RayPower 5000 is used, whose maximum power is declared by the producer to be 5 W. Its dominant wave length is 532 nm (green color). The power employed in the experiments is usually less than 200 mW in a continuous regime. Larger power enables us to see smaller particles, but it disturbs the results by generating thermal counterflow in the vicinity of surfaces heated by the incident light. This problem has been a subject of independent study and detailed quantitative results are published in article [50], which however does not fit the topic of this Thesis, although it has the same first author. On the other hand, similar effect is observed and discussed in section 5.3 and similar problem of heating the tracer particles and their acceleration due to the thermal counterflow was studied in detail experimentally and analytically by Jan Hodic in his Bachelor thesis [62]. He found that this effect is unobservable in the range of laser powers 20 – 320 mW corresponding to fluxes 400 – 6700 W/m². At larger imposed power the volume becomes overlighted due to reflections from windows and the measurement is not possible.

The laser sheet is produced by a cylindrical diverging lens from a focused laser beam, see figure 2.11. Just in front of the window, there is an aperture made of paper to avoid reflections on shiny window fringe and to limit the diverging beam in height at the outgoing window in order to allow the maximum amount of light to leave the cryostat and dissipate on a black paper far behind the window.

The optical part of the apparatus including the just described laser and the camera described below is located on heavy stone tables to reduce vibrations.

The laser can run in a *continuous regime* or in a *pulsed regime*, in which the laser shines only when triggered. This is useful in order to suppress the total amount of heat incoming into the cryostat, but the duration of this laser pulse cannot be controlled, it is always about ~ 0.4 ms, which decreases the effectivity of camera exposure.

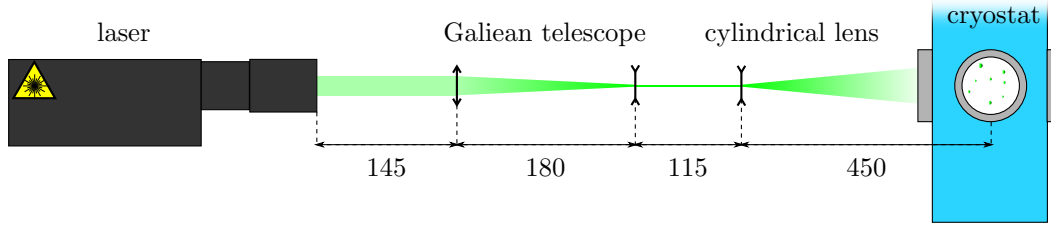


Figure 2.11: Sketch of the illumination part of the optical setup. The laser beam is focused by using a so called „Galilean telescope“ consisting of one converging and one diverging lens and then defocused in the vertical plane by using a cylindrical diverging lens ($f = -15$ mm). Units are in mm.

The used CMOS camera, Phantom v12.1, is very fast: its maximum frame rate at its maximum resolution 1 Mpix (i. e. 1280×800 pix), is 6273 Hz (or fps – frames per second). Its maximum frame rate, 1 MHz, can be achieved at the lowest resolution, 128×80 pix. The camera is situated perpendicularly to the illuminated plane and focused on the latter by using an appropriate telemetrical macro lens, which can be enhanced by using a $2\times$ extender. The field of view has dimensions of about 13×8.2 mm on the focus plane (these dimensions vary slightly, depending on the actual focusing in the experiment).

2.7 Data acquisition procedure

The Data acquisition procedure was as follows: first, there is an injection of pure helium gas from room temperature under pressure around 1.5 bar by using our *seeding system*, section 2.3. This injection stirs up the deuterium particles seeded at the bottom of the cryostat and allows us to perform the measurements. On the other hand, such injection creates a strong residual flow, therefore we have to wait until this flow is dampened, or, at least, suppressed to the level appreciably weaker than the studied flow. After this injection we start the driving of the flow by the quartz tuning fork or by the moving obstacle and some reasonable time after the injection we start acquiring images by the camera at the chosen frequency, see table 3.1 for details. The laser illuminating the particles (and the fork as well) is operated in a *pulse regime* at the same frequency as the camera, the duration of one shot is ~ 0.4 ms.

The movie usually consists of 2000 images. After this is completed, the data transfer from the camera into the computer starts, which is provided by using the commercial software Dynamic Studio, developed by the company Dantec. This software also controls the camera and laser.

2.8 Image processing

Dynamic studio stores images in its own format `image`, which is inaccessible for any other image processing software, therefore we were pushed to puzzle out its structure, which is, fortunately, very simple: the file has a header of constant length followed by the pixel intensity information of 8-bit depth organized in

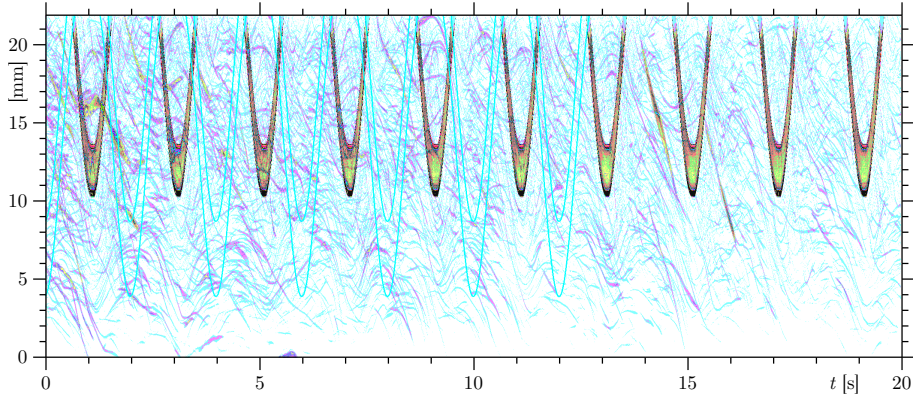


Figure 2.12: The sum over the x -coordinate (i. e. the y - t -plot) of a whole movie with the moving cylinder displayed in a standard 8-bpp-indexed palette for better contrast. The temperature is 1.32 K, the camera frame rate is 100 Hz, the frequency of the cylinder motion is 0.5 Hz. The fine azure lines drawn by the program help the user to fit the frequency phase-shift and exact y -position (x -position is not distinguishable in this view). Other (mostly azure or pink) lines are the traces of particles. The colorful periodical trace is that of the over-lighted cylinder, which has to be masked.

columns. A simple algorithm for extracting these images into a `tiff` format was developed.

The need of having a program for movable masking emerged with the experiments on the flow around the moving cylinder, see chapter 4. The parameters of the mask (its dimensions and position) and the parameters of the movement (frequency, amplitude, shape and phase-shift) have to be inserted into the program by hand, but, in order to fit these numbers, various functions are used: the sum over the x -coordinate (see example in figure 2.12), y -coordinate or $time$ -coordinate of the whole set of images.

2.9 Data processing

The Dantec software also offers a set of various techniques for data analysis but mostly we do not employ them, as we use for the implementation of the PTV technique other programs. One of them is an open-source add-on to the image analysis software ImageJ. This is called Mosaic and was developed mostly at ETH, Zurich, [63]. This algorithm finds particle positions on the images and connects them to form trajectories, on the basis of a set of chosen parameters, and finally generates a table with the particle positions.

2.9.1 Custom-made particle tracking algorithm

The author of this Thesis tried to write his own particle tracking algorithm. Although this issue was only partly successful, he was motivated mainly by the question, if the observed quantum signature in He II flows, especially the wide tails of the velocity distributions (for more detail see the authors Diploma thesis [22] or the corresponding article [64]), which are naturally *rare events*, might not be an *artifact* of the tracking algorithm.

The first part is the particle detection. We define a particle on the image as the connected area of pixels having intensity larger than a certain manually adjusted threshold. This algorithm has only one parameter: the global threshold of the pixel intensity, although we can make this threshold a local one as there are areas with less and more noise.

The most complicated issue of the described program is to connect the found particles into the trajectories across images. The algorithm of particle connecting cannot be written by using parallel computing in some simple way. It proceeds frame by frame, by adding new points to the existing trajectories. It is also possible to choose the *time-orientation* (from the first frame to the last one or from the last frame to the first one), which can, in principle, give different results.

First, the trajectory generates the expected position of a new point in the next frame, then the frame selects some point, which is the nearest to the required position, and, at the same time, has the smallest relative change of its size. Now, if some point is suitable for more trajectories, the algorithm then prefers the longer one (the possible future plans include checking this not very frequent situation more carefully). The points, which do not fit any trajectory, are the starting points of new trajectories.

This algorithm has several parameters: the maximum distance between the expected new position and the found new position, the maximum relative change of size of the particle, the number of frames, in which the trajectory looks for a new point, and finally the function for estimating the position of the new point in the trajectory.

At this moment, we have two functions for estimating the next expected point: the first variant just returns the position of the last point in the trajectory, hence the algorithm minimizes the velocity. The second variant calculates the velocity of the last point in the trajectory and uses it to obtain the new position (it means that the new position is equal to the position of the last point plus its velocity multiplied by the time between the last frame and the next one). This should minimize the acceleration of the found particles, but, in practice, it amplifies the noise.

2.9.2 Evaluation of our tracking algorithm

We mostly focused on the statistical properties of quantum turbulence, hence we are not interested in the exact shape of one particular trajectory; so the main question at this moment is: how much the choice of the algorithm affects the results from the statistical point of view? In figure 2.13 we can see that for small velocities the shape of the distribution does not depend much on the used algorithm and its parameters but at the tails of the distribution (rare events) we see strong dependence on the parameters, especially when the position of new expected point is determined by using the velocity of the last one. In addition, our algorithm produces shorter trajectories than ImageJ does, which is caused by the restrictions on particle size, and it finds less particles due to using of global threshold.

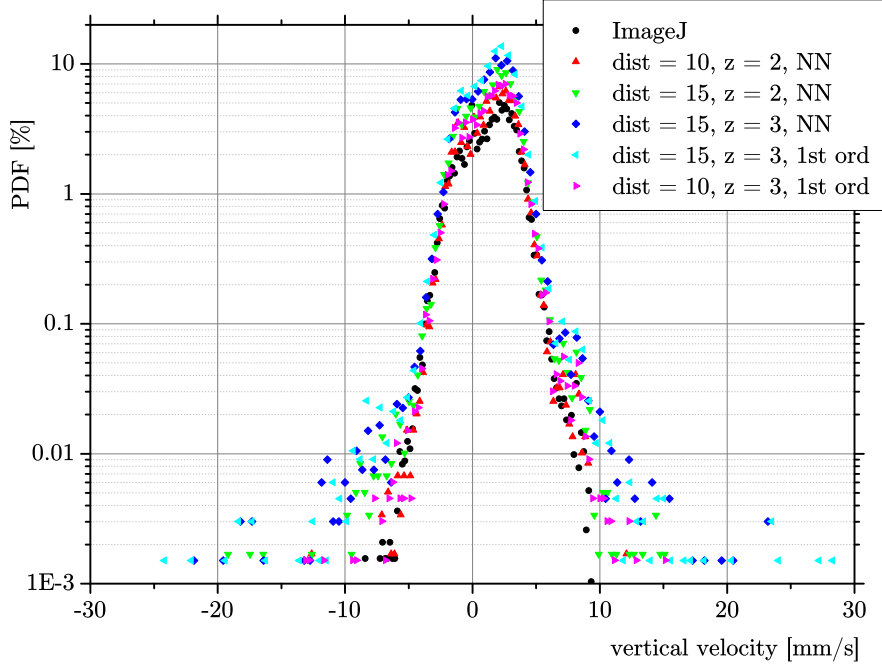


Figure 2.13: Comparison of vertical velocities of particles found by our software with those found by ImageJ. *dist* means the maximum distance between the expected new position and the found one; *z* denotes the maximum relative change of size (compared to the smaller size, so it is always greater or equal to 1). The last parameter is the used function for estimating the position of the next point – „NN“: nearest neighbor; „1st ord“: first order estimation. The shown data are taken at 1.86 K, in thermal counterflow, with a heat flux of 1700 W/m^2 ; the camera frame rate is 100 Hz.

2.9.3 Statistics over trajectories

Another program written by the author calculates the statistical distributions of velocities, accelerations, lengths and other quantities related to the connected particle positions. The table of particle positions and their connections is the input. The outputs are distributions of different parameters of that data set or subset, obtained by filtering or smoothing, which are also performed by the program.

For smoothing the input data the program uses the Kolmogorov-Zurbenko algorithm [65], which averages over a chosen number of nearest neighbors along the trajectories. Important procedure is adding missing points into the trajectories, which is done by the simplest possible way – linear extrapolation from the nearest neighbors positions.

The velocity \vec{v} is calculated numerically in Cartesian coordinates or in local polar coordinates in a time-symmetric or time-asymmetric way with controlled time-step Δt , which was useful in the work [66] studying the transition from quantum distribution to the classical one by changing this parameter of velocity calculation. Hence, the velocity of *i*-th point of the trajectory is calculated in

these two ways:

$$\begin{aligned}\vec{v}_i &= \frac{\vec{r}_{i+\Delta i} - \vec{r}_{i-\Delta i}}{t_{i+\Delta i} - t_{i-\Delta i}}, \\ \vec{v}_i^a &= \frac{\vec{r}_{i+\Delta i} - \vec{r}_i}{t_{i+\Delta i} - t_i},\end{aligned}\tag{2.11}$$

where i denotes the index in respect to the actual trajectory, the superscript a means that the velocity is calculated in an asymmetric way. Note that the first way already contains some smoothing. The first and last point of the trajectory are undefined and they do not contribute for the statistical calculations. The program also computes particle accelerations in an analogical way.

The main issue of this program is to calculate the statistical properties of the set, namely the *standard deviation*, the *skewness* and the *flatness* of all trajectory point quantities and plotting the whole distribution (of-course determined numerically for the chosen number of bins). Advanced statistical functions are the Lagrangian *autocorrelation function* $A[q](\tau)$ and *structure function* $S^n[q](\tau)$ of any natural order $n \in \mathbb{N}$:

$$\begin{aligned}A[q](\tau) &= \langle q(t+\tau)q(t) \rangle, \\ S^n[q](\tau) &= \langle |q(t+\tau) - q(t)|^n \rangle,\end{aligned}\tag{2.12}$$

where q is the chosen quantity of the trajectory point and τ is the time step.

A special care has been taken on the very important issue – the filtering. The filter consists of many independent small filters, which filter according to any feature of the individual trajectory point and the possible logic with respect to the trajectory can be chosen from following set:

- each point is assessed individually;
- whole trajectory passes, if at least one point of the trajectory passes;
- whole trajectory is blocked, if at least one point of the trajectory is blocked;
- whole trajectory passes, if 50% of trajectory points has to pass;
- whole trajectory passes, if the mean of trajectory passes.

The term „pass“ means to fit inside or outside of a chosen interval. In addition, *conditional checking* is implemented, i. e., the small filter applies or not according to another small filter (or set of filters).

While writing the Thesis, various special needs emerged to be useful part of this program, e. g. the calculation of vortex profiles (section 4.3) or the PTV-based pseudovorticity discussed in the following section.

2.10 PTV-based pseudovorticity

2.10.1 Regular vorticity

In the fluid-dynamic community, it is customary to use, among others, the *vorticity* $\vec{\omega}$ in order to characterize the flow, e. g. [67]. It is introduced by the

first *Helmholtz theorem*, which states that each movement of the fluid in an infinitesimal neighborhood of a chosen point is separable into *velocity of translation* v_i , *velocity of deformation* \dot{e}_{ik} and *velocity of rotation* $\dot{\omega}_{ik}$, that is

$$v'_i(x_j + dx_j) = v_i(x_j) + \dot{e}_{ik}(x_j) dx_k + \dot{\omega}_{ik}(x_j) dx_k, \quad (2.13)$$

where the antisymmetric tensor $\dot{\omega}_{ik}$, can also be seen as a pseudovector of *rotation*,

$$\omega_i = \epsilon_{ijk} \dot{\omega}_{jk} = \frac{1}{2} \epsilon_{ijk} \left(\frac{\partial v_j}{\partial x_k} - \frac{\partial v_k}{\partial x_j} \right) \xrightarrow{\text{antisym.}} \epsilon_{ijk} \frac{\partial v_j}{\partial x_k} = (\nabla \times \vec{v})_i \quad (2.14)$$

or simply

$$\vec{\omega} = \nabla \times \vec{v}. \quad (2.15)$$

It is possible to write the *Navier-Stokes equation* for the vorticity by applying the rotation operator as⁵:

$$\frac{D\vec{\omega}}{Dt} - (\vec{\omega} \cdot \nabla) \vec{v} = \nu \nabla^2 \vec{\omega}, \quad (2.16)$$

where $\frac{D\vec{\omega}}{Dt} = \frac{\partial \vec{\omega}}{\partial t} + (\vec{v} \cdot \nabla) \vec{\omega}$ is the material derivative. Equation 2.16 together with the continuity equation, which is fulfilled for vorticity identically, shows, that the amount of vorticity can be changed only via the viscosity mechanisms, or via the process called *vortex stretching*, linked with the second term of 2.16. Therefore, its presence is a signature of certain *flow patterns* (vortices, shear layers, etc.) or *flow processes* (vortex stretching, boundary layer separation, etc.).

In a shortcut, the spatial distribution of vorticity and its magnitude can be very interesting for describing the studied flow, especially, if we believe, there would be macroscopic vortices. Unfortunately, due to the character of our data, which are in the form of individual particle trajectories, we are not able to calculate the vorticity ω directly according to the definition 2.14, as we do not know the fluid velocity everywhere at any time, but only along the trajectories and at times of particle passing. In addition, there is the problem with the two-fluid character of the He II flows.

2.10.2 Definition of pseudovorticity

Hence we introduce an experimentally observable *approximation*. We do not venture to identify it with the proper vorticity, therefore we call it *PTV-based pseudovorticity* and we denote it ϑ :

$$\vartheta(\vec{r}; t) = \left\langle \frac{(\vec{r}_i - \vec{r}) \times \vec{v}_i}{|\vec{r}_i - \vec{r}|^2} \right\rangle_{|t-t_i| < T, |\vec{r}_i - \vec{r}| < R_m}, \quad (2.17)$$

where \vec{r} and t denote the probed point position and time, \vec{r}_i and t_i stand for the position and time of i -th trajectory point, while \vec{v}_i is its velocity. The vector product \times results into a *scalar* as our vectors are only two-dimensional projections or cuts of the real ones. The averaging is calculated only over such points, which

⁵The advective term $(\vec{v} \cdot \nabla) \vec{v}$ has been rewritten as $\frac{1}{2} \nabla |v|^2 - \vec{v} \times \omega$ and rotation operator $\nabla \times$ has been applied; for more details see any book of fluid mechanics, e. g. [68].

are located inside a circular area of chosen radius R_m and centered at the probed point \vec{r} . T is the duration of a time window centered at the probed time t .

Equation 2.17 is the general definition, however, in the experiment with large slowly oscillating obstacle, chapter 4, we have used a *phase* of the obstacle motion instead of time, while in the streaming experiment, chapter 5, we did not care about time anymore, as the time resolution represented by the camera frame-rate was $\sim 10\times$ longer than the oscillation period and therefore we observed *only* the steady component of the particle motion.

2.10.3 Convergence

Intuitive arguments for the construction of definition 2.17 are:

1. For the lack of better approach we *have to* consider that the set of trajectory point velocities $\{\vec{v}_i\}$ are selected points of a *continuous* velocity field⁶, in other words, $\sum \int \vec{v}_i \cdot d^2\vec{r} = \sum \int \vec{v}(\vec{r}) \delta(\vec{r} - \vec{r}_i) d^2\vec{r}$, \vec{r}_i being the positions of points with velocities \vec{v}_i and \vec{v} is continuous.
2. The vector product $\frac{(\vec{r}_i - \vec{r})}{|\vec{r}_i - \vec{r}|} \times \vec{v}_i$ represents the magnitude of the projection of velocity v_i into direction perpendicular to $(\vec{r}_i - \vec{r})$, i. e. projection to a uniform spin around point \vec{r} .
3. The second $|\vec{r}_i - \vec{r}|$ in the denominator of definition 2.17 compensates the geometrical fact that the amount of points in an annulus increases linearly with the radius of such an annulus.
4. The studied flow is steady (at least locally), therefore we do not care about the fact that ω is an Eulerian quantity, while the velocities along trajectories are Lagrangean quantities.
5. The physical unit of ϑ is $[\text{s}^{-1}]$, which is the same as the unit dimension of regular vorticity ω .

To prove that under certain conditions ϑ converges to ω , let's start with the circulation Γ and its relation with $\omega = \nabla \times \vec{v}$ due to the *Stokes theorem*:

$$\Gamma = \oint_{\partial\mathfrak{A}} \vec{v} \cdot d\vec{\partial\mathfrak{A}} = \int_{\mathfrak{A}} \nabla \times \vec{v} d\mathfrak{A}, \quad (2.18)$$

where \mathfrak{A} is an area, e. g. $\mathfrak{A} = \{\vec{\rho} \in \mathbb{R}^2, |\vec{\rho} - \vec{r}| < R_m\}$, or, if approximating⁷ real numbers \mathbb{R} with rational numbers \mathbb{Q} , $\mathfrak{A} = \{\vec{\rho} \in \mathbb{Q}^2, |\vec{\rho} - \vec{r}| < R_m\}$, then $\vec{\rho}$ can be indexed by $i \in \mathbb{N}$ and therefore we can substitute the integration in the second equality in 2.18 by summation over corresponding i and integration over whole plane \mathbb{R}^2 :

$$\Gamma \approx \frac{1}{M} \int_{\mathbb{R}^2} \sum_{i, \vec{r}_i \in \mathfrak{A}} (\nabla \times \vec{v}_i) \delta(\vec{r}_i - \vec{r}) d^2\vec{r} = -\frac{1}{M} \int_{\mathbb{R}^2} \sum_{i, \vec{r}_i \in \mathfrak{A}} \vec{v}_i \times \nabla \delta(\vec{r}_i - \vec{r}) d^2\vec{r}, \quad (2.19)$$

⁶It is not necessary to be equal to the flow velocity field, which would be fulfilled in the case of tracking hypothetical *fluid particles*.

⁷Although this looks terrible for mathematicians, physics does not distinguish those sets.

where M is the number of points \vec{r}_i . The second equality is a standard step in the *theory of distributions*. Gradient of δ -function is commonly used and it equals, in the sense of distributions, in two-dimensional space, to

$$\nabla \delta(\vec{r}_i - \vec{r}) = \frac{\vec{r}_i - \vec{r}}{|\vec{r}_i - \vec{r}|^2}. \quad (2.20)$$

Therefore we have

$$\Gamma \approx -\frac{1}{M} \int_{\mathbb{R}^2} \sum_{i, \vec{r}_i \in \mathfrak{A}} \vec{v}_i \times \frac{\vec{r}_i - \vec{r}}{|\vec{r}_i - \vec{r}|^2} d^2 \vec{r} \quad (2.21)$$

and by using the ϑ definition 2.17 we get

$$= \int_{\mathbb{R}^2} \vartheta(\vec{r}) d^2 \vec{r} \quad (2.22)$$

and therefore in the sense of distributions and within the classical limit $\Gamma \rightarrow \omega$ for $\mathfrak{A} \rightarrow$ point we have

$$\vartheta(\vec{r}) \xrightarrow{R_m \rightarrow 0} \omega(\vec{r}). \quad (2.23)$$

2.10.4 Discussion of conditions

We summarize the conditions used above:

1. dense sampling (as dense as \mathbb{Q} samples \mathbb{R}),
2. \vec{v}_i being samples of a *continuous* field,
3. $R_m \rightarrow 0$.

In practice, none of these conditions is fulfilled.

The violation of the first and the third conditions is closely connected. First: the sampling is limited by the number of tracked particles, which, as we believe, is better to keep lower, because, in the opposite case, serious problems can arise with the trajectory connections, which (and this is the worst) do not need to be distinguished during the data processing. Therefore, in the final data, there is lot of „white places“, whose size limits the integration area size R_m . Let's imagine an extreme case, that inside the region used for calculating ϑ there is only one trajectory point, then $\vartheta(\vec{r}) = \frac{(\vec{r}_1 - \vec{r}) \times \vec{v}_1}{|\vec{r}_1 - \vec{r}|^2}$ and this value is just a random number not representing vorticity.

The violation of the second condition is connected not only with the two-fluid nature of He II, but more significantly with the behavior of non-fluid particles carried by the flow. But, in the case of classical liquid, we could, at least, *except* that for small buoyant particles their velocities would be *close enough* to the continuous flow velocity field. Hence, in the case of He II, we have to use as an assumption one of our main long-term result, namely, that is that He II behaves as a single fluid in all cases, where is no reason for different forcing of individual components (i. e. by viscosity near walls or by heat gradients), and that the two-fluid behavior is displayed in bulk co-flow only at small length-scales.

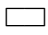
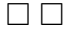

In addition, there is the problem with the time locality. The regular vorticity is naturally an Eulerian quantity, while trajectories and their properties

are Lagrangean quantities. In the streaming experiment, chapter 5, this is bypassed by studying only the steady component of the particle motion. In the case of slowly oscillating obstacle, chapter 4, we assume that the problem is locally steady within phase window of 15° , which is a compromise between the precision and the statistical quality.

Chapter 3

Table of parameters

Table 3.1: Comparison of experimental conditions of three main experiments performed by the author. The *viscous penetration depth* $\delta = \sqrt{2\nu/\Omega}$, where we set $\nu = \kappa/6$ according to [69] and $\Omega = 2\pi f$, where f is frequency. The *fork constant* is calculated according to the formula 2.10. The velocity is the *root-mean-square*-value, therefore, in the case of the Obstacle experiment, $v_{\max} = A \cdot \Omega_{\max}/\sqrt{2}$, when the fork is used, this velocity is measured via the electrical current according to the formula 2.9, hence it is naturally rms; for the sake of clarity the peak maximum velocity is added, too.

.	unit	Obstacle	Streaming	Cavitation
Temperature range T	[K]	1.3 – 2.18	1.3 – 2.22	2.14 – 2.24
Tracer particles		D ₂	D ₂	.
Camera frame-rate	[Hz]	100	800	400
Scale factor	[$\mu\text{m}/\text{pix}$]	27.4	10.33	10.56
Obstacle shape				
– visible size	[mm]	10 × 3	0.9 × 0.4	2.2 × 19.7
– third size	[mm]	30	9.0	0.8
Obstacle frequency f	[Hz]	0.05 – 1.25	8298 – 8303	4186
Amplitude A	[mm]	5; 10	up to 0.01	up to 0.05
Maximum rms velocity v_{\max}	[mm/s]	55.5	338	1075
Maximum velocity v_{\max}	[mm/s]	78	478	1520
Velocity changed by		frequency	force	force
Fork constant a	[C/m]	.	$1.1 \cdot 10^{-6}$	$3.4 \cdot 10^{-5}$
Viscous penetration depth δ	[μm]	64 – 730	0.8	1.1

Various flows of fluids at different length- or velocity-scales can be successfully characterized by carefully chosen *dimensionless numbers*, such as the *Reynolds number* Re generally defined as

$$Re = \frac{s \cdot v}{\nu}, \quad (3.1)$$

where s denotes a *characteristic size* of the problem – it can be the size of an obstacle, the size of a channel, etc. Similarly, v stands for a *characteristic velocity*

ity of the fluid and its declaration again strongly depends on careful judgment. Finally, the effective viscosity ν is again difficult to choose due to the two-fluid description of He II. Alternatively, Re can be seen as a ratio of inertial to friction forces, which suggests the interpretation of its magnitude – flows of small Re are dominated by the viscosity, while at large Re the non-linear advection and stretching processes are important, leading to *turbulence*.

The choice of characteristic sizes of the flow can be justified by various ways. For consistency, we have chosen the visible size perpendicular to the obstacle motion, explicitly, in the case of the study of flow past a slowly moving obstacle, chapter 4, it is the obstacle width $s = 10$ mm, and in the case of the study of the streaming pattern, chapter 5, it is the thickness of the fork $s = 0.4$ mm.

The Reynolds number is a suitable parameter describing steady flows. The discussed here oscillatory flows have to be characterized by a pair of dimensionless parameters.

One example of such a dimensionless parameter is the *Strouhal number*, named after the former professor active at our University Čeněk Strouhal and defined as

$$St = \frac{s\Omega}{v} = \frac{s}{A}, \quad (3.2)$$

where s is the just discussed characteristic size, Ω is the oscillation angular frequency and v is a characteristic velocity, which is, in the case of flow forced by an oscillating obstacle, $v = \Omega A$, where A is the oscillation amplitude. St was originally dedicated for describing a little bit different flow problem: the self-induced oscillations of an obstacle in a stream, therefore, the angular frequency of oscillations was a measurable result, not a control parameter.

Similarly to the *Strouhal number*, there exists a *Keulegan-Carpenter number* K_C [70] defined as

$$K_C = \frac{2\pi A}{s}, \quad (3.3)$$

where again A and s are the amplitude and the characteristic size, respectively. A similar parameter ϵ is introduced by the community studying viscous streaming [71]:

$$\epsilon = \frac{A}{s}, \quad (3.4)$$

which differs from K_C only by a factor of 2π and at the same time $\epsilon = 1/St$.

Second parameter to make a pair is the *Stokes number* β defined as

$$\beta = \frac{fs^2}{\nu}, \quad (3.5)$$

where f is the oscillation frequency and ν is the kinematic viscosity. Chong et al. [43] define the *Reynolds number* \widetilde{Re} in a similar way, which again differs from the *Stokes number* β only by a factor of 2π

$$\widetilde{Re} = \frac{\Omega s^2}{\nu}, \quad (3.6)$$

where $\Omega = 2\pi f$. We have used a „tilde“ to avoid misunderstanding while talking about Reynolds number. The Chong’s argument why to understand \widetilde{Re} as a Reynolds number is that, in the case of large $St = s/A$, the fluid has to be

Table 3.2: Dimensionless numbers characterizing discussed experiments. For details in definitions, see the text. For those dimensionless numbers, which are defined by using *viscosity*, the approximate value $\nu = \kappa/6 = 1.66 \cdot 10^{-8} \text{ m}^2/\text{s}$ is used. The peak values of velocity and amplitude are used as needed.

.	Obstacle	Streaming
Strouhal number St	1; 2	44; 82
Keulegan-Carpenter number K_C	3.1; 6.3	$(8; 14) \cdot 10^{-2}$
$\epsilon = 1/St = K_C/2\pi$	0.5; 1	$(1.2; 2.3) \cdot 10^{-2}$
Stokes number β	$(3 - 75) \cdot 10^2$	$8 \cdot 10^4$
$\widetilde{Re} = 2\pi\beta$	$(2 - 47) \cdot 10^3$	$5 \cdot 10^5$
Reynolds number Re	$(0.9 - 38) \cdot 10^3$	$(6; 12) \cdot 10^3$
Streaming Reynolds number Re_s	$(0.5 - 38) \cdot 10^3$	75; 260

transported from one side of the obstacle to the opposite one around whole obstacle in one half-period, hence the characteristic velocity is $v \sim \Omega s$. Both pairs of dimensionless numbers remain consistent in the way that

$$Re = K_C \beta = \frac{\widetilde{Re}}{St} = \frac{\Omega A s}{\nu}. \quad (3.7)$$

In the case of a steady streaming, the *streaming Reynolds number* Re_s is introduced [72]:

$$Re_s = 2\pi \frac{\beta}{St^2} = \frac{\Omega A^2}{\nu} \quad (3.8)$$

and it characterizes the streaming pattern. At small Re_s , the steady flow creates a single boundary layer with open cells, while at larger ones ([73] reports $Re_s \rightarrow 37$ as the critical one) the streaming cells close and the outer streaming pattern arises. See the illustration in figure 3.1 and the introductory section 5.1.

Table 3.2 summarizes ranges of dimensionless numbers in two our visualization experiments and figure 3.1 shows them in the phase diagram of $St \times \beta$ together with the regions known from classical experimental and theoretical works as summarized in [74] (which presents this diagram in the $St \times Re$ axes).

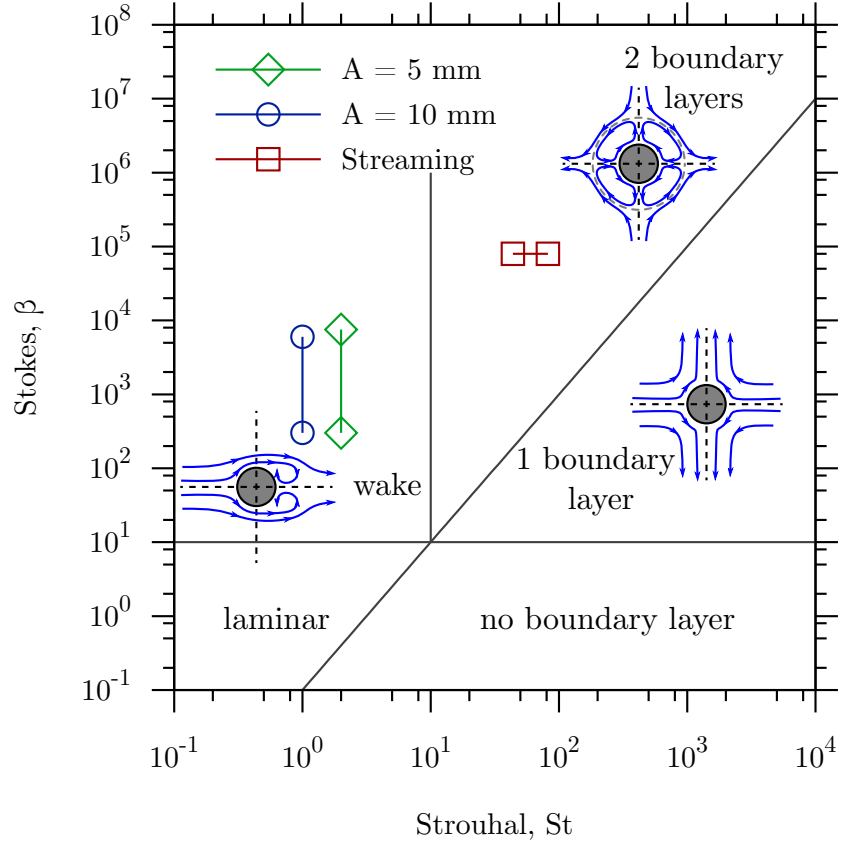


Figure 3.1: Phase diagram of oscillatory flows in the $St \times \beta$ space, *Strouhal number* $St = s/A$, 3.2 and *Stokes number* $\beta = fs^2/\nu$, 3.5. Regions are denoted according to [74]. Green squares and blue circles denote the moving obstacle experiment, see chapter 4, red squares represent the streaming experiment, see chapter 5. Diagonal line corresponds to *streaming Reynolds number* $Re_s \sim 1$ separating region with a single boundary layer from that with two boundary layers.

Chapter 4

Oscillating obstacle

4.1 Introduction

The flow past a bluff body is, for the case of cylinder, an often studied case, see, e. g., the review [75], describing various regimes of the wake behavior in dependence on the Reynolds number Re :

- Laminar Steady Regime ($Re < 49$), more details in [76],
- Laminar Vortex Shedding ($50 < Re < 140 - 195$), see [77],
- Wake Transition Regime ($Re \in [190, 260]$), [78],
- Regime of increasing disorder in the fine-scale three-dimensionalities, [79],
- Shear Layer Transition Regime ($Re \in [10^3, 2 \cdot 10^2]$), PIV measurement [80],
- Asymmetric Reattachment (or Critical transition), meaning reattachment of the separation bubble on only one side of the body, [81],
- Symmetric Reattachment (or Supercritical Regime), [82],
- Boundary Layer Transition Regime (or Postcritical Regime), the boundary layer on the cylinder surface becomes turbulent, however, in [83] an evidence of periodic vortex shedding is observed even in this regime.

This shows the beauty of the Nature, as there is such a diversity of regimes for for such a relatively „simple“ problem.

Oscillatory flows of viscous fluids are generally more complicated than steady flows because a second length scale emerges in addition to the linear size of the obstacle - the viscous penetration depth $\delta = \sqrt{(2\nu)/\Omega}$, where $\Omega = 2\pi f$ is the angular frequency of oscillations; thus two dimensionless parameters are needed to describe the flow. The viscous flow past an oscillating body is different from that past uniformly moving body [84], especially in the case when the amplitude is not much greater than the *formation length* of the wake [85], as the wake cannot develop. The importance of the amplitude has been expressed by Keulegan and Carpenter [70], who introduced what is now known as the *Keulegan-Carpenter number*, which can be identified with the Strouhal number in the case of forced oscillations, see equations 3.2 and 3.3, but in the fluid dynamics community

the difference is respected in the sense that the Strouhal number describes the oscillatory *response* of the system. In the article [86] Taneda and Honji studied the wake past a plate oscillating in the direction perpendicular to its plane, which is definitely closer to our case than the case of the circular cylinder, as the curvature of the surface is important in the vortex formation, see, e. g., Tao [87]. Phan [67] used the vorticity calculated from the particle motion for characterizing the flow patterns past oscillating cantilevers.

Flows of He II due to oscillating structures (which are widely used in quantum turbulence research since the discovery of superfluidity, see Vinen and Skrbek [88] or their review [89]) have not yet been extensively investigated by visualization methods. This situation holds despite the fact that these techniques have already been tested in experiments performed in Prague [90], besides of qualitative results of Luzuriaga [91], [92], and the time is ripe in order to adequately analyze this important class of flows of liquid ^4He , in order, for example, to clarify the mechanisms of vortex generation at the oscillator's edges.

This and the following chapters aim at giving a meaningful contribution to this promising line of scientific inquiry by visualizing the flow in the proximity of a prism of rectangular cross section, oscillating in the quiescent liquid. Such a shape of the oscillator was specifically chosen due to its similarity to the shape of quartz tuning fork prong – the most common oscillators presently employed in quantum turbulence studies [89], and to enhance the possibility of observing large-scale vortices, compared to a circular cross section.

The macroscopic vortices or vortical structures in quantum flows have been already observed: in the wake behind a cylinder by Chagovets and Van Sciver [93]; in the form of vortex rings by Murakami et al. [94], for a mechanically generated flow; and by Stamm et al. [95], for a thermally driven jet flow; see also the influential work by Zhang and Van Sciver [52] on thermal counterflow past a circular cylinder.

4.1.1 Brief setup description

The detailed description of our experimental setup was given above in chapter 2. Here we present only a short recapitulation for clarity. The measurement PTV technique is used with solid deuterium particles. The flow is generated by a oscillating solid transparent obstacle, of the shape of a prism, with dimensions $30 \times 10 \times 3$ mm, with oscillation frequencies $0.05 - 1.25$ Hz and amplitudes 5 or 10 mm. The longer side of the obstacle points to the camera and it is illuminated from the side by a laser sheet produced by a solid state laser, whose beam is defocused in the vertical direction. The laser sheet crosses the obstacle approximately in the middle of its length. The obstacle is moved by a motor via a *connecting rod*, hence the motion is not strictly harmonic, see section 2.4 for more details.

The data acquisition procedure is as follows (assuming that the deuterium particles had already been created in the helium bath by a procedure described above): First, there is an injection of pure helium gas from room temperature under pressure around 1.5 bar by using our *seeding system*, section 2.3. This injection stirs up the existing deuterium particles seeded at the bottom of the cryostat and allows us to measure. On the other hand, such an injection creates a strong residual flow, therefore we have to wait until this flow is dampened,

or, at least, suppressed to the level substantially weaker than the studied flow. We then start moving the obstacle and acquiring images by the camera at the frame-rate 100 Hz. The laser illuminating the particles (and the obstacle as well) is operated in the *pulse regime* at the same frequency as the camera. The movie usually consists of 2000 images, hence its length is 20 s. When the recording is completed, the data transfer from the camera into the computer begins.

The obtained gray-scale images are masked by using the program [96] written by the author of this thesis in order to eliminate the overlighted moving obstacle and reflections around it. The particle's images are found and connected into trajectories by using a open-source program ImageJ [63], for more details see the chapter 2.

4.2 Observations

4.2.1 Phase averaging

In order to increase the *statistical quality* of the obtained data sets, the method called *phase averaging* is utilized. It uses periodicity of the driving force, which, as one may expect, should also cause periodicity of the response, i. e., $f(t) \approx f(t + T)$, where $f(t)$ is the state of the system at the time t and T is the period of the driving force. It is then possible to merge the data with the same phase, constructing the function $g(t) = \sum_i f(t + iT)$, which can be seen as a function of the *phase* ϕ , $g(\phi) = g(2\pi t/T)$. One example is shown in figure 4.1, where the traces of deuterium particles with the phase $\phi \approx 90^\circ$ are drawn, near the bottom dead center of the obstacle motion. It is not a-priori evident that the *phase averaging* should work, because, strictly speaking, the problem is non-linear, especially near the beginning of the motion (the movies start usually 30 s after the start of the obstacle motion). It is therefore purely experimental observation that the phase averaging works; in fact it works quite well in He II and perhaps a little bit worse in He I (will be discussed bellow).

Figure 4.1 shows a pair of macroscopic vortices shed in the wake behind the moving obstacle in its bottom position, i. e. when the obstacle stops and reverses its direction of motion. These data are taken at temperature 2.18 K in He I, which is a *classical* liquid, the corresponding Reynolds number is $Re = 9 \cdot 10^3$. The same obstacle, same frequency and amplitude lead to the result displayed in figure 4.2, which was taken in He II – a *superfluid quantum liquid*.

Pairs of macroscopic fluid vortices of size comparable to the obstacle size can be inferred from the observed trajectories of deuterium particles, both in He I (figure 4.1) and He II (figure 4.2). The vortical structures seem to be similar to those observed in the proximity of flat plates accelerating in viscous fluids, as observed by Taneda [86]. However, the large-scale vortices generated in He II appear to be more evident than those shed in He I, which is caused by two reasons: First, there are stronger residual flows in He I caused by the helium gas injection steering the particles sedimented at the bottom of the cryostat; second, there are less particles (or the number density of particles) due to larger liquid volume at the earlier stages of the experiment, when we usually study the higher temperatures. We usually try to adapt seeding settings for the best data quality at the lower temperatures, which are more relevant for emphasizing quantum

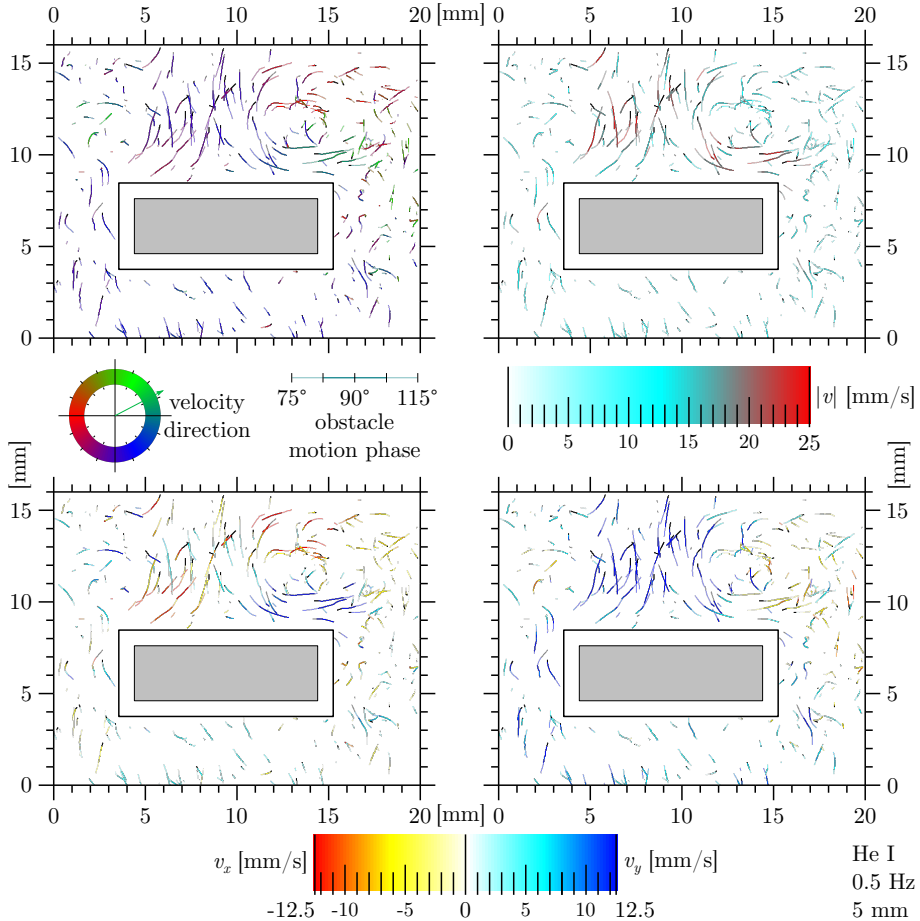


Figure 4.1: Trajectories of seeding particles in He I at temperature 2.18 K around the obstacle moving with frequency $f = 0.5$ Hz and amplitude $A = 5$ mm. The trajectories are *phase averaged* and only those recorded near the bottom obstacle position, with phase $\phi = 90^\circ \pm 15^\circ$, are displayed (those with phase $90^\circ \pm 8^\circ$ are shown in darker colors). All panels show the same data colored via the direction of velocity, the velocity magnitude and horizontal and vertical component of velocity, respectively. The gray rectangle represents the obstacle of dimensions 10×3 mm, while the bigger one does the mask used during the data processing.

features of the flow.

Unsteady flows of viscous fluids can often be characterized by the *vorticity* $\vec{\omega}$, which is a local derivative of the velocity field \vec{v} of the fluid, $\vec{\omega}(\vec{r}) = \nabla \times \vec{v}(\vec{r})$. This approach was used, for example, by Tao [87]. This (local) quantity can be seen as a measure of the vortex strength in the flow field of interest. It is a *pseudovector* and therefore it can be seen, in three-dimensional space, as a *vector*, or, in two-dimensional cut, as a *scalar*.

The vorticity cannot consequently be computed in our case, due to the fact that the fluid velocity is not known everywhere at a given time, but only along the trajectories; in addition, we do not measure the fluid velocity, but the particle velocity. In order to quantify the magnitude of the shed vortices, we have used the PTV-based pseudovorticity ϑ introduced in section 2.10, which we hope is closely related to the flow vorticity ω , more precisely, to its component perpendicular to the studied plane.

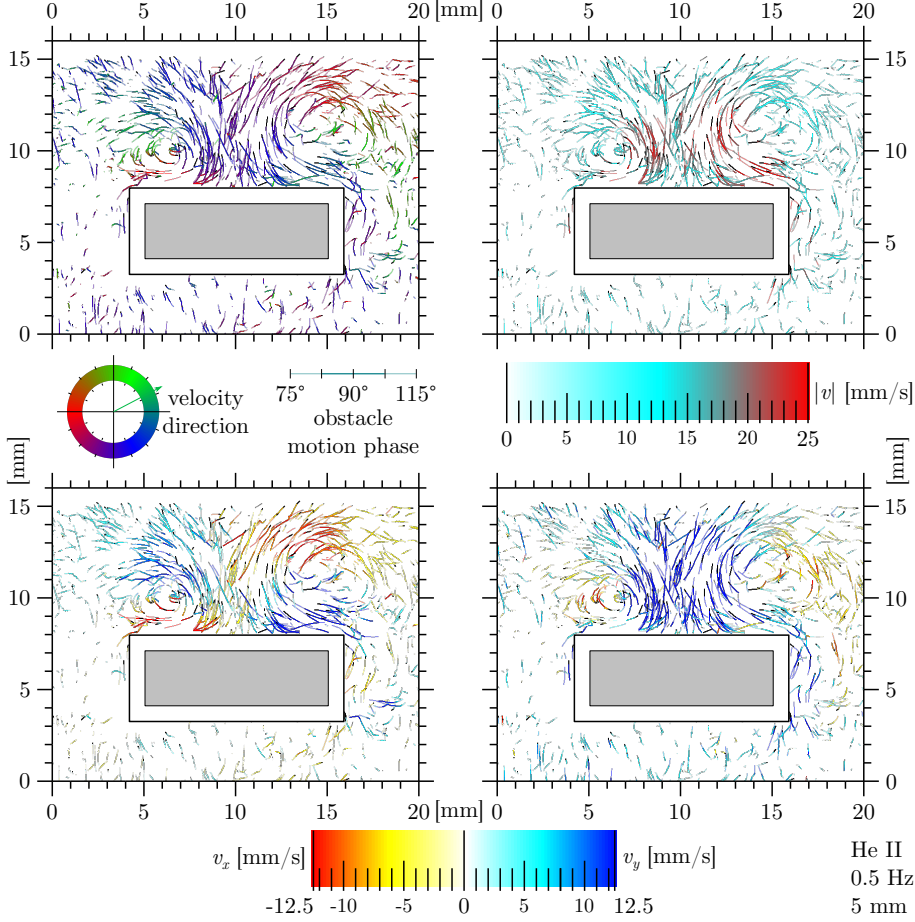


Figure 4.2: Trajectories of seeding particles in He II at temperature 1.24 K around the obstacle moving with $f = 0.5$ Hz and $A = 5$ mm. The trajectories are *phase averaged* and only those near the bottom most obstacle position with phase $\phi = 90^\circ \pm 15^\circ$ are displayed, and those with phase $90^\circ \pm 8^\circ$ are shown in darker colors. All panels show the same data colored via the direction of velocity, the velocity magnitude and horizontal and vertical component of velocity, respectively.

We ought to emphasize at this point that, as mentioned above, the contributions to the particle dynamics originating independently from the two postulated flow fields of He II are at present difficult to separate, as the used deuterium particles, which are not tracers (i. e., fluid particles), generally interact simultaneously with both velocity fields and their motions are additionally influenced by *quantized vortices*, which interact with each other and therefore with both mentioned continuous velocity fields.

In figure 4.3, maps of the $\vartheta(\vec{r}, \phi)$ are shown, at temperature $T = 1.24$ K, obstacle motion frequency $f = 0.5$ Hz, and amplitude $A = 5$ mm, for various phases (ϕ) of the motion. The macroscopic vortices form in the wake, as visible in the figure at phases $\phi = 90^\circ$ and 270° , respectively. The vortex is a stable structure, therefore it stays there even if the obstacle moves back (phases 135° , 180° , 315° and 0° respectively) and they are pushed by the obstacle, later along the sides into the wake (phase 45°), where they are neutralized by a new pair of forming vortices of opposite spin.

Figures 4.4 and 4.5 show, in the form of the pseudovorticity ϑ maps, the

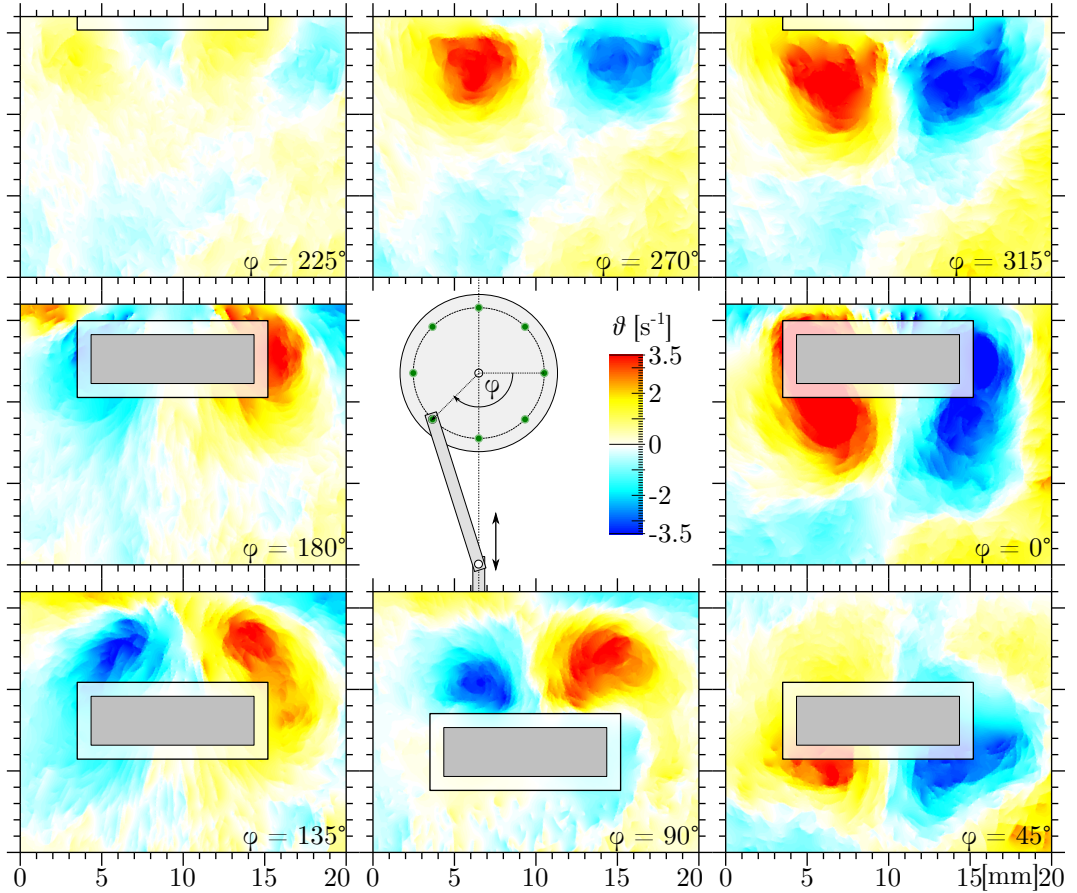


Figure 4.3: PTV-based pseudovorticity ϑ at different phases of the motion in He II at temperature 1.24 K, frequency 0.5 Hz and amplitude 5 mm. The rectangles represent the actual size of the obstacle and the mask size, respectively. The physical dimension of each panel is 20×16 mm, one unit on both axes corresponds to 1 mm; the axis labels are not displayed in order to save place. Note also that the motion is not strictly harmonic, see figure 2.5 in section 2.4.

macroscopic vortices shed at the bottom position of the obstacle in He II at different frequencies and both available amplitudes. In all cases the vortices are evident, but the quality is strongly affected by the insufficient camera frame rate (which was 100 Hz) at the larger velocities, because the flow is quite fast in the wake. Then the trajectory connection did not work well and therefore there are no velocity data in the wake, which causes that the vortices appear to be weaker than they really are and become shifted away from their real position. This problem would be fixed simply by increasing the camera frame-rate, which is, unfortunately, impossible to do *after* the experiment. On the other hand, at lower velocities, the flow is disturbed by the residual flow produced by the particle stirring. This is even more evident in He I as shown in figure 4.6. This problem is not so easy to fix, as longer waiting times would imply lower amount of particles.

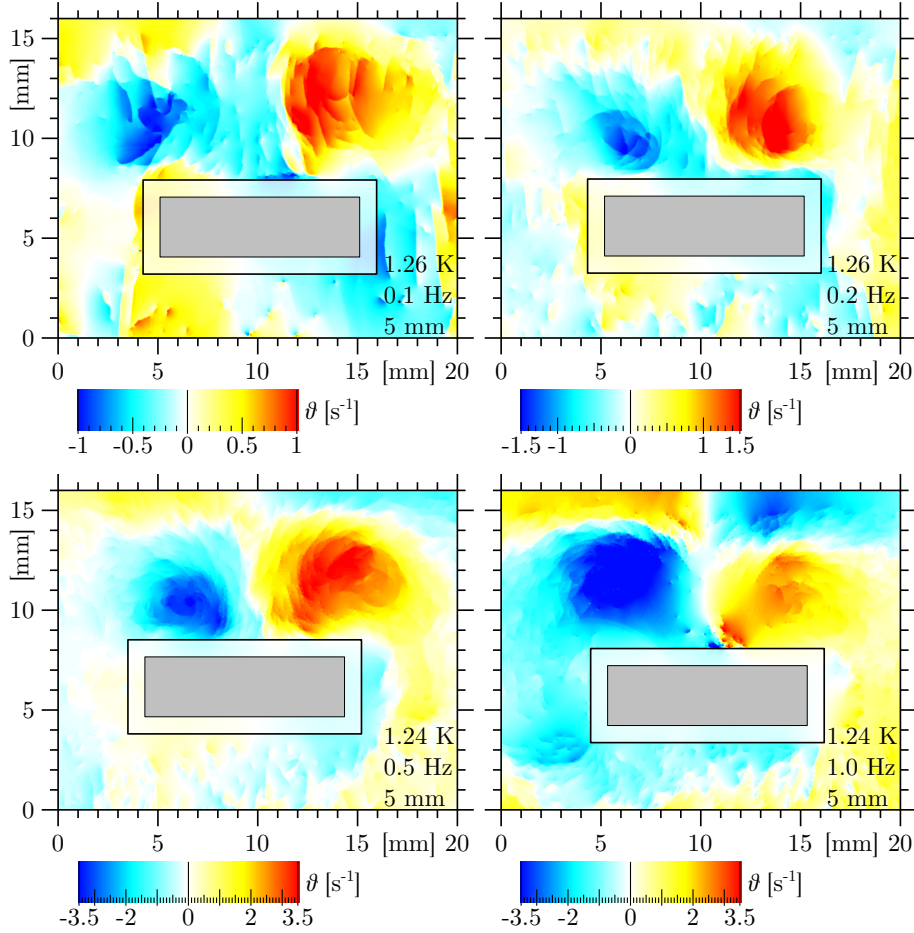


Figure 4.4: PTV-based pseudovorticity ϑ in He II, amplitude 5 mm and different frequencies: 0.1 Hz, 0.2 Hz, 0.5 Hz and 1.0 Hz, respectively. All panels show the situation near the bottom dead center of the obstacle motion. The rectangles represent the actual size of the obstacle and the mask size. The lower strength of vortices in the right bottom panel is caused artificially by the lack of quality trajectories as the particles moved too fast in the wake, hence the trajectory connection failed there. That the location of the obstacle is not stable is caused by the mechanical imperfection of the moving mechanism.

4.3 Macroscopic vortices

4.3.1 Vortex model

The observed macroscopic vortices in He II are very similar to those known from the flow of classical liquids, and, as already said, they are similar to those observed in He I in this experiment. In order to quantify this similarity we can examine their structure.

The simplest model of a real vortex in a classical fluid is the so called *Rankine vortex*¹, which connects the two limiting cases – the *rotation like a solid body* and the *potential rotation* – in such a way that the tangential component of the fluid

¹William John Macquorn Rankine, 1820 – 1872, Scottish.

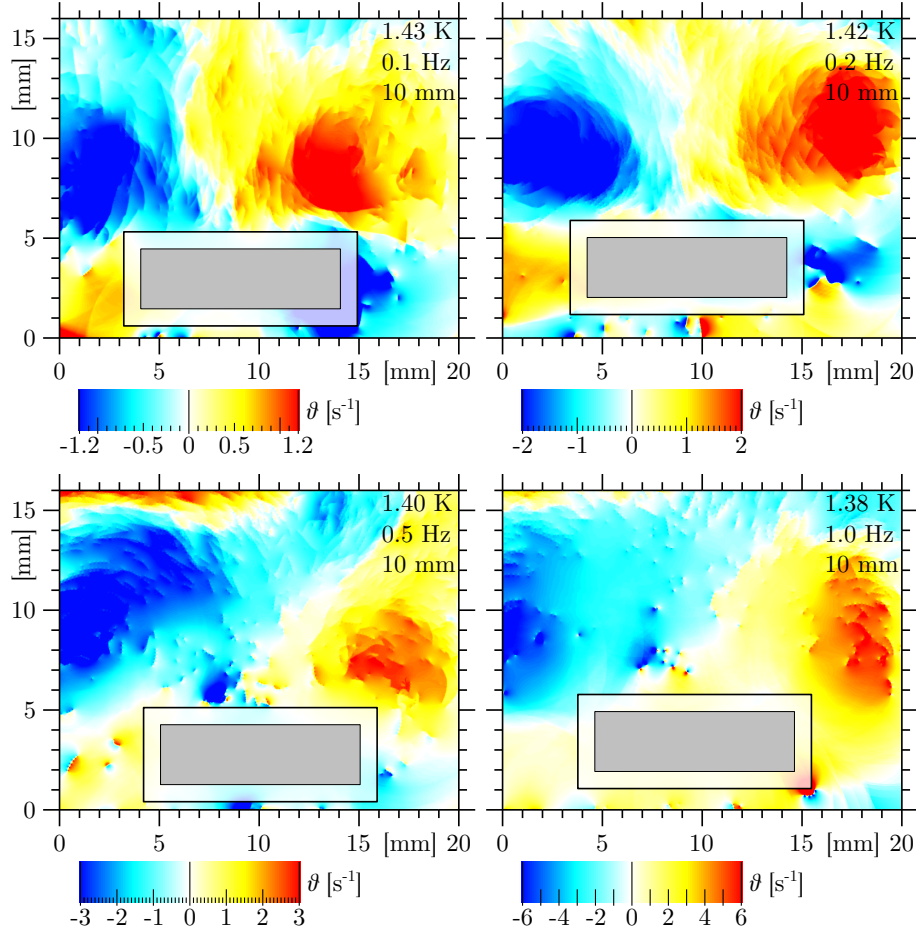


Figure 4.5: PTV-based pseudovorticity ϑ in He II, amplitude 10 mm and different frequencies: 0.1 Hz, 0.2 Hz, 0.5 Hz and 1.0 Hz, respectively. All panels show the situation near the bottom dead center of the obstacle motion. The lower strength of vortices in both bottom panels and even the worse resolution at the largest frequency is caused artificially, by the lack of long trajectories as the trajectory connection did failed in such areas due to the too fast motion of particles in the wake.

velocity u in the distance r from the center of the vortex is

$$u(r) = \begin{cases} \frac{\Gamma_0}{2\pi} \frac{r}{R_C^2} & \text{for } r < R_C \\ \frac{\Gamma_0}{2\pi} \frac{1}{r} & \text{for } r > R_C, \end{cases} \quad (4.1)$$

where R_C is the vortex core radius² and Γ_0 is the *circulation* of this vortex which represents the vortex strength. The inner part of the vortex (i. e. for $r < R_C$) is called the *vortex core* and it rotates like a solid body, while the outer part (i. e. for $r > R_C$) represents an *inviscid potential vortex*.

A more sophisticated model containing turbulence inside the core was introduced by Amromin [97], who derived it from the Navier-Stokes equations for a classical viscous fluid with small kinematic viscosity ν . The tangential component u of the fluid velocity at the distance r from the vortex center has a following

²Not to be misunderstood with the quantized vortex core, which has the diameter in order of $1 \cdot 10^{-10}$ m.

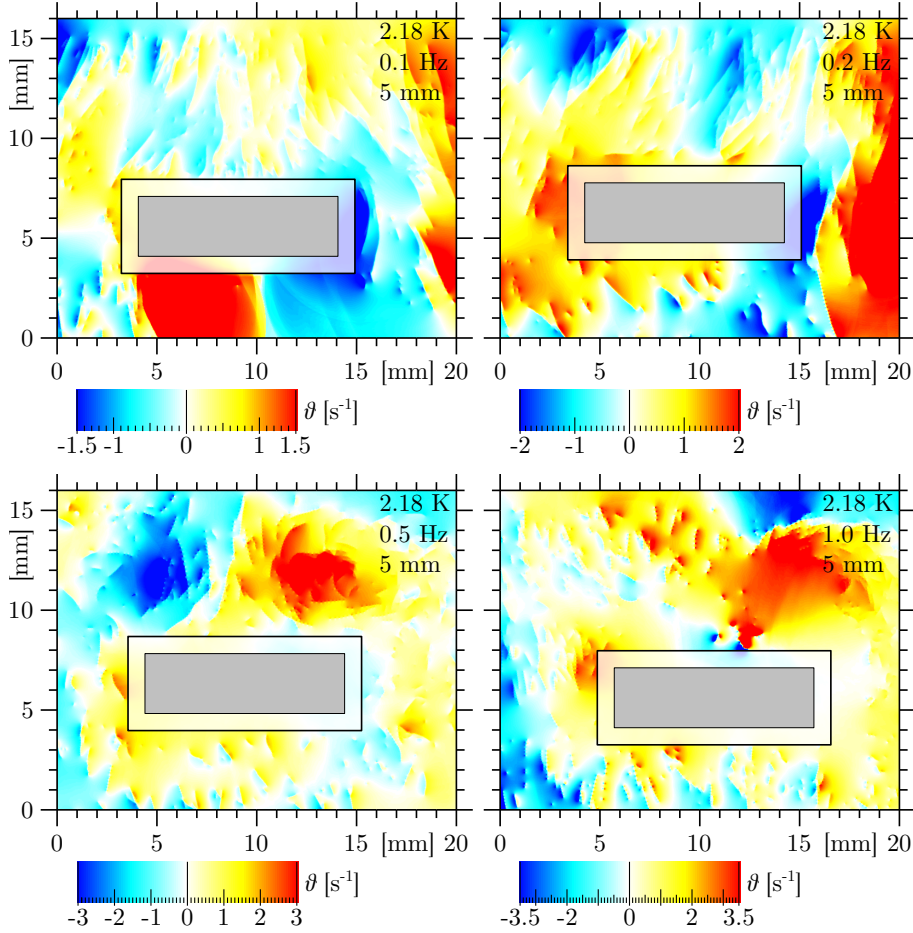


Figure 4.6: PTV-based pseudovorticity ϑ in He I, amplitude 5 mm and different frequencies: 0.1 Hz, 0.2 Hz, 0.5 Hz and 1.0 Hz, respectively. All panels show the situation near the bottom dead center of the obstacle motion.

form:

$$u(r) = \begin{cases} \frac{\Gamma_0}{2\pi} \frac{r}{R_C^2} + \frac{\langle v'_x v'_y \rangle r}{2\nu} \ln \frac{r}{R_C} & \text{for } r < R_C \\ \frac{\Gamma_0}{2\pi} \frac{1}{r} & \text{for } r > R_C, \end{cases} \quad (4.2)$$

where Γ_0 and R_C are, similarly to the previous case 4.1, constants representing respectively the *circulation* of the vortex and a vortex core radius. $\langle v'_x v'_y \rangle$ is the *turbulent stress term*, which is very difficult to measure experimentally, but, fortunately, it can be eliminated from the equation 4.2 by applying the condition of continuity at $r = R_C$, leading to

$$u(r) = \begin{cases} \frac{\Gamma_0}{2\pi} \frac{r}{R_C^2} \left(1 - \ln \frac{r}{R_C}\right) & \text{for } r < R_C \\ \frac{\Gamma_0}{2\pi} \frac{1}{r} & \text{for } r > R_C. \end{cases} \quad (4.3)$$

The inner part of this model vortex (i. e. for $r < R_C$) is called *turbulent vortex core* while the outer part (i. e. for $r > R_C$) represents an *inviscid vortex*. This modification to the *Rankin model* affects mainly the profile near the vortex center. There are additional enhancements available, affecting mainly the crossover between the core and the inviscid envelope based on the assumption of vortic-

ity diffusion, for more details see [98] or the so called *Burger's vortex* (in the Amromin's model, the transition is continuous but not smooth).

4.3.2 Vortex circulation profiles

In a pure superfluid, the macroscopic rotation can be realized only via at least partial polarization of the vortex tangle, which allows the superfluid to *mimic* the macroscopic flow of classical viscous liquid. This scenario is suggested by various numerical models, including those studied in our group, see, e. g., Varga [26].

The similarity of the observed macroscopic vortices in He II with those in classical fluids can be illustrated by the Amromin's theory applied to them; we do so by comparing the theoretical dependence expressed by formula 4.3 with measured circulation profiles, see figure 4.7. Again, it is important to remind that we are observing the motion of *particles*, not a motion of *normal* or *superfluid* component.

Because the value of the tangential component of velocity u near the the vortex center is heavily influenced by noise, we decided to analyze the behavior of $ur = |\vec{v} \times \vec{r}|$ instead of u itself. We see that ur converges better for small r but it does not behave as expected for larger r (i. e. it is not constant, as the theory predicts), which is probably caused by the increasing influence of the second oppositely oriented vortex and possibly by other flow structures further away.

The estimation of $\Gamma/(2\pi)$ as a function of r was done in a following way: we have determined the center of the vortex manually, then for each point of each trajectory longer than 5 points we calculated the vector product $\vec{v} \times \vec{r}$, where \vec{v} is the actual velocity of the trajectory point determined by using the previous and the next positions, and \vec{r} is the position vector with respect to the center of the vortex. We have sorted out these products according to the magnitude of \vec{r} into the sets representing the annuli and calculated the average and standard deviation in each annulus thus obtaining the radial dependence of the macroscopic vortex circulation (we call it *profile*). A non-trivial observation is that such profiles do not depend on temperature, therefore we venture to merge the data obtained at different temperatures in order to get a better statistics.

The circulation profiles of the observed macroscopic vortices formed behind the obstacle near its bottom position are shown in figures 4.7 and 4.8. The corresponding error bars are determined by a standard way as $\sigma = \sqrt{\sigma_\Gamma^2 + \mu_\sigma^2}$, where σ_Γ is the standard deviation of the averaged values, while μ_σ is the average of standard deviations of the partial profile points. It seems that this leads to overestimation of the error bars, but, on the other hand, the partial profiles before averaging are significantly scattered, sometimes up to a degree that in some data sets their systematic structure is impossible to determine.

The equation 4.3 for the circulation can be rewritten in a dimensionless form

$$\Gamma'(r') = r'^2 (1 - \ln r'), \quad (4.4)$$

where $r' = r/R_C$ and $\Gamma' = \Gamma(r)/\Gamma_0 = [2\pi(ur)(r)]/\Gamma_0$. The values of $\Gamma_0/(2\pi)$ and R_C for different oscillation frequencies and amplitudes in He II are given in table 4.1. During the fitting procedure, more weight has been given to the data closer to the center. We have got less statistics in He I, hence the fitting does not converge here so nicely and for this reason it is not displayed graphically.

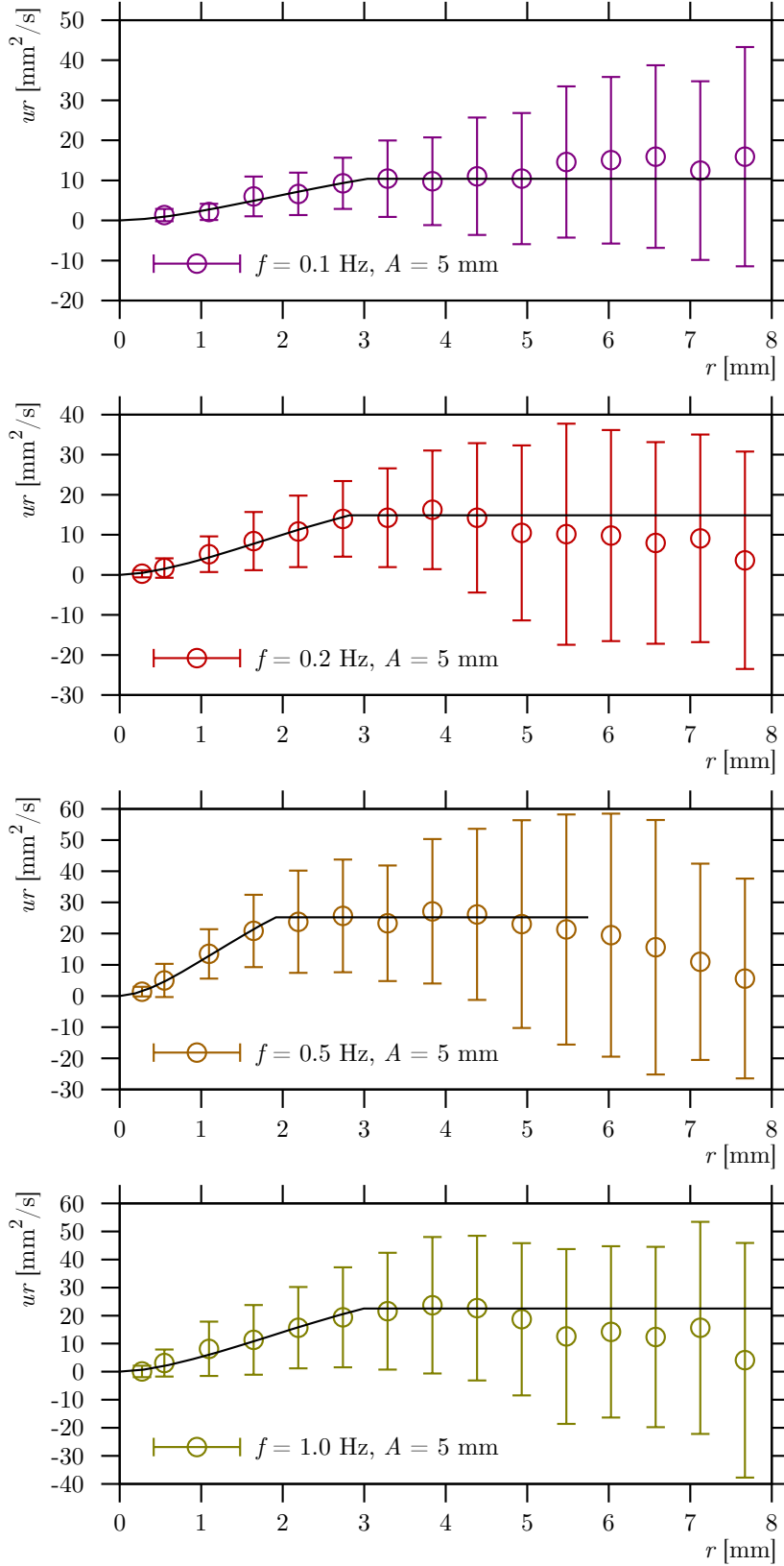


Figure 4.7: Circulation profiles, i. e. the dependence of $ur(r) = 1/(2\pi)\Gamma(r)$ on the distance from the vortex center, at the bottom position of the obstacle. Amplitude A and frequency f of the obstacle are indicated in each panel. The circles represent the data obtained at different temperatures in He II, averaged and weighted by the number of used trajectory points as described in the text.

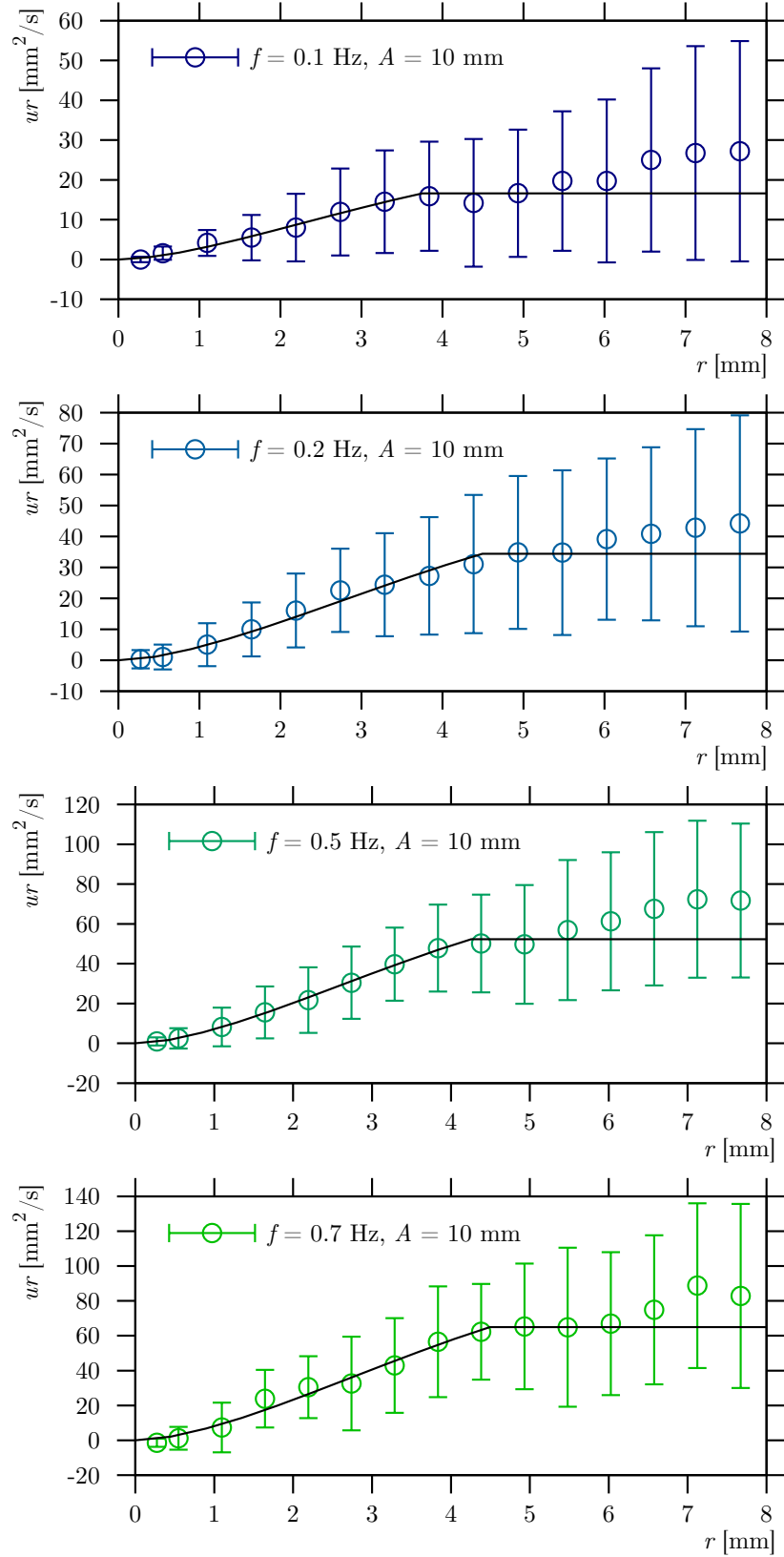


Figure 4.8: Circulation profiles at the bottom position of the obstacle. Amplitude A and frequency f of the obstacle are indicated in each panel. The circles represent the data obtained at different temperatures in He II, averaged and weighted by the number of used trajectory points as described in the text.

Table 4.1: Summary of the fits of observed macroscopic vortices by the Amromin vortex model, equation 4.3. First two columns specify the parameters of the data set averaged over entire temperature range in He II. R_C is the radius of turbulent vortex core, while $\Gamma_0/(2\pi) = (ur)_0$ represents the strength of the vortex, Γ_0 being its circulation. Displayed uncertainties of these values are only the uncertainties of the fit of the averaged points, the scatter of these points (error bars in figures 4.7 and 4.8) is not included. N_p stands for the total number of used trajectory points after filtering (in this case depending only on the length of the trajectory, as described in the text).

frequency [Hz]	amplitude [mm]	R_C [mm]	$\frac{1}{2\pi}\Gamma_0$ [mm ² /s]	N_p
0.05	5	2.23 ± 0.23	6.6 ± 2.6	16512
0.1	5	3.04 ± 0.16	10.4 ± 2.1	7243
0.2	5	2.82 ± 0.12	14.9 ± 2.2	14965
0.5	5	1.92 ± 0.09	25.2 ± 4.4	9316
0.7	5	3.40 ± 0.42	36.3 ± 15.0	1454
1.0	5	2.99 ± 0.13	22.5 ± 3.5	12625
0.05	10	5.58 ± 2.84	13.8 ± 19.9	12158
0.1	10	3.75 ± 0.24	16.6 ± 3.9	16467
0.2	10	4.49 ± 0.18	34.4 ± 4.6	15510
0.5	10	4.26 ± 0.12	52.3 ± 5.4	10167
0.7	10	4.49 ± 0.17	64.9 ± 8.7	2394

4.4 Behavior of $\langle \vartheta^2 \rangle$

In order to quantify how the magnitude of the shed vortices depends on the experimental conditions, which are temperature T , frequency f , and amplitude A , for each processed movie we compute the quantity $\langle \vartheta^2 \rangle$, i. e., the ensemble average of ϑ^2 – it can be loosely interpreted as the square of the average flow vorticity ω . The reason for doing so is that the positive quantity $\langle \vartheta^2 \rangle$ retains useful quantitative information allowing the comparison of the visualized flow fields. The second power has naturally two advantages: first, clockwise and anti-clockwise rotations sum up, not subtract, second, the areas with faster rotation count more, therefore the importance of the rest of the flow field of view diminishes.

It is still true, however, that the areal average of this quantity on itself has no sense, it has to be used in comparison with the data obtained in the same experiment. In addition, the resulting $\langle \vartheta^2 \rangle$ depends not only on the experimental parameters like bath temperature, obstacle shape, size, frequency and amplitude, the density of particle seeding or the size of the field of view, but also on parameters used in the calculation: the phase window width Φ , radius of integration area R_m and, additionally, on the grid density that is used in any particular calculation. The dependence on the calculation grid density for number of grid points greater than $1 \cdot 10^3$ is however negligible, which is always fulfilled, as the used grid resolution is $800 \times 600 \approx 5 \cdot 10^5$. The dependence on the phase window Φ is linearly decreasing with increasing Φ as with increasing time distance the velocity correlation decreases. The chosen value $\Phi = 15^\circ$ is a compromise between the time-locality and the statistical convergence. The dependence on R_m

is decreasing with increasing R_m , see discussion 4.5.

While in the range of investigated parameters we do not observe any clear temperature dependence of $\langle \vartheta^2 \rangle$, it increases with the oscillation frequency. In other words, it is not surprising that, as the motion strength increases, the magnitude of the shed vortices also increases.

4.4.1 Dependence on Reynolds number

As it is customary in fluid dynamics, we show our results on the vortex strength as a function of relevant Reynolds numbers Re , although we do not observe any strong oscillation amplitude dependence of the data. In the case of He I, we chose the (viscous) Reynolds number as

$$Re = \frac{\Omega A s}{\nu}, \quad (4.5)$$

where $\Omega = 2\pi f$ and A are, respectively, the oscillation angular velocity and amplitude, s is the characteristic size of the obstacle which we have chosen $s = 10$ mm, i. e., equal to the obstacle width that pushes the fluid, and ν stands for the effective bulk kinematic viscosity – its values are taken from [5]. Another definition of ν we employ here to characterize the obtained He II data follows the work by L’vov et al. [69], where the kinematic viscosity of He I at the lambda line was found to be $\nu = \kappa/6 = 1.66 \cdot 10^{-8}$ m²/s and is assumed constant below it. We therefore use this value for computing the (superfluid) Reynolds number Re_κ .

The corresponding Re_κ range for our data (figure 4.10) lies approximately between 800 and 37000 and the viscous penetration depth $\delta = \sqrt{\kappa/3\Omega}$ range is between about 0.25 mm, at the smallest Re_κ , and 0.05 mm, being therefore always larger than our typical particle size (smaller than 0.01 mm). Although it is larger than our pixel resolution 0.03 mm, the boundary layer is not resolved due to overlighting of the area close to the obstacle, which forced us to mask the raw images by using a mask somewhat greater than the boundary layer area, see figures above, where the masked area is highlighted.

For our He II data, the first (viscous-like) definition of Reynolds number leads to $900 < Re < 83000$ in the considered experimental conditions, which corresponds to $\delta = \sqrt{2\nu/\Omega}$ ranging between approximately 0.23 and 0.04 mm, respectively, see figure 4.9.

Qualitatively similar figures 4.9 and 4.10 display the overall mean of ϑ^2 as a function of the just introduced Reynolds numbers. The standard deviation of the displayed points is up to $8\times$ larger than the value, which is caused simply by different strength of ϑ in different areas and phases; still, the data scatter cannot be neglected here. The He II data points shown in both figures 4.9 and 4.10 collapse to an increasing curve of both Reynolds numbers, $Re = \Omega A s/\nu$ as well as $Re_\kappa = 6\Omega A s/\kappa$. Similarly, despite the larger scatter, the He I data points also display the tendency to collapse, but to *another* curve. The tendency to collapse is slightly stronger for data points calculated from movies with larger number of trajectory points (see the caption of figures 4.9 and 4.10). The existence of these two separate curves is a puzzling outcome.

Let us spell it even more clearly. The parameter $\langle \vartheta^2 \rangle$ as displayed in figures 4.9 and 4.10 appears to behave differently in He I and He II, as a function of the

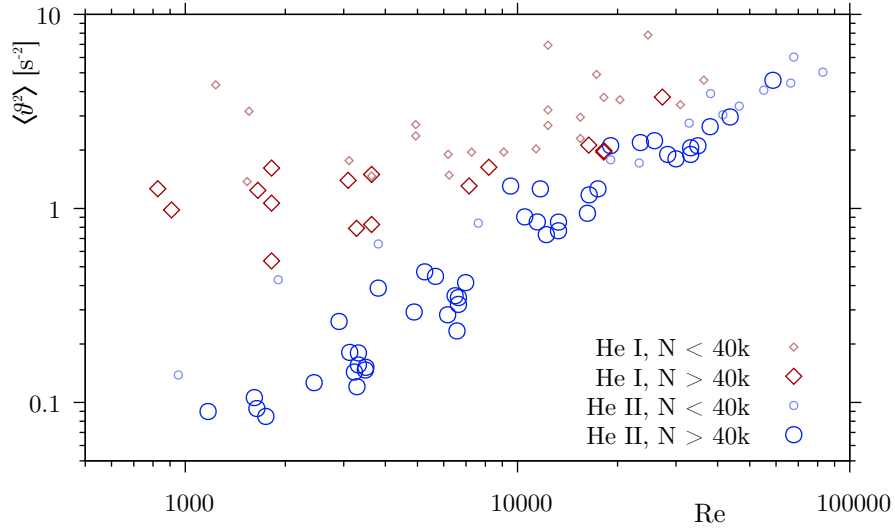


Figure 4.9: Plot of the dependence of $\langle v^2 \rangle$ on Reynolds number Re , which is in the case of He II (blue circles) based on the measured effective bulk viscosity tabulated in [5]. Small symbols represent such datasets with less than 40 000 trajectory points (after filtering), while the bigger symbols represent those with more than 40 000 points. Red squares are the data obtained in He I, the corresponding definition of Re is straightforward.

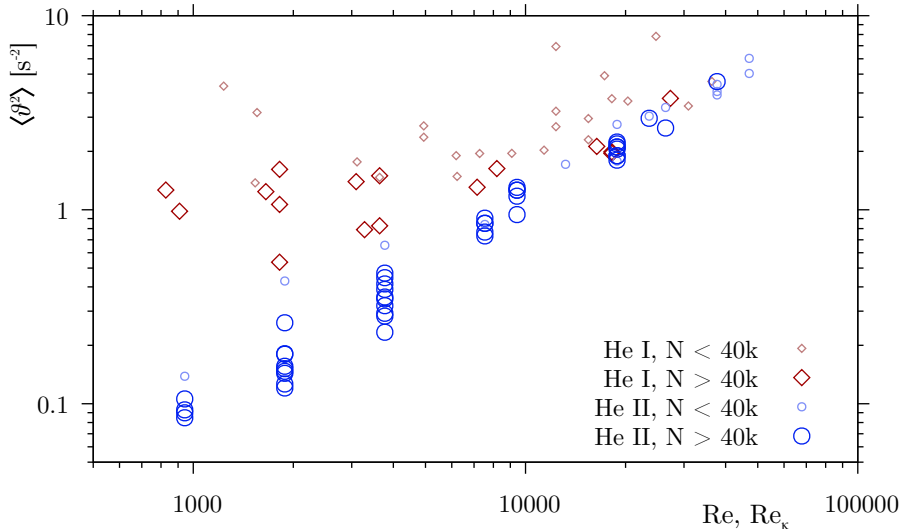


Figure 4.10: Plot of the dependence of $\langle v^2 \rangle$ on Reynolds number Re , which is in the case of He II (blue circles) based on the estimation of $\nu = \kappa/6$, see [69]. Small symbols represent such datasets with less than 40 000 trajectory points (after filtering), while the bigger symbols represent those with more than 40 000 points. He I data (red squares) are the same as in the previous figure 4.9.

Reynolds number. This is on the first sight in contrast with the common assumption that forced coflows of He II at large enough length scales are closely similar to viscous flows of comparable magnitude, as discussed, e. g., by Chagovets, Xu and Van Sciver [99], [93]. The existence of two distinct branches, at Reynolds numbers smaller than approximately 10^4 , but not above this value, although influenced by the relatively large data scatter, calls therefore for plausible physical explanations, not related to the used data processing procedure.

One of the relevant differences between He I and He II is the fact that the heat conductivity of He II is about $10^6 \times$ larger than that of He I, see [5], i. e., the heat dissipates in He II much faster than in He I. If we take into account that the helium gas injected into the cryostat in order to stir the sedimented particles (see section 2.7) is *very hot* compared with the bath, then the incoming heat has to dissipate, which may result in parasitic flows that might partly mask the macroscopic vortices shed at the cylinder edges, especially at the lowest frequencies and in He I. This is a contra-intuitive statement as one would expect that the residual flows created by the gas injection would dissipate *faster* in He I due to its larger viscosity, but we believe that the amount of injected heat dominates the injected kinetic energy. In other words, the observed residual flows behave more like a thermal convection. This explanation could be tested simply by repeating the experiment with different waiting times after the injection.

4.4.2 Length scales

Another reason that might contribute to explain the two obtained curves at low Reynolds numbers is related to the different ratio of probed length-scales to those characteristic for the flow. The probed length scale d can be viewed, both in He I and He II, as the average distance traveled by a particle between two consecutive frames. If we, for the sake of simplicity, assume that the average particle velocity is of the order of the imposed cylinder velocity, we find that d can be estimated as $d \approx \Omega A / f_{\text{cam}}$ ($f_{\text{cam}} = 100$ Hz is the camera frame-rate).

On the other hand, we have to consider the small length scales characterizing the flow: the *intervortex distance* ℓ (to be discussed below) in the case of He II, and the *Kolmogorov length-scale* η in the case of He I:

$$\eta \approx \sqrt[4]{\frac{\nu^3}{\varepsilon}}. \quad (4.6)$$

Here $\varepsilon = -dE/dt$ is the *energy decay rate* and, if we assume that the average vorticity $\omega^2 \approx \langle \vartheta^2 \rangle$, we can use the classical relation linking ε with the flow average vorticity ω :

$$\varepsilon = \omega^2 \nu \quad (4.7)$$

getting

$$\eta \approx \sqrt[4]{\frac{\nu^3}{\varepsilon}} \approx \sqrt[4]{\frac{\nu^2}{\langle \vartheta^2 \rangle}}. \quad (4.8)$$

In the case of He II, we write the average vorticity ω due to the flow of He II with *vortex line density* L as

$$\omega \approx \kappa L = \frac{\kappa}{\ell^2}, \quad (4.9)$$

which is based on the assumption that the energy decay rate ε of the flow is proportional to the square of the quantized vortex length L per unit volume, also known as the vortex line density. It follows that

$$\varepsilon = \nu_{\text{eff}} (\kappa L)^2. \quad (4.10)$$

Although equation 4.10 lacks a rigorous theoretical justification, being mainly motivated by the analogy with the classical relation 4.7, it has been successfully used to describe various He II flows. For example, as recently discussed by Varga and coworkers [100], mechanically generated flows of He II can, on large enough scales, be viewed as flows of a single-component fluid possessing an effective kinematic viscosity, which one can deduce from either temporal decay [101] or even from the steady-state data [102].

Therefore, by using equations 4.7, 4.9 and 4.10, we get the mean intervortex distance ℓ :

$$\ell_q \approx \sqrt[4]{\frac{\kappa^2}{\langle \vartheta^2 \rangle}}. \quad (4.11)$$

This is closely similar to the classical relation 4.8, except for the factor $\sqrt{6} \approx 2.4$. This analogy can be pushed further, by setting

$$\ell_c \approx \sqrt[4]{\frac{\nu_{\text{eff}}^2}{\langle \vartheta^2 \rangle}}, \quad (4.12)$$

where ν_{eff} can be understood as an effective bulk kinematic viscosity, e. g., as that published in [5] or as theoretically estimated value $\kappa/6$ in [69] and assume that its temperature dependence over our range of investigated temperatures is weak.

We can now define the ratio R between the probed length-scale d and the flow characteristic length-scale:

$$R = \begin{cases} d/\eta & \text{for He I} \\ d/\ell & \text{for He II.} \end{cases} \quad (4.13)$$

The resulting ratio R is plotted as a function of Re and, respectively, Re_κ , in figure 4.11. It is apparent that we are actually probing length scales larger than the relevant flow scale only at Reynolds numbers larger than about 10^4 . In other words, the two branches displayed in figures 4.9 and 4.10 might possibly exist due to the fact, that, at Reynolds numbers smaller than 10^4 , we are investigating scales smaller than the dissipative flow scale in He I or the intervortex distance in He II. While in He I below the Kolmogorov length-scale the fluid motion is dissipated into heat by the action of the finite viscosity, quantum flows of He II may exist all the way down to the scale – the size of the cores of quantized vortices. We may say that quantum restrictions on the superfluid motion could be the reason why, for Reynolds numbers smaller than 10^4 , the parameter $\langle \vartheta^2 \rangle$ behaves differently in He I and He II.

4.4.3 The quantum signature

The importance of the length-scale ratio R is additionally illustrated by figure 4.12, which shows the normalized distribution of horizontal velocity component

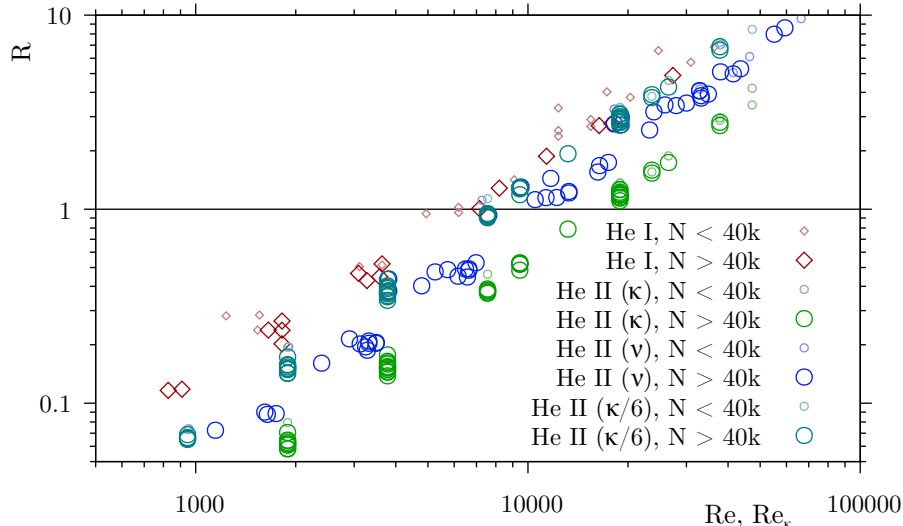


Figure 4.11: Plot of the dependence of the ratio R on Reynolds number. Red squares represent He I data, where Re and η are calculated according to classical approach, equation 4.8, green circles correspond to He II data with ℓ_q calculated according to equation 4.11 against Re_κ . Blue circles denote He II data, where the estimation of Re and ℓ_c (equation 4.12) is based on the experimentally measured effective kinematic viscosity, see [5], while the cyan circles are the same He II data, but Re_κ and ℓ_c are calculated by using the approximation $\nu = \kappa/6$, see [69]. Small symbols represent such datasets with less than 40 000 trajectory points (after filtering), while the bigger symbols represent those with more than 40 000 points.

for selected movies having different R both in He I and in He II. We can easily notice that all distributions with $R > 1$ are more or less of a Gaussian shape³, while those with $R < 1$ and in He II are wider, having tails comparable with the v^{-3} shape observed in the *thermal counterflow* experiment, see our publication [64] and the author’s diploma thesis [22]. This length-scale dependence is studied in more detail in the article [54] and in the chapter 7 of this Thesis.

To summarize, we have identified and discussed three possible reasons why the parameter $\langle v^2 \rangle$ at low Reynolds numbers behaves differently in He I and He II: first, the data scatter, second, different heat conductivities of He I and He II, and, third, the fact that the probed length-scales are smaller than the Kolmogorov scale in He I or the quantum length scale in He II, respectively.

4.5 Discussion

Neither table 4.1 nor figure 4.8 display results for $f = 1.0$ Hz and $A = 10$ mm, despite measurements were performed under these conditions. Similarly, the data quality in figures 4.4 and 4.5 in panels for higher velocities is very poor. The reason is that the camera frame-rate was not sufficiently fast for a such rapid flow, especially in the back-flow in the wake behind the obstacle, and therefore connecting of trajectories does not work well. The velocity in the back-flow in the wake is approximately twice the obstacle velocity, i. e. $v_{\max} \sim 2A\Omega \approx 125$ mm/s,

³Intermittent effects cannot be observable with our statistics.

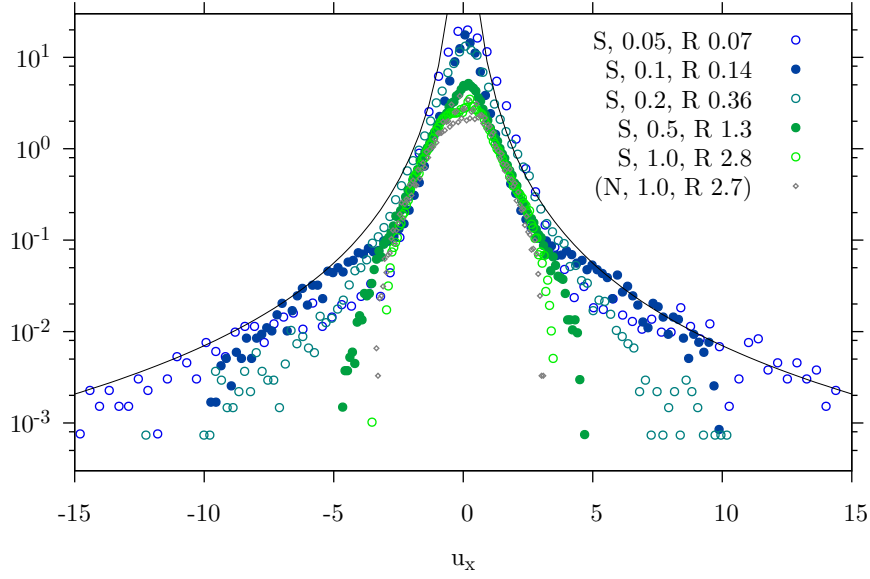


Figure 4.12: The *Probability density function*, PDF in percent, of the normalized horizontal velocity $u_x = \frac{v_x - \langle v_x \rangle}{\sigma[v_x]}$ of selected datasets with amplitude $A = 5$ mm and different frequencies (the first number in the legend) in He II corresponding to different ratios R , see equation 4.13, of the probed length-scale and the flow small length-scale; current R is the second number in the legend. Thin black line represents the distribution u_x^{-3} characteristic for particles trapped on a quantized vortex orbiting around another straight vortex. An example of He I data is shown in gray, see figure 4.13 for more of them.

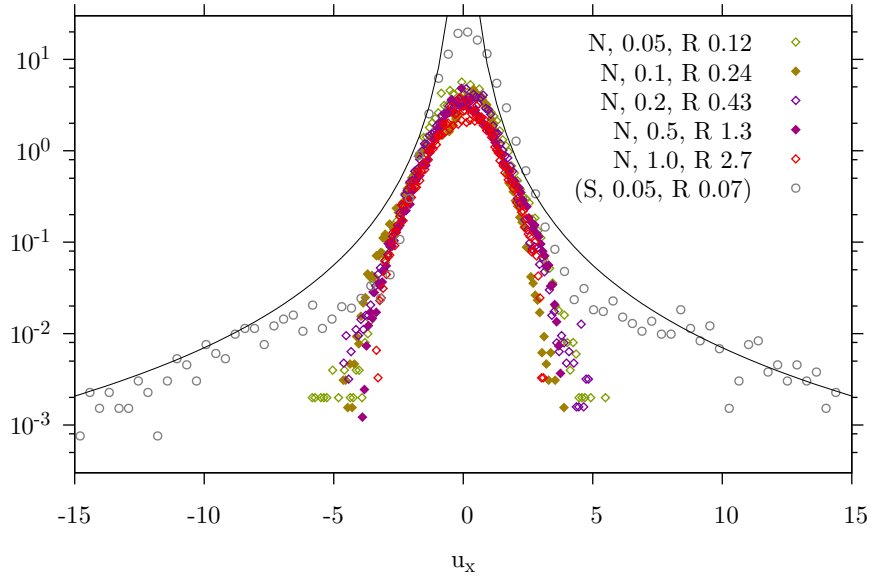


Figure 4.13: The PDF of the normalized horizontal velocity $u_x = \frac{v_x - \langle v_x \rangle}{\sigma[v_x]}$ of selected datasets with amplitude $A = 5$ mm and different frequencies (the first number in the legend) in He I corresponding to different ratios R ; current R is the second number in the legend. An example of He II data is shown in gray, see figure 4.12 for more of them.

which, at our resolution $27.4 \mu\text{m}/\text{pix}$ and camera frame rate 100 Hz, corresponds to about 45 pix/fr. This fact strongly suggests that, if this experiment is repeated, higher camera frame-rate has to be used. Second possibility is to decrease the number of particles, but then we would need longer movies to obtain comparable statistics, which in the presented case is rather poor. This is always a problem – better setup ideas come to mind *after* the analysis is done.

4.5.1 Choice of integration area radius

The calculation of the the PTV-based pseudovorticity ϑ is strongly dependent on the choice of the integration area size, R_m . As it was already discussed in section 2.10, ϑ converges to the proper vorticity ω of a single continuous flow field, if the size of integration area converges to zero, if the tracking particles are fluid particles and if the density of seeding is infinite. None of this conditions is fulfilled in our real experiment, but we can, at least, try to optimize the plausibility and validity of our results by optimizing the size of the integration area creating a balance between the statistical quality and the locality. Figure 4.14 shows values of ϑ^2 and examples of its spatial distribution for different values of the parameter R_m .

With larger R_m , there are more terms with larger distance from the probed point, hence of smaller magnitude, which results to systematically smaller ϑ^2 , see figure 5.12 panel A. Figure 5.12 panel B shows the dependence of $\vartheta^2 R_m^2$ on R_m and we can easily recognize there various regimes of ϑ scaling: first, if the number of trajectory points inside the integration area is in order of ones, then the resulting ϑ is more or less a random number depending on the exact relative positions of the probed point \vec{r} and the trajectory point \vec{r}_i , then ϑ scales as R_m^{-2} , hence $\vartheta^2 R_m^2$ as R_m^{-2} too⁴. If we imagine calculation of ϑ in an area with uniformly rotating trajectories, we get ϑ scales as R_m^{-1} , hence $\vartheta^2 R_m^2$ scales as $R_m^0 = 1$, panel D. The drop of $\vartheta^2 R_m^2$ at $R_m \sim 2 - 4$ mm is probably caused by covering less correlated more distant areas inside the integration area. At larger R_m the influence of the edge of the field of view increases, the edge produces a fake signal due to the lack of data outside producing a *virtual* shear, and hence $\vartheta^2 R_m^2$ slightly grows with R_m . If R_m is larger than the field of view, ϑ is no more affected by its value and $\vartheta^2 R_m^2$ scales as R_m^2 (the last two points in the plot).

Finally, $R_m = 5.0$ mm has been chosen, which corresponds to the half of the width of the obstacle, therefore we can expect similar size of the produced vortical structures; additionally, there is a minimum in the plot of $\vartheta^2 R_m^2 (R_m)$ at this value of R_m . This choice is consistent with the choice of R_m in the study of *viscous streaming*, chapter 5, in the sense that the more important side is that pushing the fluid. One can of course argue that we cheat a bit when selecting the size of vortices we would like to see, but the existence of vortices of such a size is visible, perhaps less clearly (in some cases they are partly covered by a kind of „ghosts“ appearing statistically in the data) also for different choices of R_m .

⁴By the way, there are 148 856 trajectory points in the example dataset, 12 404 inside the used phase window, which leads to mean interparticle distance 0.2 mm, hence the average number of trajectory points used to calculate one ϑ -point is 23 at the smallest shown $R_m = 0.5$ mm (panel C) in this dataset.

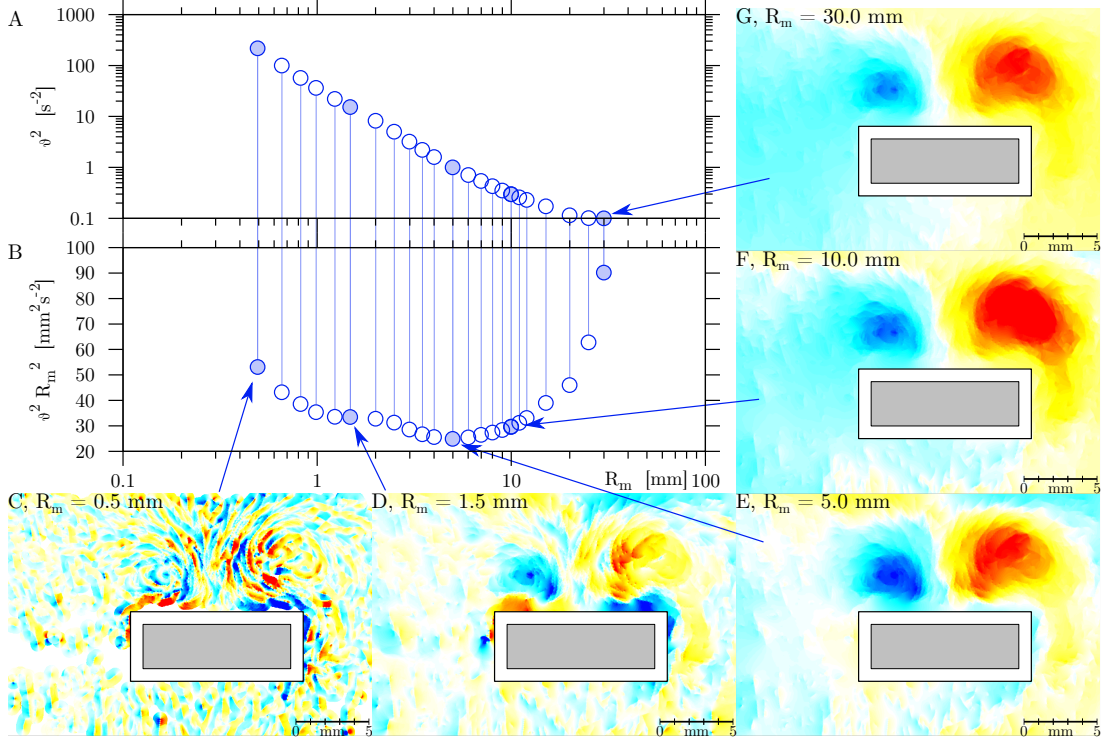


Figure 4.14: The panel **A** shows the dependence of overall square of ϑ as the function of R_m for the data taken in He II at obstacle frequency 0.5 Hz and amplitude 5 mm near its bottom position. Panel **B** shows the same values multiplied by R_m^2 to neutralize the scaling caused statistically. Other panels, **C** – **G**, show examples of the spatial distribution of the pseudovorticity ϑ at different values of R_m . As the final value of R_m has been chosen $R_m = 5.0$ mm, which corresponds to the half of the width of the obstacle (the side, which pushes the fluid), therefore we can estimate similar size of the produced vortical structures.

4.6 Conclusion of the chapter

The behavior of macroscopic, millimeter-sized vortical structures, generated by a body of rectangular shape oscillating in liquid ^4He , has been studied by visualizing the dynamics of micrometer-sized particles seeding the fluid. An obstacle of rectangular cross section (3×10 mm) performed quasiharmonic oscillations in the liquid, at various frequencies (0.05 – 1.25 Hz) and amplitudes (5 and 10 mm), at temperatures between about 1.2 and 3 K, resulting in Reynolds numbers up to 10^5 . Consequently, in the present experiments, a direct comparison between similar, mechanically driven flows of He I and He II was carried out. First of all, our visualization study confirms the existence of large vortical structures shed by the oscillating body, which appear similar in viscous He I and superfluid He II. Although this result is not surprising (for example, visualization of macroscopic vortex rings was reported in [103] and in [104]), our investigation represents, to the best of our knowledge, the first systematic visualization study of quantum flows due to an oscillating object. We note, additionally, that in viscous fluids vortices are shed by accelerating plates at similar Re as the minimum Reynolds numbers investigated here, as reported by Taneda and Honji [86].

At Reynolds numbers lower than approximately 10^4 , a noticeable difference

between the investigated He I and He II flows is observed. More precisely, after thorough studies of the quality of the data sets and of the robustness of the processing procedure, we found that the probed length-scales are, at these low Reynolds number, smaller than the quantum (dissipative) scale of the flow, determined, in He II, by the average distance between quantized vortices ℓ and, in He I, by the Kolmogorov dissipative scale η . For Reynolds numbers larger than 10^4 , the effect vanishes and He II behaves similarly to He I, as it is expected for mechanically driven coflows of superfluid ^4He at length scales exceeding the average distance between quantized vortices. This suggests that, similarly to thermal counterflow [105], both viscous and quantum features can be observed in mechanically driven flows of He II, depending on the length scales at which the quantum flow is probed.

Note, however, that the observed effect might also be influenced by the much larger thermal conductivity of He II, compared to that of He I, leading to different dissipation mechanisms of the parasitic energy input. Additionally, the obtained $\langle v^2 \rangle$ values are affected by the data scatter, which cannot be neglected here. In order to clarify the reported behavior, future studies should therefore be devoted to increase the data set size, as this will likely lead to less uncertainty in the evaluation of various physical quantities of interest.

Chapter 5

Streaming flow

5.1 Introduction

In the case of classical viscous fluid of kinematic viscosity ν , such as normal liquid He I, near an obstacle oscillating with a relatively small¹ amplitude A at angular frequency Ω , inside the so-called Stokes layer, the fluid copies the motion of the boundary up to a distance of the order of the viscous penetration depth $\delta = \sqrt{2\nu/\Omega}$ [106], where the phase of the fluid motion slips due to its inertia and the amplitude of its oscillatory motion decreases exponentially with the distance. The mean displacement of the fluid particles over an oscillation cycle is *close* to zero.

At time scales much longer than the oscillation period, however, the Reynolds stresses and the viscous forces between the parts of fluid forced by different parts of the oscillating obstacle cause a slow steady flow. Due to the mass conservation, this flow can create closed loops called *streaming cells*, as it is schematically drawn in figure 5.1 for a cylinder, which represents an often studied object [74] in theoretical [107] as well as in experimental studies [108].

In the case of a translationally oscillating infinite cylinder, as shown in figure 5.1, it was found that, if the streaming Reynolds number $Re_s = \Omega A^2/\nu$ is smaller than 37 [73], the steady streaming flow is not closed. If Re_s is greater, the streaming flow closes [107], the streaming cells are formed and, at their outer boundary, the subsequent *outer streaming patterns* can be formed via the viscous induction [72]. They are oppositely oriented with respect to the inner ones and, at sufficiently high Re_s , they can close, creating cells and the described process can repeat itself. The thickness of the *inner streaming cells* δ_{DC} is always greater than the *oscillatory Stokes boundary layer* thickness $\delta_{AC} = \sqrt{\nu/\Omega} = \sqrt{2}\delta$ and depends non-trivially on Re_s , exhibiting $\delta_{DC} \sim s/\sqrt{Re_s} \sim \delta_{AC}/\epsilon$ scaling, see [43].

The streaming problem is often theoretically studied in polar geometry around an infinite cylinder or a sphere [106, 107], see also the review [71], alternatively near a stretched plane [109]. Because the *curvature* of the surface plays an important role [72], the corners are responsible for the streaming in the case of a rectangle, as has been numerically shown by [110], whose results are freely redrawn in figure 5.2.

¹Compared to the size of the body.

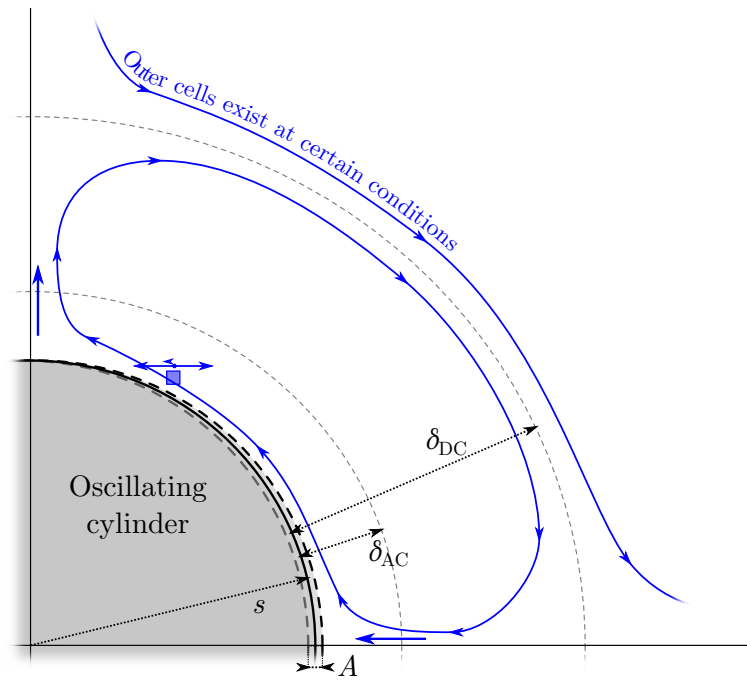


Figure 5.1: The drawing of the streaming problem as studied theoretically. A denotes the amplitude of the obstacle motion, s is its size and δ_{AC} represents the thickness of the *Stokes layer*, while δ_{DC} the thickness of the inner streaming cells, further details in text. Dimensions are not to scale.

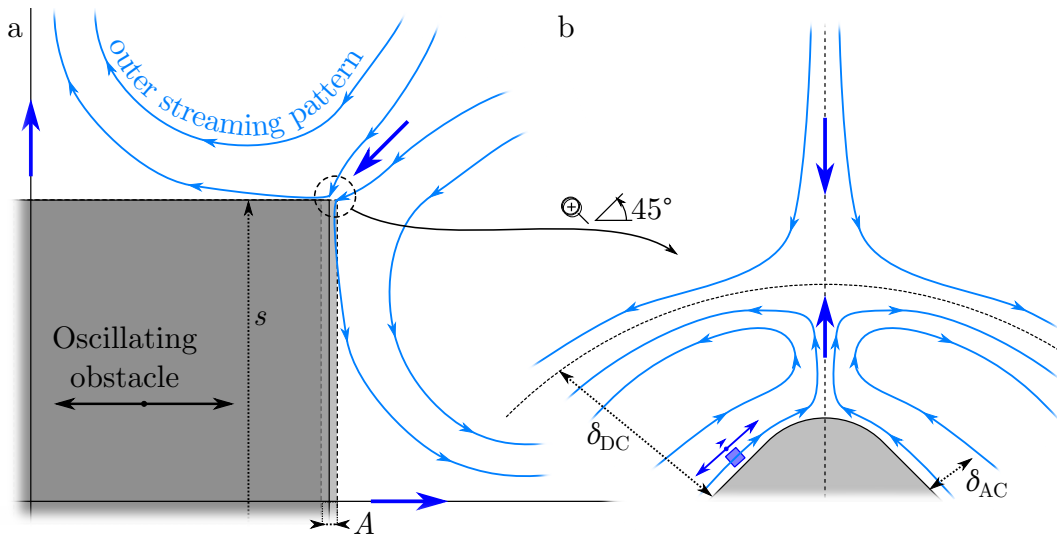


Figure 5.2: The drawing of the streaming problem near a rectangle. The figure is drawn according to the numerical results of [110]. Similarly to the figure 5.1, A denotes the amplitude of the obstacle motion, s is its size and δ_{AC} represents the thickness of the *Stokes layer*, while δ_{DC} the thickness of the inner streaming cells. Dimensions are not to scale.

5.2 Results

A detailed description of the experimental setup was given in chapter 2, here is only a short recapitulation. The measurement PTV² technique is used, with solid deuterium particles. The flow is generated by an oscillating quartz tuning fork of main resonant frequency 8300 Hz at He II temperatures, the fork's prongs point to the camera and are illuminated from side by a laser sheet produced by a solid state laser, whose beam is defocused in the vertical direction. The laser sheet crosses the fork close to the tip, unfortunately, we do not know the exact position. The fork is driven electrically with the ac voltage up to $77 V_{\text{rms}}$ producing maximum velocity of the fork up to 340 mm/s; this value of the velocity was measured as the electrical current through the fork, see equation 2.9, whose result is trustworthy only approximately, see figure 2.9 obtained in a different measurement.

The data acquisition procedure is as follows: first, there is an injection of pure helium gas from room temperature under pressure around 1.5 bar by using our *seeding system*, section 2.3. This injection stirs up the deuterium particles seeded at the bottom of the cryostat and allows us to measure. On the other hand, such injection creates a strong residual flow, therefore we have to wait until this flow is dampened, or, at least, suppressed to the level weaker than the studied flow. After this injection we start driving the fork and 30 s after the injection we start acquiring images by the camera at the frame-rate 800 Hz, which is $10\times$ slower than the fork oscillation frequency. The laser illuminating the particles (and the fork as well) is operated in the *pulse regime*, at the same frequency as the camera. The movie usually consists of 2000 images, hence its length is 2.5 s. After it is completed, the data transfer from the camera into the computer starts.

5.2.1 Data sets

We have recorded several sets of movies in He I as well as in He II, at different drives. Tables 5.1 and 5.2 summarize the achieved velocities and numbers of tracked trajectories, after data manipulations, such as: adding missing points into the trajectories by linear interpolation; Komogorov-Zurbenko linear smoothing [65] (not changing the number of points); removing trajectories shorter than 10 points to decrease noise; and, for movies recorded in He I at 2.2 K, also removing fake trajectories produced by reflections on a tiny bubble formed at the illuminated side of the fork due to local overheating and boiling.

Examining the table 5.1, one can notice that the fork tip velocity v_{el} measured at higher drive in He I (Z77 group) is closer to the fork tip velocities at the low drive in He II (groups F22, M22 and A22). This is caused by the higher damping in He I, compared to that in He II.

The fork tip velocity values in He I (i. e. group Z77 in table 5.1) are rather widely scattered, while the scatter in He II is reasonable (standard deviation $\sigma_{\text{HeII}}[v_{\text{el}}] = (1-14)\cdot 10^{-3}$ m/s). This is most likely caused by the boiling/cavitation occurring in He I and by worse temperature stabilization. The steep temperature dependence of the sound velocity could be an additional factor, due to possible damping or amplification by acoustic resonance [111].

²Particle tracking velocimetry.

Table 5.1: The data groups measured in the experiment and their physical conditions. T stands for the temperature of the bath deduced from the measured *saturated vapor pressure*, F_{el} is the electrical piezoelectric force driving the fork, set up by the applied ac voltage, and $\langle v_{\text{el}} \rangle$ is the fork tip velocity measured via the electrical current, see section 2.5. ν represents the effective bulk kinematic viscosity of the bath at corresponding temperature, data taken from [5], Re_s is the *streaming Reynolds number* $Re_s = (\Omega A^2)/\nu$, where A is the oscillation amplitude estimated as $A = \langle v_{\text{el}} \rangle / \Omega$. Following [43], ϵ is the ratio of this amplitude and the characteristic size of the oscillator, which we choose to be the thickness of the fork $T \approx 0.4$ mm. The table continues below as table 5.2.

group	T [K]	F_{el} [μN_{rms}]	$\langle v_{\text{el}} \rangle$ [m/s]	ν [m^2/s]	Re_s	ϵ
Z77	2.22	41	$2.1 \cdot 10^{-1}$	$1.9 \cdot 10^{-8}$	$4.5 \cdot 10^1$	$1.0 \cdot 10^{-2}$
F77	1.95	41	$3.4 \cdot 10^{-1}$	$9.6 \cdot 10^{-9}$	$2.3 \cdot 10^2$	$1.6 \cdot 10^{-2}$
F22	1.95	12	$1.7 \cdot 10^{-1}$	$9.6 \cdot 10^{-9}$	$5.8 \cdot 10^1$	$8.4 \cdot 10^{-3}$
M77	1.57	41	$3.4 \cdot 10^{-1}$	$9.1 \cdot 10^{-9}$	$2.4 \cdot 10^2$	$1.7 \cdot 10^{-2}$
M22	1.57	12	$1.8 \cdot 10^{-1}$	$9.1 \cdot 10^{-9}$	$7.1 \cdot 10^1$	$8.9 \cdot 10^{-3}$
A77	1.22	41	$3.4 \cdot 10^{-1}$	$1.2 \cdot 10^{-8}$	$1.9 \cdot 10^2$	$1.7 \cdot 10^{-2}$
A22	1.22	12	$1.9 \cdot 10^{-1}$	$1.2 \cdot 10^{-8}$	$6.0 \cdot 10^1$	$9.3 \cdot 10^{-3}$
S77		41	$3.4 \cdot 10^{-1}$			
S22		12	$1.8 \cdot 10^{-1}$			

Note also that, while the ratio of higher to lower drive force is 3.4, the ratio of velocities is $1.88 \approx \sqrt{3.4} = 1.85$, because in the turbulent regime the drag force depends on the velocity quadratically.

While examining the table 5.2 that shows the observed particles' velocities (column $\langle |v| \rangle$), we have to realize that the camera acquisition frequency 800 Hz is $10\times$ smaller than the fork oscillation frequency, hence this fast contribution can hardly affect the velocity calculated as the particle displacement between the following frames. Secondly, an important notice is that the velocity values are calculated from the whole field of view, in which the spatial distribution of particle velocity is strongly inhomogeneous, see figure 5.3-second panel, therefore it is not possible to compare these values to the expected streaming flow velocity $V_s = \epsilon \Omega A \approx 5.4$ mm/s defined in [43]. This statement holds also for other quantities given in table 5.2 - they are however useful for comparison among different groups.

5.2.2 Observations

The main quest of this chapter is to find out if the streaming pattern exists in superfluid helium. For the start, we have to be sure that we are actually able to see such a pattern with our experimental setup. Let us take as a „pilot“ group the Z77 data set, obtained in He I, which is a classical viscous liquid, at the highest attainable drive. According to the electrical current through the fork, the fork tip velocity $v_{\text{el}} \approx 210$ mm/s, the corresponding *streaming Reynolds number* $Re_s = (\Omega A^2)/\nu = v_{\text{el}}^2/(\Omega \nu) \approx 45$ might be large enough (according to [72] it ought to be greater than 37) to close the incoming and outgoing streaming jets into closed *streaming cells* (see figure 5.1) at whose outer part the additional streaming

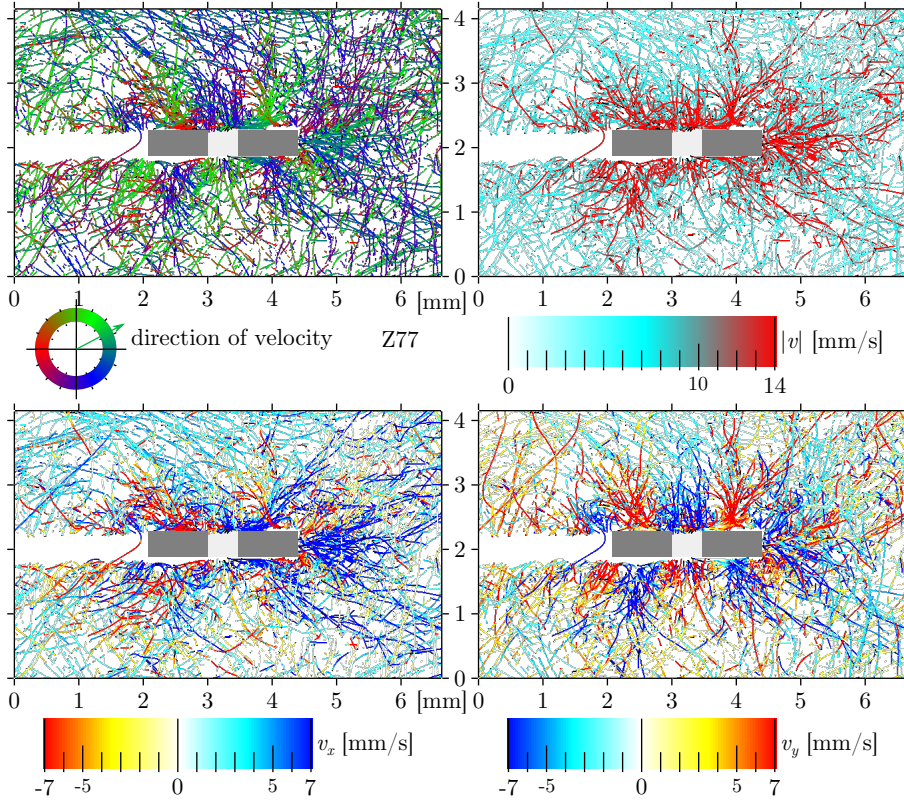


Figure 5.3: Trajectories obtained in He I, at the highest attainable drive – group Z77 in table 5.1. All panels show the same data colored via the direction of velocity, magnitude of velocity, horizontal component of velocity and vertical component of velocity, respectively. Gray rectangles display the position of fork prongs, the area in shadow is not highlighted.

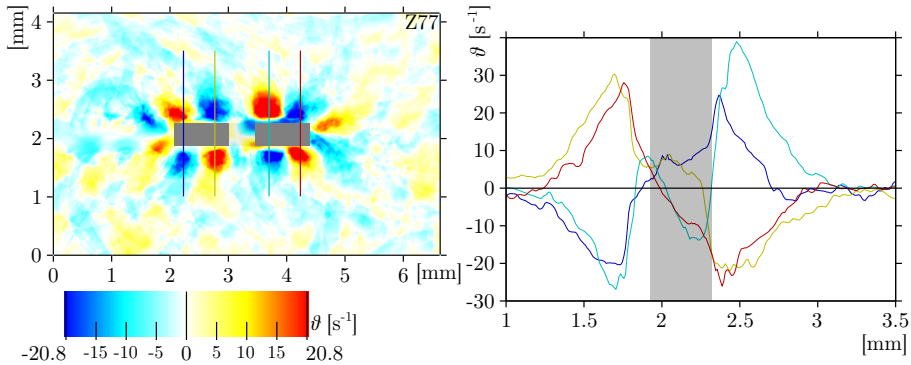


Figure 5.4: Map of the PTV-based Lagrangean pseudovorticity ϑ in He I, at the highest attainable drive – group Z77 in table 5.1. Blue color corresponds to clockwise dominant sense of rotation, while red one to the anticlockwise. The **right** panel shows cuts of the ϑ map along four lines drawn in the left panel.

Table 5.2: The second part of the table 5.1 – the measured properties of data groups. N_p and N_{tr} are the number of trajectory points and trajectories after the data manipulations, $\langle |v| \rangle$ is the average magnitude of the particle velocity, while $\sigma[v_y]$ is the standard deviation of its vertical component (perpendicular to the movement of the obstacle). $\langle \vartheta^2 \rangle$ is the mean square value of the Lagrangean pseudovorticity, see section 2.10. All values of $\langle |v| \rangle$, $\sigma[v_y]$ and $\langle \vartheta^2 \rangle$ are calculated from the whole field of view.

group	N_p [$\cdot 10^3$]	N_{tr} [$\cdot 10^3$]	$\langle v \rangle$ [mm/s]	$\sigma[v_y]$ [mm/s]	$\langle \vartheta^2 \rangle$ [s^{-2}]
Z77	596	14.3	3.3	3.3	11.7
F77	276	6.4	7.7	8.1	110.1
F22	166	3.5	3.4	3.5	40.5
M77	214	4.9	6.5	6.9	114.4
M22	241	4.7	3.4	3.4	26.6
A77	291	6.0	6.0	6.6	84.1
A22	184	2.9	3.6	3.3	36.8
S77	781	17.3	6.7	7.2	74.3
S22	591	11.2	3.4	3.4	17.3

cells might form. The thickness of the primary, or *inner, streaming cells* should be of order of the $\delta_{DC} = \frac{1}{\epsilon} \sqrt{\frac{\nu}{\Omega}} \approx 58 \mu\text{m}$ – rather small – only about 6 pixels – for our optical setup of resolution about $10.3 \mu\text{m}/\text{pix}$. At the same time we have to bear in mind that the discussed theoretical model has been constructed for a cylinder. Indeed as it follows from the theoretical works [74], [73], the curvature plays a significant role.

Let us examine our experimental findings. Figure 5.3 clearly demonstrates that *streaming cells* are observable by using our optical setup. This is even more apparent from the PTV-based Lagrangean pseudovorticity ϑ shown in figure 5.4. Therefore, we declare that we are able to resolve the streaming patterns and in the following we shall examine them in more detail.

Figure 5.5 clearly shows that the macroscopic streaming pattern exists also in He II, which is a quantum liquid. In this case the pattern is better recognizable on the base of the colored trajectories. The reason is that, although in the group F77 movies the fork is driven by the same force as in Z77, the achieved velocity is larger, as well as the streaming Reynolds number Re_s evaluated using the effective bulk kinematic viscosity. To calculate Re_s , we use the tabulated viscosity [5]. Again, the pattern is better pronounced in the form of a Lagrangean pseudovorticity map, see the right top panel of figure 5.6.

Although the ratio between the normal and superfluid components of He II varies in the probed temperature range substantially (from 50 : 50 at 1.95 K to less than 5% of normal component at 1.25 K), the achieved fork tip velocities remain similar, see table 5.1, as well as the measured average velocity of particles in the datasets, see table 5.2. The directly observed streaming patterns also look identical, see figure 5.6, where the map of the pseudovorticity ϑ at all three studied temperatures is shown. We believe that the displayed differences are of statistical nature only, because they seem to be smaller than the differences among individual streaming cells at symmetrical positions, which ought to be

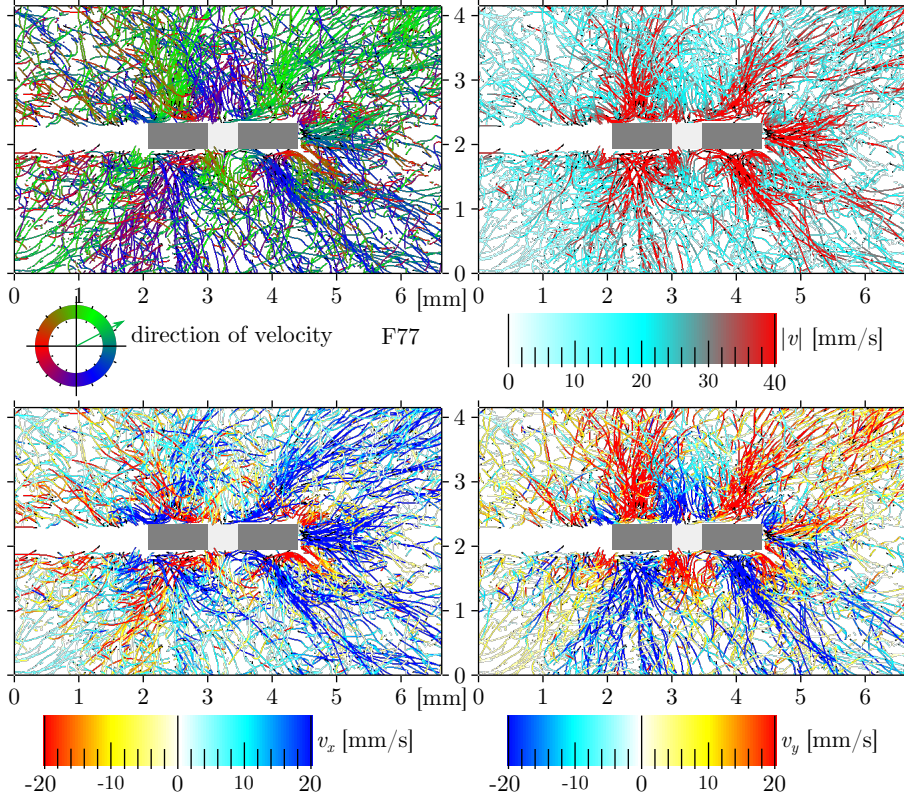


Figure 5.5: Trajectories obtained at 1.95 K (i. e., in He II) at the highest attainable drive – group F77 in table 5.1. All panels show the same data colored via the direction of velocity, magnitude of velocity, horizontal component of velocity and vertical component of velocity, respectively.

the same due to the symmetry. Hence we decided to merge the data obtained at the same drive at different temperatures into one group, in order to increase the statistical quality. Explicitly, groups F77, M77 and A77 are merged into the group S77, while F22, M22 and A22 into the group S22, with resulting parameters displayed in table 5.1.

The trajectories of the S77 group (i. e. the larger driving force in He II independent on temperature) are shown in figure 5.7 and the group S22 in figure 5.9, respectively. The streaming cells are nicely visible based on these merged trajectories, again even better as the pseudovorticity map, figures 5.8 and 5.10. We do not find it useful to show here all the particular data sets independently, because, as it was said, they are similar; the reader can find them on the attached CD.

The right panels of figures 5.4, 5.8 and 5.10 show cuts of the pseudovorticity spatial distribution highlighting the non-axisymmetric shape preventing us to use the method of vortex profiles described in the previous chapter. We see that the pseudovorticity ϑ changes faster on the side closer to the obstacle. Further, we see at the best only a weak evidence of a „plateau“ of ϑ in the center of the vortex predicted by Amromin [97]. This suggests that the core of the macroscopic vortex is significantly smaller than the integration area for calculating ϑ – its radius is $R_m = 0.4$ mm.

Comparison of the estimated value of δ_{DC} (the distance of the streamline which

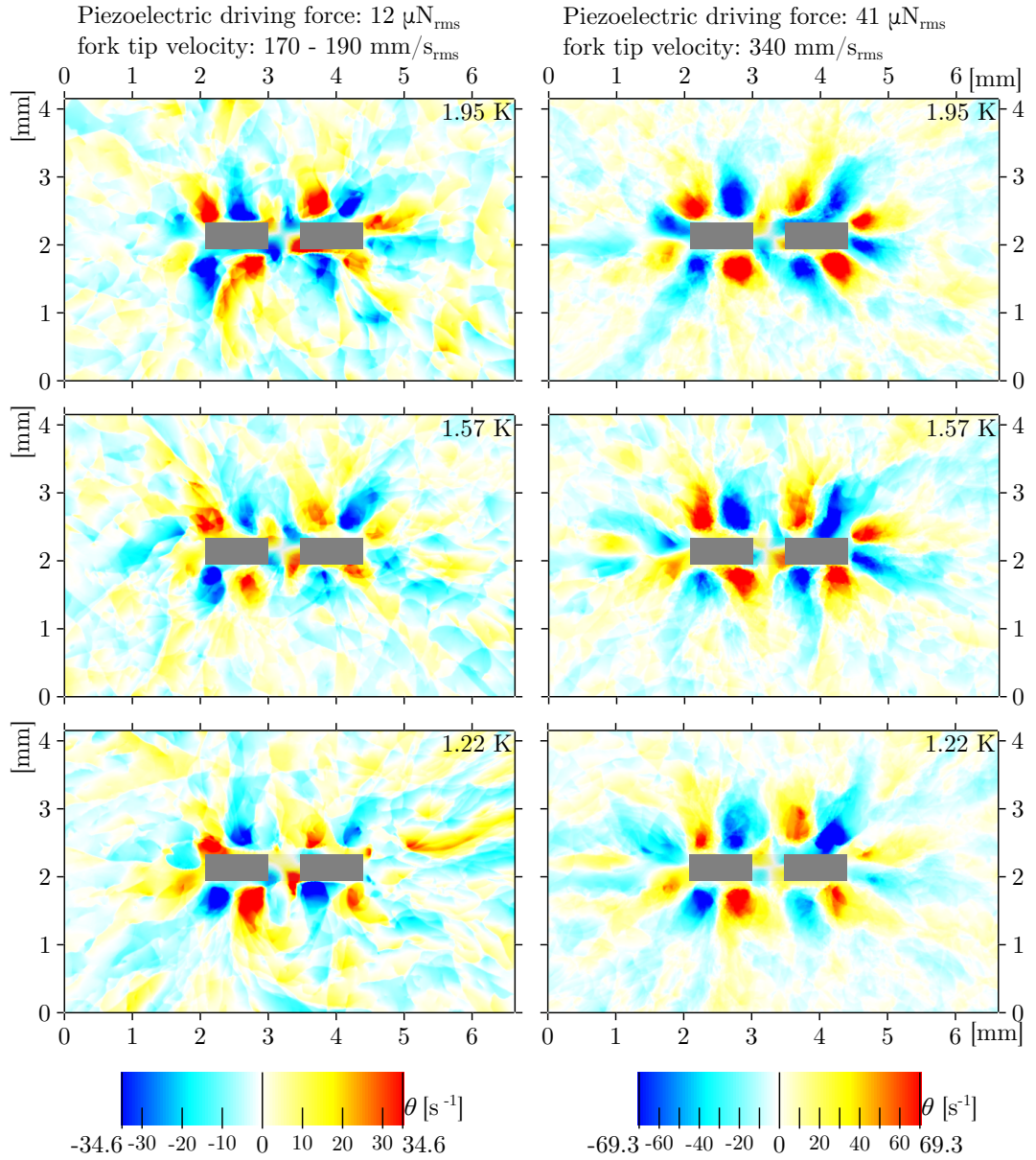


Figure 5.6: Map of PTV-based pseudovorticity ϑ at three different temperatures (in rows) and two different drivings (in columns) In the right top corner of each panel there is the name of group pointing into table 5.1. The legend is common for whole column. Blue colors correspond to clockwise dominant sense of rotation, while red ones to the anticlockwise. Do not forget that on the left side of the fork (indicated by a pair of gray rectangles) there is a shadow with no, or very little, data, hence the calculated values of ϑ are not trustworthy there.

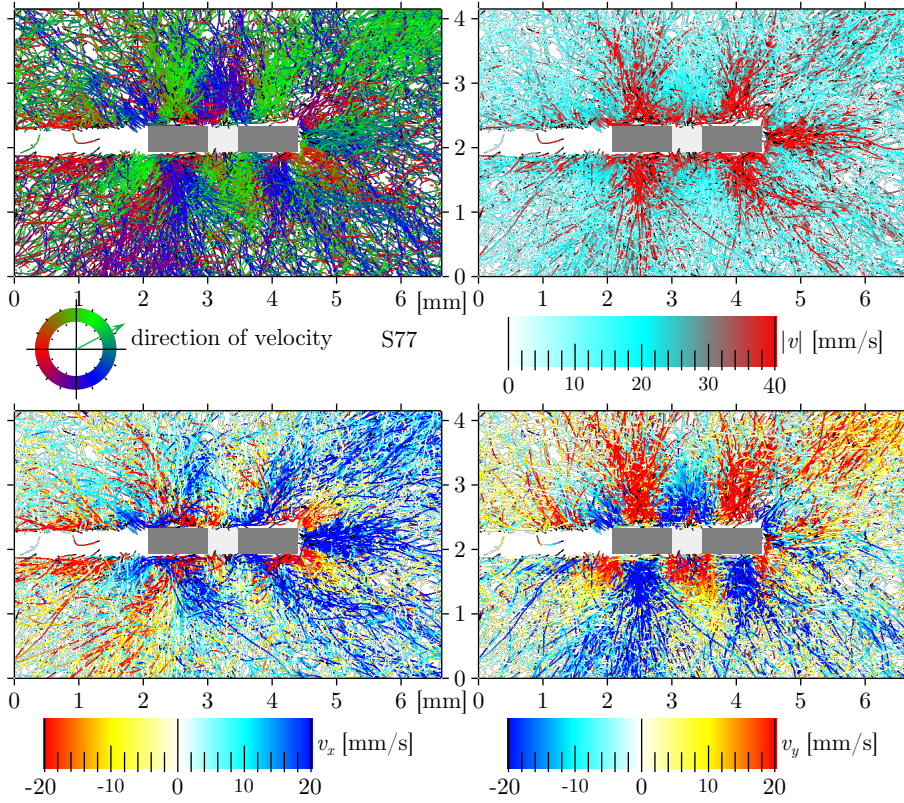


Figure 5.7: Trajectories obtained in He II at the highest attainable drive $41 \mu\text{N}_{\text{rms}}$, and fork tip velocity 340 mm/s . All panels show the same data colored via the direction of velocity, magnitude of velocity, horizontal component of velocity and vertical component of velocity, respectively.

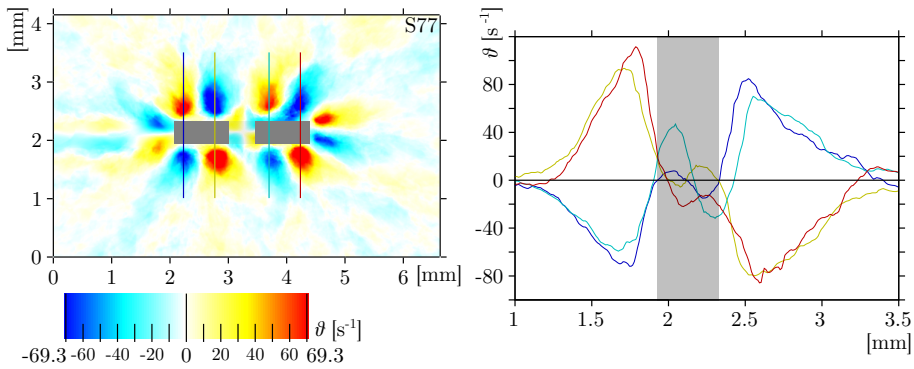


Figure 5.8: Map of PTV-based pseudovorticity ϑ in He II at the highest attainable drive. Blue colors correspond to clockwise dominant sense of rotation, while red ones to the anticlockwise. The **right** panel shows a cut of the ϑ along four lines marked in the left panel.

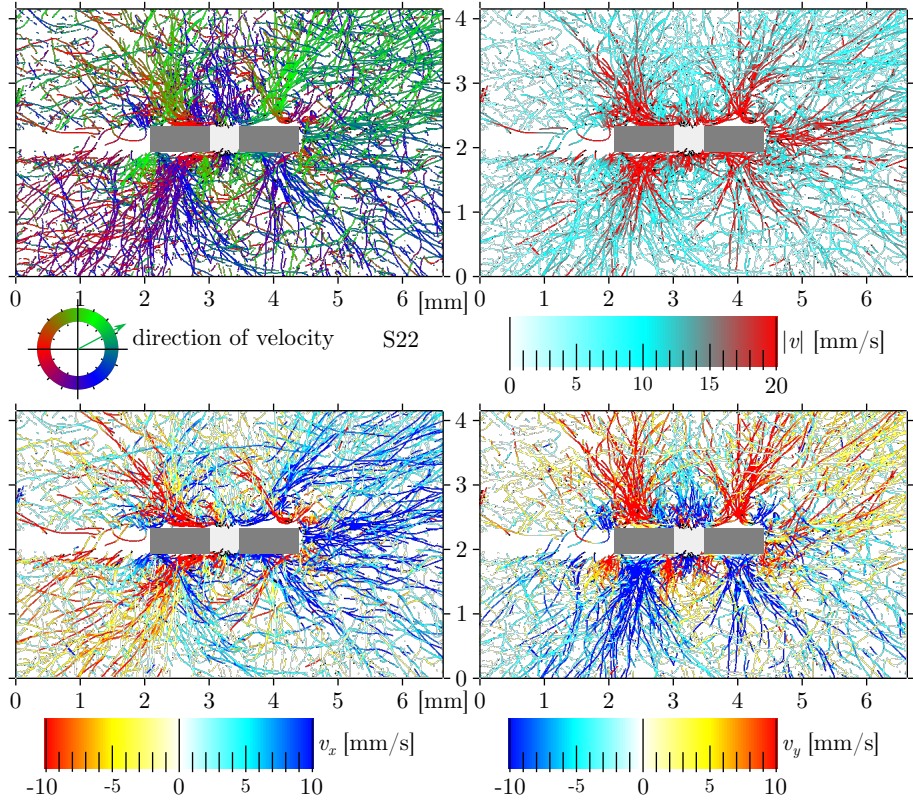


Figure 5.9: Trajectories obtained in He II at the smaller drive $12 \mu\text{N}_{\text{rms}}$ and fork tip velocity $\sim 180 \text{ mm/s}$. All panels show the same data colored via the direction of velocity, magnitude of velocity, horizontal component of velocity and vertical component of velocity, respectively.

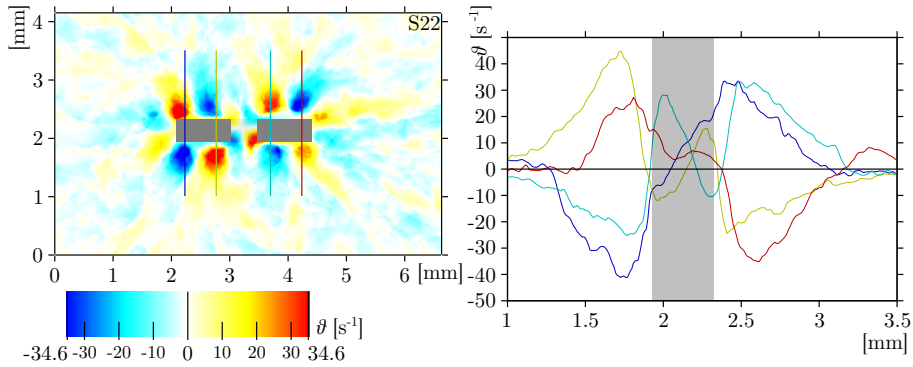


Figure 5.10: Map of PTV-based pseudovorticity ϑ in He II at the smaller drive. Blue colors correspond to clockwise dominant sense of rotation, while red ones to the anticlockwise. The **right** panel shows a cut of the ϑ along four lines marked in the left panel.

segregates the inner and outer streaming cells [43]) $\delta_{\text{DC}} = \frac{1}{\epsilon} \sqrt{\frac{\nu}{\Omega}} \approx 26 \mu\text{m}$ for He II and $58 \mu\text{m}$ for He I with the observed size of the streaming cells $\sim 0.7 \text{ mm}$, which can be read from figure 5.8, leads us to conclude that we observe the *outer streaming cells*.

Examining figure 5.6 one could perhaps imagine seeing an indication of the inner cells of opposite orientation close to the fork. We want to warn that this is more probably an artifact caused by the algorithm for calculating ϑ . In the area covered by the obstacle, there are no data, hence the algorithm returns the result as if the velocity there were zero, producing a fake signal of opposite sign *inside* and *near* the covered area. This is more strongly apparent in the right panels of figures 5.4, 5.8 or 5.10, where there are peaks of ϑ *inside* the obstacle (indicated by a grey area).

5.2.3 Summary of observations

There are strong outwards streaming jets both above and below the axis of each fork prong, that perpendicular to the direction of oscillation; these jets are compensated by suction jets from the sides with an angle of about 45° , but, between the prongs, the neighboring suction jets merge, creating a single one, parallel with the primary outwards streaming jets and of lower intensity. Hence, between neighboring (and oppositely oriented) jets, there are peaks of the PTV-based pseudovorticity ϑ , as it is apparent from figure 5.6. One naturally expects that the flow would close, creating streaming cells, but this is not directly demonstrated from the particle trajectories (figures 5.3, 5.5, 5.7 and 5.9). This might be due to the insufficient length of recorded trajectories, especially as we see only 2D projections of 3D flows and the trajectories are effectively shortened simply by the non-zero velocity component perpendicular to the illuminated plane.

5.3 Discussion

5.3.1 Number of streaming cells

In contrast to the figure 5.1 displaying 4 streaming cells with 2 outcoming jets around a circular cylinder, we have observed 6 cells and 3 outcoming jets around each fork prong. This can be explained by the large curvature of the prong corners, see figure 5.11a. It is not important how exactly the obstacle moves, but rather how moves the flow past it – the fluid near the corner flows as the blue arrow in figure 5.11a shows. Therefore, if we zoom in (figure 5.11a), the flow around the corner is locally symmetric around the axis of the corner and the oscillatory flow around it generates the steady streaming due to the Reynolds stresses with an outcoming jet pointing along the corner axis. But, this inner (or primary) streaming pattern is invisible for us as discussed above, therefore we see the complementary *incoming* jet in the outer streaming pattern and the complementary outcoming jets located at the centers of the sides generated simply due to the conservation of mass (or the equation of continuity). As the outcoming jets are always stronger than the (wider) incoming ones, the first type dominate the flow, see the magnitude of velocity in figure 5.11c.

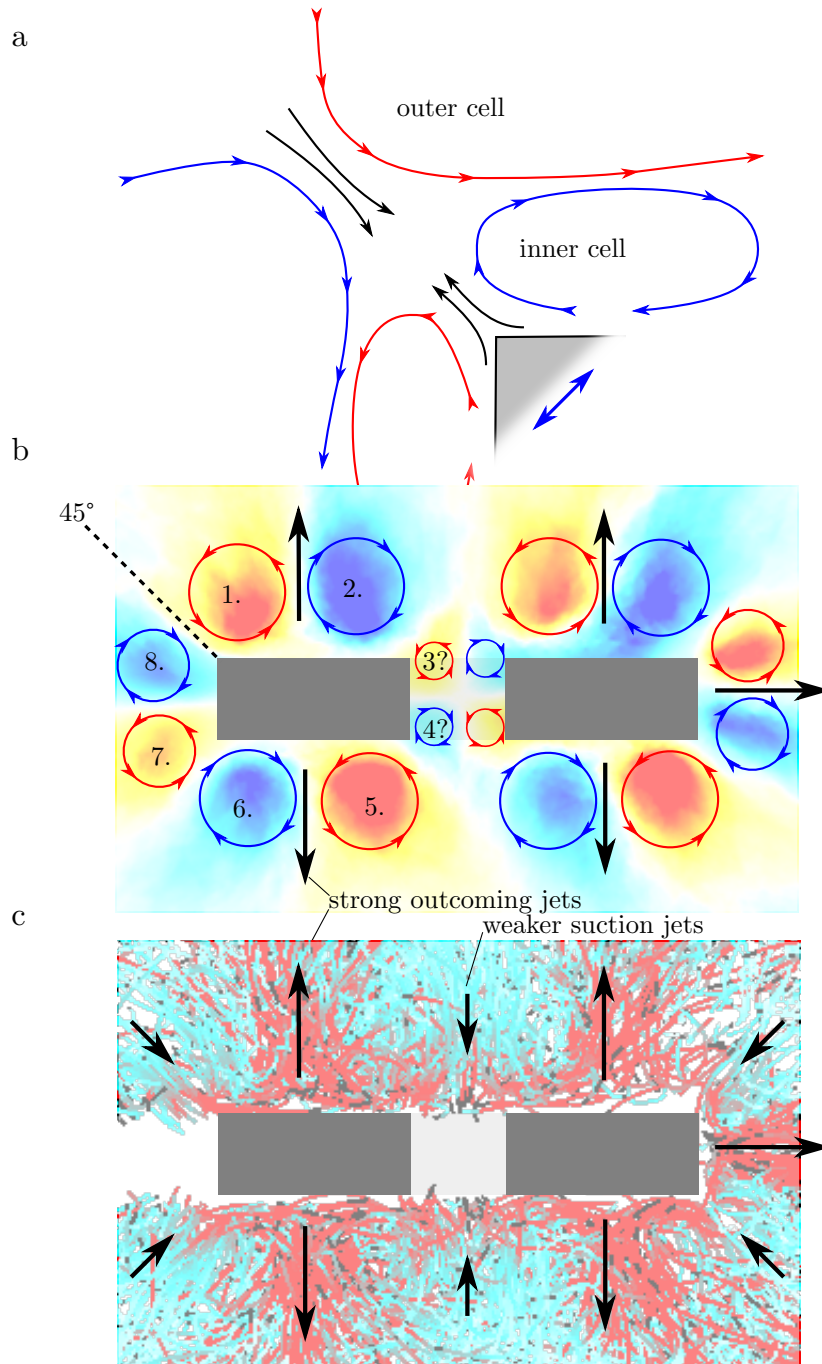


Figure 5.11: Panel Panel **a**: schematic view of the streaming flow features in the proximity of the fork top left corner (the fork oscillates in the horizontal direction). Locally the fluid flows past the corner symmetrically with respect to its axis. Panel **b**: The closeup of the Lagrangian pseudovorticity map calculated from all the data obtained in He II, with driving force $F = 41 \mu\text{N}$. Panel **c**: corresponding particle trajectories, color coded by velocity magnitude, see the top right panel of figure 5.7. The strong outgoing jets are shown with black arrows, as the weaker incoming jets, orientated along the axes of the prong corners. Each corner generates one incoming jet in the outer streaming pattern and 2 outer streaming cells (plus 2 invisible inner cells), in total 8 cells for one prong, although the ones numbered 3 and 4 are barely visible due to the lack of trajectory points in the shadow area.

By using the symmetry argument, we claim that there are 8 streaming cells around each prong, although the ones numbered 3, 4, 7 and 8 in the figure 5.11b are not directly observed due to the lack of data in the shadow area. In total, 16 streaming cells around the whole fork exist in the plane perpendicular to its axis.

5.3.2 Quantum length scale

In turbulent quantum fluids, an important length scale is the quantum length scale, defined as the *intervortex distance* ℓ . In the vicinity of our fork vibrating at given experimental conditions in He II it can be estimated directly from the second sound measurements [112] as $\ell \approx 50 \mu\text{m}$. This estimate provides, however, an average over a large flow region in the neighborhood of a tuning fork similar to ours and represents an upper limit of ℓ (note that, as reported in [54], ℓ can also be obtained from the flatness of the particle velocity distributions). Other estimates of ℓ in the closer vicinity of the fork have been discussed in [113], based on considerations of energy dissipation by quantized vortices. They yield intervortex distance $\ell_{\times} \sim 0.5 - 2 \mu\text{m}$, for the unpolarized vortex tangle, while for the partly polarized one, based on a classical Kolmogorov-like approach, $\ell_{\parallel} \sim 1 - 3 \mu\text{m}$.

It follows that this study, at experimentally accessible length scales, shows the behavior of He II in the flow regime, when the number of quantized vortex lines is so large that they dynamically lock the *normal* and the *superfluid* components together, hence closely similar results in He I and in He II can indeed be expected.

5.3.3 Choice of R_m

The calculation of the PTV-based Lagrangean pseudovorticity ϑ is strongly dependent on the choice of integration area size, R_m [114]. As it was already discussed in section 2.10, ϑ converges to vorticity ω of a single continuous flow field, (i) if the size of the integration area converges to zero, (ii) if the tracking particles are fluid particles and (iii) if the density of seeding is infinite. None of these conditions is fulfilled in our experiment. On the other hand, we can at least aim to optimize the validity of our results, by maximizing the number of particles. This was indeed achieved by merging multiple data sets, obtained at the same or at least similar conditions, and by optimizing the size of the integration area finding a right balance between statistical quality and locality.

Figure 5.12 shows values of ϑ^2 and examples of its spatial distribution for different values of the parameter R_m . With larger R_m , there are more data with larger distance from the probed point, which results in systematically smaller ϑ^2 , see panel A of figure 5.12. In the case of random velocities, the sum of ϑ^2 scales as R_m^{-2} . Panel B of figure 5.12 shows compensation of this first order effect.

Another regime of scaling takes place at smaller values of R_m , when $\langle \vartheta^2 \rangle R_m^2 \sim R_m^{-1}$, hence $\vartheta \sim R_m^{-3/2}$, which corresponds to spatial correlation in the integration area, but we lack any explanation. Additionally, it is possible to notice a small „bump“ in this regime at $R_m \approx 0.7 \text{mm}$, which can be connected with the strong coherent structures in the flow field of the fork, which occupy a relatively small area when compared with the background characterized by small random velocities.

Finally, if we would increase R_m over the size of the field of view, ϑ might no

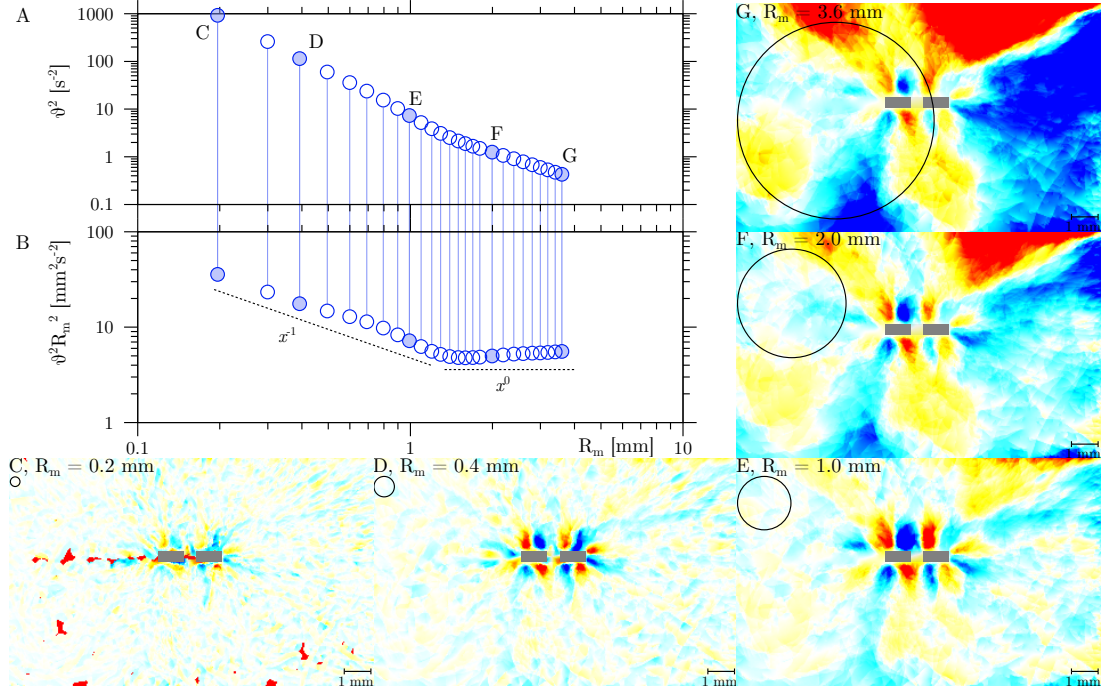


Figure 5.12: The panel **A** shows the dependence of overall square of ϑ as the function of R_m , while the panel **B** shows the same values multiplied by R_m^2 to neutralize the statistically caused scaling. Other panels, **C** – **G**, show examples of the spatial distribution of the Lagrangean pseudovorticity ϑ in the M77 group at highlighted values of the parameter R_m . Black circles indicate the actual size of the integration area for calculating ϑ . For detailed analysis, $R_m = 0.4$ mm has been chosen, which corresponds to the thickness of the tuning fork.

more depend on R_m as it were calculated using all data anyway. This regime is not displayed in figure 5.12.

Other panels of figure 5.12 show that at larger values of R_m the map of ϑ tends to highlight larger structures, which can easily be *artifacts* produced due to the lack of data behind the boundary of the field of view. On the other hand, too small R_m results into too small number of trajectory points used for calculating ϑ in certain position, and the result is devalued. As the final value of R_m , we have chosen $R_m = 0.4$ mm, which corresponds to the thickness of the tuning fork, i. e. its side which pushes the fluid. This allows to recognize the produced vortical structures of similar size.

A sceptic can argue that we cheat a bit when analyzing our results by favoring the size of vortices we expect and would like to see, but the existence of vortices of such a size is clearly visible also for different choices of R_m . Moreover, their size is also apparent from the recorded particle trajectories.

5.3.4 Resonance stability

Another effect, which rather strongly affects the precision of our velocity measurement in all cases, is the sedimentation of the particles on the prongs of the fork. It slightly increases their effective mass and decreases the resonant frequency of the fork. A tiny increase of the effective mass, $\sim 3 \cdot 10^{-11}$ kg, explains

the observed downshift by $\sim 5 \cdot 10^{-2}$ Hz, which is enough to move the fork slightly off resonance and change the fork tip velocity up to ~ 30 mm/s during the time between particles injection and measurement, i. e., within about 30 s. Estimated change of mass corresponds to the sedimentation of around ~ 300 particles of mass of order of $1 \cdot 10^{-13}$ kg on the surface of the fork, i. e., sedimentation rate around 10 particles per second along whole length of the fork. In the data group S77, 174 particles were observed to touch the fork, i. e., within the overall recording time of the S77 data group – 45 s – sedimentation rate 4 particles per second only on the illuminated length close to the tip of the fork has been directly observed.

5.3.5 Thermal counterflow

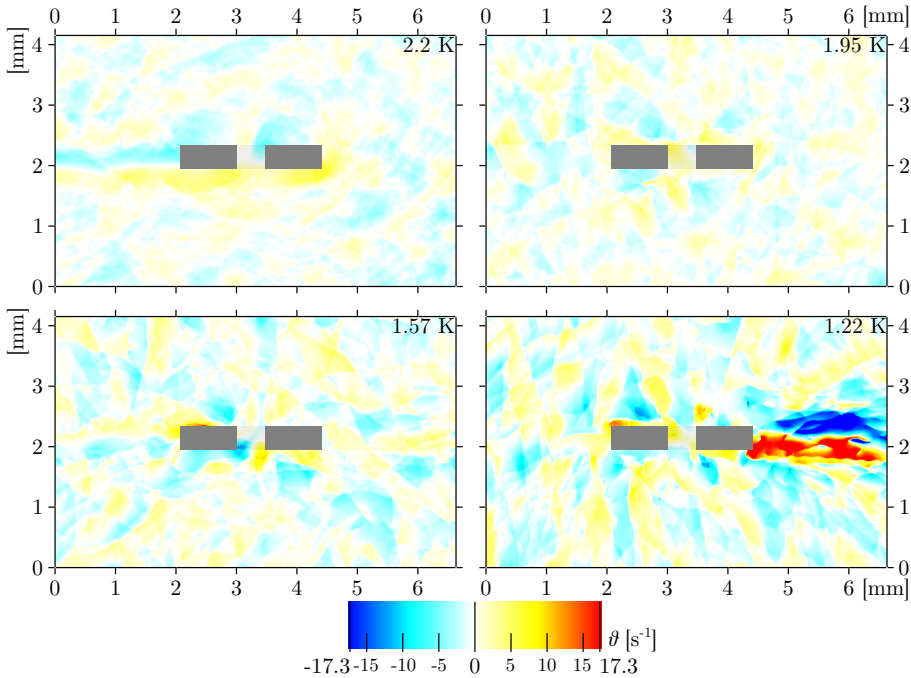


Figure 5.13: Map of PTV-based Lagrangean pseudovorticity ϑ around stationary fork – a „background“ – at different temperatures in both He I and He II. The color code, the same for all panels, is highlighting the effect of thermal counterflow produced at the illuminated side of the fork. It is most pronounced at the lowest temperature, as the counterflow velocity grows rapidly with decreasing temperature.

Figure 5.13 summarizes the data with no applied drive to the fork, at four studied temperatures. In all panels of figure 5.13, one can recognize random background flow field produced by the residual motion after the particle injection. At the lowest temperature 1.22 K, it is dominated by a counterflow jet produced at the illuminated side of the fork. As the ratio of *normal component* decreases with decreasing temperature, its velocity increases rapidly in order to maintain the total mass flow zero, therefore the counterflow jet is more apparent at the lowest temperature, as the particles in this case (low vortex line density) are mainly dragged away from the heated surface by the viscous normal component.

Unfortunately, we are not aware of any possibility to compensate for the counterflow effect, since we lack any better approximation of the particle motion in this area, as there is a shadow at the opposite side of the fork where only very big particles are visible and the statistics there is poor, much worse than on the illuminated side. On the other hand, comparing the actual magnitude of the color map in figure 5.13 with previous figures displaying ϑ we venture to say that this effect does not appreciably affect the observed pattern in He II.

The observed particle velocity at the lowest temperature (figure 5.13, the last panel) in the right of the illuminated side is about 8 mm/s, but it is difficult to determinate it as it is inhomogeneous and there are no particles close to the source. Let us point out that it was observed in another experiment [115] not described in this work that the particles leave the area close to the heater quite fast. Here the used laser power is 170 mW in the whole beam, which is diverged by the cylindrical diverging lens located 450 mm in front of the center of the experimental volume, hence the total power flux illuminating the discussed side is about 3.5 mW/mm². The surface of the fork in the discussed area is covered by gold layer, the reflectance³ of gold is 82% at the used wavelength 532 nm. Assuming that all light, which is not scattered, is transformed into heat, the heat flux is 640 W/m². The corresponding velocity of normal component is $v_n = \frac{q}{\rho_{ST}} = 55$ mm/s, which would be valid in a narrow channel.

5.3.6 Bubble in He I

The laser heating an illuminated surface produces a boiling bubble in He I, as its nucleation energy is not high when the working point is very close to the saturated vapor pressure curve, separated from it only by the hydrostatic overpressure by about 30 cm of liquid. This bubble scatters light, producing chaotically moving reflections, which are interpreted as particles by the tracking algorithm. These reflections move, therefore it is not possible to remove them by subtracting the average, as it is done for the reflections produced by the fork. We use a „ruder“ method to remove them. We remove all trajectories that stay in a small volume close to the illuminated side for entire time over which the bubble exists. The trajectory of a particle, which comes from far or leaves such a volume, is considered to be real and is saved. We did not attempt to repair the particle positions optically moved by the curved surface of the bubble.

5.4 Conclusion of the chapter

By using the particle tracking velocimetry technique, we have observed streaming patterns in the bulk liquid surrounding an oscillating quartz tuning fork in both He I, which is a classical viscous fluid, and He II, which is a quantum liquid displaying the two-fluid behavior and superfluidity. At the experimentally probed length scales, the observed flow patterns are similar in both fluids and are found to be consistent with those due to a square cylinder vibrating in water [110].

³In this spectral region gold changes its reflectivity a lot from 40% under 450 nm to almost 100% above 650 nm.

As our experimental length scale is significantly larger than the viscous penetration depth, any flows inside the Stokes boundary layer are currently invisible to us. At the probed length scale, larger than the quantum length scale – the mean distance between quantized vortices, we do not observe any appreciable influence of the quantization of vorticity in He II. We argue that this can be understood based on the notion that the mechanically driven turbulent co-flow of He II investigated here can be described as if it were a flow of a single quasiclassical fluid characterized by an effective kinematic viscosity, due to the action of the mutual friction force that at scales equal to or exceeding the probed one couples the motions of the two components of He II [116, 88, 34, 66].

Last but not least, there are practical aspects to our investigation. Although quartz tuning forks are employed as convenient probes in both ^4He [59] and ^3He [117] liquids, the very existence of a streaming flow, generated by their fast oscillations, its extent, and possible influence on their performance has not yet been investigated in detail. In both normal He I and in superfluid He II we show that, in the range of investigated parameters, a vibrating quartz tuning fork does appreciably influence its fluid surroundings, at least up to a distance of the order of its cross section size. Future studies could then focus on quantifying how the performance of this valuable experimental tool as well as similar oscillating objects used in superfluid hydrodynamics is affected by the generated streaming flows, existence of which our study demonstrates.

Chapter 6

Cavitation

In this chapter we show that very intense oscillatory flows of liquid helium studied in this Thesis could eventually lead to an interesting physical phenomenon known as cavitation. Generally, the *cavitation*, similarly as the *boiling*, is the process of nucleation bubbles in a liquid. While the boiling is generally understood to be caused by local overheating, the phenomenon of cavitation is a result of local „*underpressure*“ in the liquid.

6.1 Introduction

The understanding of cavitation in both classical and quantum liquids, or more generally – detailed microscopic mechanism of bubble nucleation in them, remains largely an open problem [118], although its phenomenological description in classical viscous liquids [119] is valued for practical engineering purposes. The difficulty of the detailed description of the nucleation mechanism lies in the area between the validity of the continuum hypothesis and the individual particle approach [120], hence quantum mechanics has to play an important role not only in quantum fluids but even in the case of classical liquids [121]. To this end, liquid helium offers a unique opportunity to study this problem both in He I, which is a classical low density liquid possessing very low kinematic viscosity [59] and in He II, which is a quantum liquid exhibiting the two-fluid behavior [34]. One can hope to discern which aspects of cavitation are common and different in classical and quantum liquids and, subsequently, such studies ought to help in developing the detailed microscopic description of the nucleation problem [121].

The presented experiment extends the previous investigations of cavitation in liquid helium due to an oscillating quartz fork performed by our colleges and published in [122], where it is shown that cavitation can easily be detected by monitoring the frequency sweeps across the resonant frequency of the fork, as the electrical response collapses when cavitation occurs. In article [123], the analysis of their results based on the Bernoulli equation in He II suggested pure cavitation, albeit heterogeneous in nature. Moreover, based on the measured temperature dependence of the critical cavitation velocity that steeply increased (from about 0.6 m/s to about 2.1 m/s for a particular fork) on decreasing temperature within about 20 mK below the superfluid transition in the bulk Blažková et al. concluded that in He I the vicinity of the fork is locally overheated and cavitation occurs here at a higher temperature than that at which the surrounding helium bath

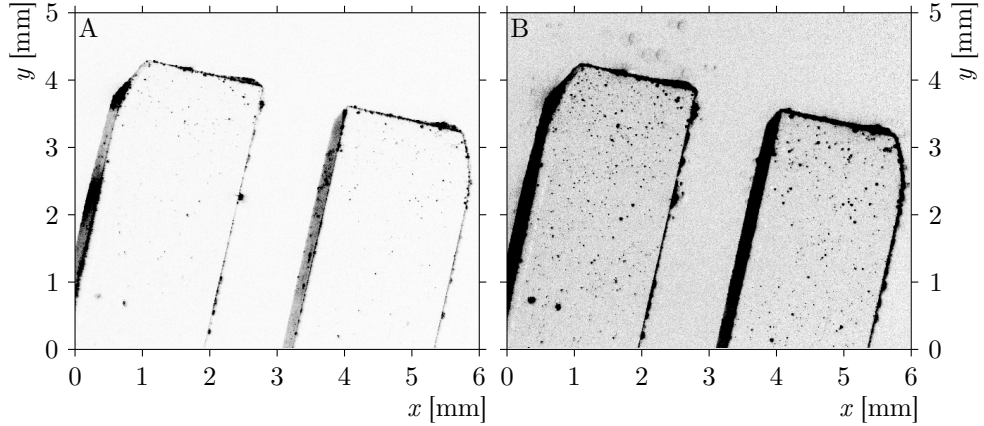


Figure 6.1: An example of acquired images of the fork with no drive: **A:** in He II – note small particles of dirt used to measure the velocity; **B:** in He I – the image has been darkened in order to highlight the bubbles appearing due to boiling near the fork surface overheated by the laser, confirming the presence of He I. All photographs presented here are displayed in negative.

is kept. They speculated that the steep increase of the cavitation threshold just below the superfluid transition can be understood as a consequence of the high convective heat transfer efficiency in superfluid He II compared to He I. This explains why, in accord with the previous observations [124], it is more difficult to reach the cavitation in He II than in He I.

Motivated by recent work by An Qu et al. [125] reporting differences in the lifetime of bubbles in He I and in He II, in this chapter we focus on the size and shape of the cavitation bubbles produced heterogeneously by the flow enhancement by excrescences on the surface of the oscillating quartz fork in He I as well as in He II.

6.2 Experimental setup

The cavitation was produced by decreasing the local pressure by velocity enhancement, by passing a moving object – a prong of the quartz tuning fork. The cavitation is detected optically by camera and illumination laser. See more details about the whole experimental setup and instruments in the chapter 2. The used fork has length $L = 19.7$ mm, thickness $T = 0.8$ mm and width $W = 2.2$ mm, see the figure 2.6 for meaning of these lengths. The main resonant frequency is 4186 Hz and the fork constant $a = 3.4 \cdot 10^{-5}$ C/m, see the chapter 3 for more details.

The velocity of the fork prongs have been measured independently by two ways: first the standard electrical measurement as described in section 2.5 or in article [60], second a direct optical measurement of elongation of the projection of small dust particles attached on the fork surface as visible in figure 6.1. The comparison of these two velocities is plotted in figure 2.9 in section 2.5.

The overview of measured cases is plotted in figure 6.2. Note that we were not able to reach cavitation at lower temperatures, as our maximum attainable velocity is up to 1 m/s, which is sufficient in He I but not in He II, in agreement

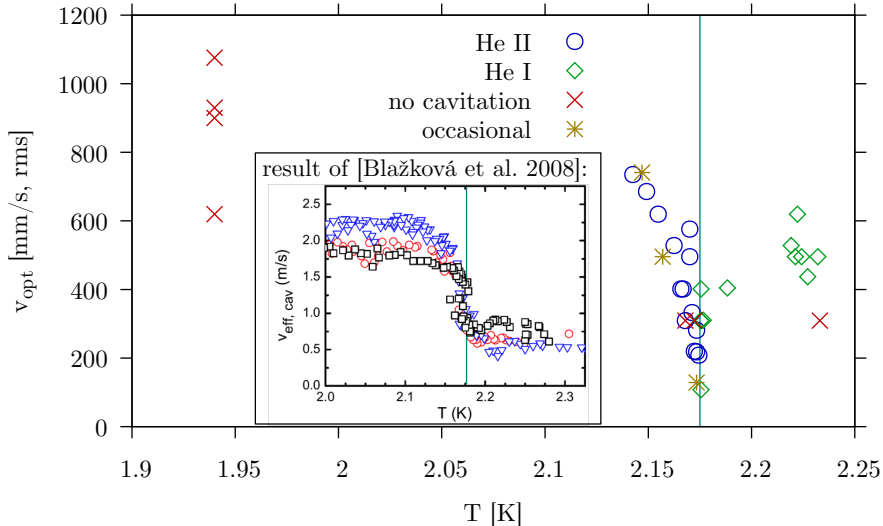


Figure 6.2: Temperature and achieved velocity of the measured cases. Blue circles and cyan squares denote the movies, where the cavitation has been observed in He II or He I respectively; red crosses are cases when cavitation was not observed; and orange stars denote movies with occasional appearance of tiny bubbles. The vertical line highlights the temperature of the λ -transition T_λ . The **inset** shows results of the previous work of our group [122]; it shows the critical velocity at which cavitation causes a collapse of the resonance peak.

with previous results of our group [122], see inset of figure 6.2.

6.3 Observations

The surprising observation is that there is a cluster of small bubbles instead of one large nearly hemispherical bubble as minimization of the sum of the energy of surface tension and volume Gibbs energy would suggest, see figures 6.3 and 6.4. Note that although the camera exposure time, 9.998ms, is much longer than the fork cycle period, 0.24ms, the scene is illuminated only during the laser pulse, i. e. for ~ 0.4 ms, corresponding to about 1.7 fork periods. This ensures capturing of the entire fork period and, on the other hand, the captured image is not a superposition of many periods. In He I we sometimes observe that the bubbles live longer than one cycle; these bubbles then rise up as can be seen in figure 6.5. Such images strongly suggest that the observed bubbles form a real cluster and we do not observe a superposition of different bubbles produced during different fork cycles. In He II the situation is different in that the bubbles do not tear off from the fork surface up to the highest attainable drive.

The velocity of the fork versus the driving force is plotted in figure 6.6. The fork moves fast enough to create the turbulent regime of flow past it, where the drag force F_D depends more or less quadratically on the velocity, $F = F_D \sim v^2$; see the cases without cavitation in figure 6.6. When cavitation occurs, the data points lie below this dependence because creation of bubbles consumes energy – this can be qualitatively interpreted as an additional braking force F_b – the difference between the applied drive force and the force, which would be needed

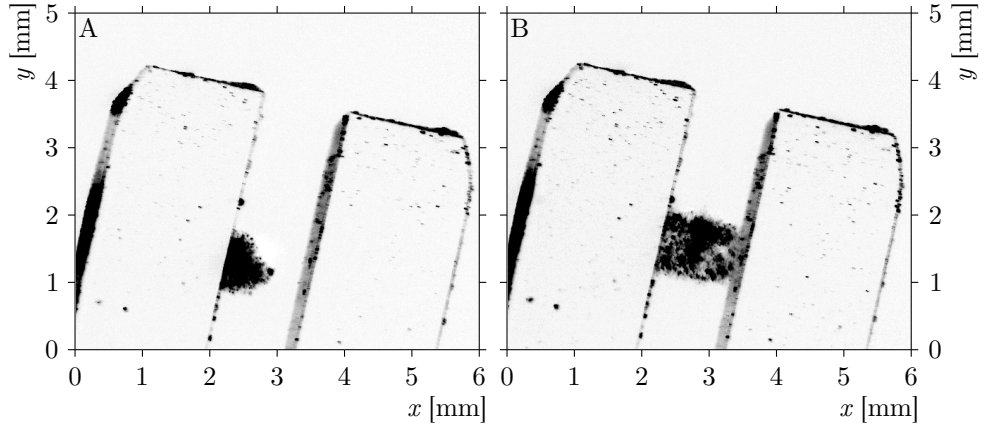


Figure 6.3: Fork under the same drive $129 V_{\text{rms}}$ in **A**: He II, rms velocity of the fork tips 576 mm/s, and **B** in He I, rms velocity 528 mm/s.

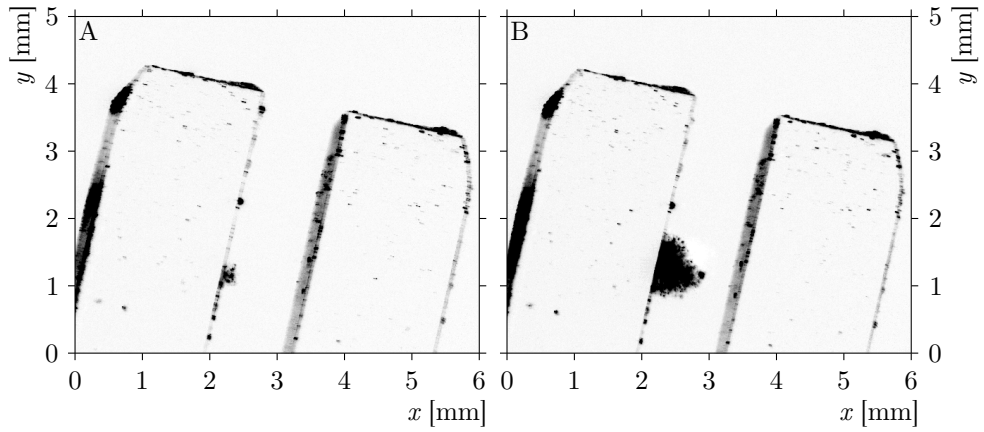


Figure 6.4: Images of the fork at the same bulk temperature 2.17 K, i. e. in He II, but under different drives: **A** $36.9 V_{\text{rms}}$, rms fork tip velocity 309 mm/s; **B**, $129 V_{\text{rms}}$, 576 mm/s.

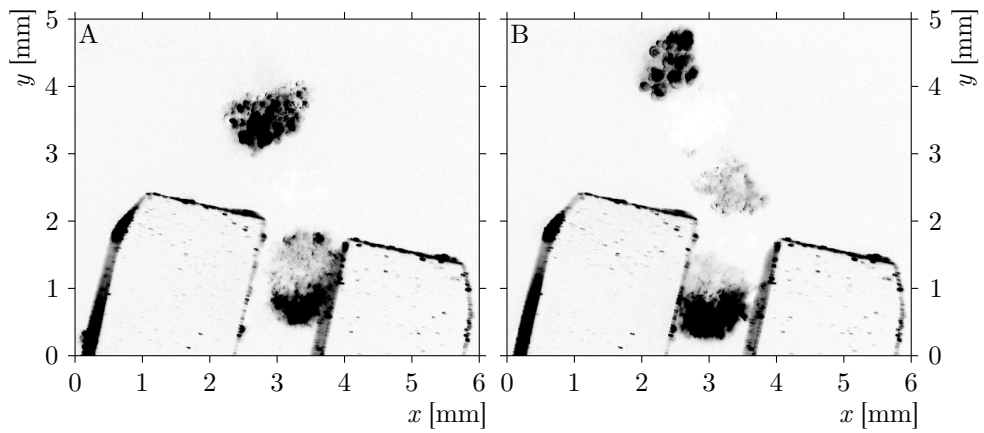


Figure 6.5: In He I at highest drives the bubbles live longer than one fork cycle, these bubbles then rise up. The **B** frame follows 10 ms after the **A** frame.

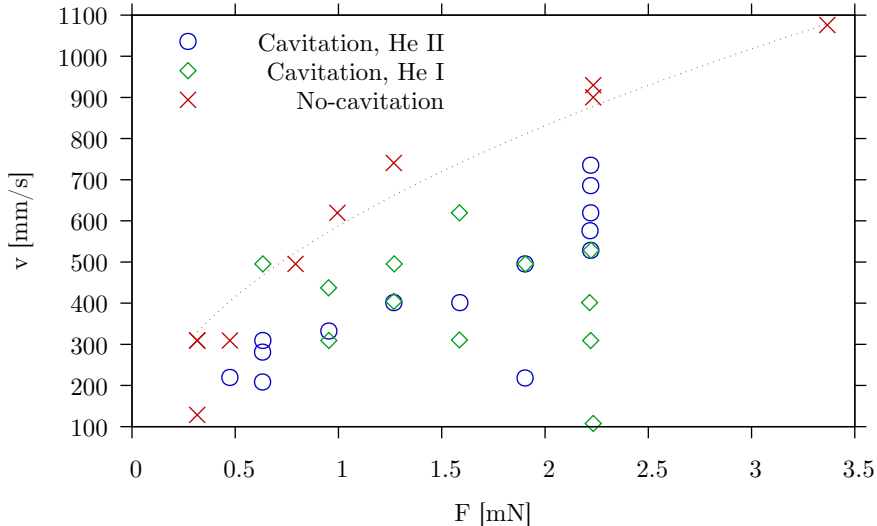


Figure 6.6: Measured velocity of prongs plotted versus applied force. The cases when the cavitation did not occur (represented by red crosses) *approximately* follow the expected dependence $F_D \sim v^2$ (plotted as a dotted line) valid for the turbulent regime.

to get to the same velocity under the action of hydrodynamic drag force only, i. e., $F_b = F - Cv^2$, where the prefactor $C \approx 2.9 \cdot 10^{-3} \text{Ns}^2\text{m}^{-2}$ is the fitting parameter using the data of figure 6.6. Note in passing that in He II the maximum energy losses can be carried away to the bulk by thermal counterflow of typical counterflow velocity up to a fraction of mm/s, i. e., much lower than the velocity of moving prongs.

We attempt to quantify the observed bubbles or clusters of bubbles by measuring their area A on each frame (simply by counting the pixels brighter than a chosen threshold). This leads to an effective radius r_{eff} , which the bubble would have assuming its semispherical shape:

$$r_{\text{eff}} = \sqrt{\frac{2A}{\pi}}. \quad (6.1)$$

The effective radius of the bubble (or cluster of bubbles) is plotted versus the additional braking force in figure 6.7. Although there is a visible correlation, the points are too scattered to discern any functional dependence. On the other hand, the reported difference in cavitation properties in He I and in He II is clearly visible: a fixed size bubble produces higher braking force in He II than in He I. The reason of this difference is unclear but might be connected either with the slightly larger surface tension of He II [5] or with quantized vortices attached to cavitation bubbles.

6.4 Conclusion

By using the fast optical camera we have directly observed heterogeneous cavitation in flow of He I and He II due to oscillating quartz fork, on both sides of the λ -transition. Typically a cluster of small bubbles is produced rather than one bigger hemispherical bubble, the position, size and shape of such a cluster

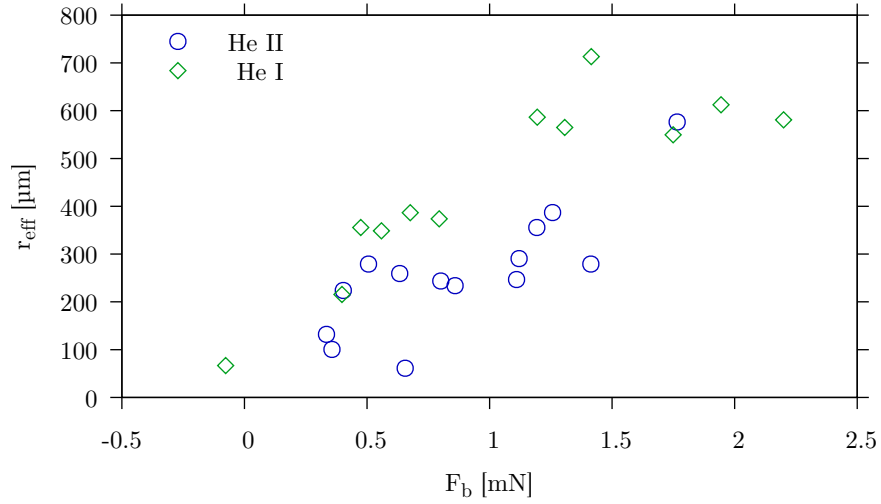


Figure 6.7: Effective radius r_{eff} of observed cavitation bubbles as a function of the added braking force F_b , evaluated as explained in the text.

changes from frame to frame. The produced bubbles are at first look similar in He I and in He II, however, cavitation threshold is lower in He I than in He II. Once nucleated, bubbles live longer in He I than in He II and can rise up in the bulk from the place of their nucleation. Additionally, under otherwise identical conditions the nucleated bubbles brake the motion of the fork's prongs more in He II than in He I.

Chapter 7

Small-scale similarity in quantum turbulence

In this chapter we use the experimental data recorded when studying the oscillatory flows of normal and superfluid helium together with the data relevant to our visualization studies of thermal counterflow and analyze them in order to investigate the idea of small-scale similarity in quantum turbulence. We do not describe in any detail the history of measurements performed in thermal counterflow; the reader is directed to the published paper [54] which the author of the thesis coauthored and the reprint of which is for convenience attached to this Thesis.

7.1 Introduction

The interpretation of our visualization results (chapter 4, article [126]) led to the conclusion that, at length scales larger than the *quantum length-scale* ℓ_q of the probed flow, defined as the intervortex distance, turbulent He II behaves as if it were a viscous fluid, while its quantum nature becomes apparent at smaller scales. More precisely, in thermal counterflow, the velocity and acceleration distributions of small particles suspended in the liquid have, at large enough scales, classical-like shapes, while, at scales smaller than ℓ_q , they are characterized by power-law tails emerging from the quantum description of He II [127, 128], similarly as in another quantum system – the cold atomic Bose-Einstein condensate [20, 129, 130].

We investigate experimentally, by visualization, the flow-induced dynamics of relatively small particles of solid deuterium or hydrogen in thermally and mechanically driven flows of He II, which appear distinctly different at scales larger than ℓ_q . Still, if the *probed length-scale* d (to be defined later) is smaller than ℓ_q , we find that the tails of the particle velocity distributions (which indicate the occurrence of rare events of large magnitude) are nearly identical, in the range of investigated parameters. Our experimental result therefore supports the long-held expectation that, at small enough length-scales, the dynamics of quantized vortices does not depend on the type of imposed large-scale flow. Additionally, this property of quantum turbulence can be seen as analogous to the small-scale universality observed in classical turbulent flows of viscous fluids, see for example [131], [132], [133] or [134] as it emerges from the pioneering work of Kolmogorov [17, 18].

7.2 Experimental setup

The experimental setup and methods of data analysis are already described in chapter 2. The oscillating obstacle has been described in chapter 4, including the results and a discussion of the observed quantum features. On the other hand, the *thermal counterflow*, to which we compare, is not a subject of this Thesis, although it was subject of the author's Diploma thesis [22]. Therefore, the counterflow measurement needs to be introduced.

It is performed in a vertical glass channel of square cross section, of 25 mm sides, and 100 mm long, a flat square heater is placed on the channel bottom to generate the flow in the vertical direction. The heater is a meander of resistive Pb wire in a thin kapton layer. The heater is driven by applying DC voltage and the actual power is measured by the 4-point method, as the quite long and thin wires have non negligible resistance. Thermal counterflow movies are recorded at camera frequency $f_{\text{cam}} = 400$ Hz, while oscillating obstacle movies are obtained at $f_{\text{cam}} = 100$ Hz. An example of thermal counterflow movie is on the attached CD.

The strength of thermally driven counterflow is quantified by the counterflow velocity [135]

$$v_{\text{ns}} = v_n - v_s = \frac{q}{\rho ST} \left(1 + \frac{\rho_n}{\rho_s} \right) = \frac{q}{\rho_s ST}, \quad (7.1)$$

where v_n and v_s indicate the normal fluid and superfluid velocities, respectively; once the heater is switched on, the superfluid component moves toward the heat source and the normal component flows away from it [136], in order to conserve the null mass flow rate (we assume here that $v_n > 0$ and $v_s < 0$). The total density ρ of the fluid, defined as the sum of the densities of its normal (ρ_n) and superfluid (ρ_s) components, depends weakly on temperature, while the densities ρ_n and ρ_s display much stronger temperature dependencies [5] (He II can be often considered entirely superfluid at temperatures below 1 K); q is the applied heat flux, S denotes the entropy per unit mass, tabulated, together with other fluid properties, in [5], and T indicates the temperature. We might emphasize that the phenomenon of *thermal counterflow* takes place only in He II; it is a pure quantum type of thermal convection which has no classical analogue [89].

7.3 Length-scales

7.3.1 Probed length-scale

The probed length-scale d in our experiment we define as the mean distance traveled by the particle between two consecutive frames, as it is done in the chapter 4. Let's note that it could be also the mean particle size, when this is larger than the former value, as it is introduced in [54].

In the case of the thermal counterflow experiments, we set $d = v_{\text{abs}}t$, where v_{abs} denotes the average particle velocity, obtained at the smallest time between particle positions, and t indicates the time step between two consecutive particle positions ($t = 1/f_{\text{cam}} = 2.5$ ms), used for the calculation of the velocities [105, 66], see the equation 2.11. Therefore we can calculate the velocity distribution at different length-scales d by using data of one movie only simply by changing this

time step t in the multiples of the smallest time corresponding to the camera frame rate used for video recording.

For the oscillating obstacle flows, we set the length-scale d probed by the particles equal to $2\pi fAt$, where f is the obstacle motion frequency, A is its amplitude and $t = 1/f_{\text{cam}} = 10$ ms as already introduced in the chapter 4. In this case we do not need to artificially increase the probed length-scale as just described above, because we have got several movies at different experimental conditions (f and A) covering length-scales smaller and larger than the *quantum length-scale* ℓ_q characterizing the investigated flow.

7.3.2 Flow length-scale

We define the ratio $R = d/\ell_q$ between the length scale probed by the particles and the quantum length scale of the investigated flow (that is, the average distance between quantized vortices). The corresponding ℓ_q for the counterflow data is computed as detailed in article [66] by using relevant published data [48]. More precisely, in the present conditions, i. e., at large enough heat fluxes, the imposed counterflow generates a tangle of vortex line density $L \approx \gamma^2(T) v_n s^2$, where the parameter $\gamma(T)$ is known with sufficient accuracy (of about 30%, see, e. g., [35] and references therein). We therefore experimentally select the quantum length scale $\ell_q \approx 1/\sqrt{L}$, by tuning the heat flux q , and we use the values of $\gamma(T)$ reported in [48] to estimate the average distance ℓ_q between quantized vortices.

In order to estimate the corresponding ℓ_q in the oscillating obstacle experiment we make a few additional assumptions and, as a first step, on the basis of the results of the chapter 4, we take the definition of the Kolmogorov dissipative scale $\eta = (\nu^3/\epsilon)^{1/4}$ [17], where ν is the fluid kinematic viscosity and ϵ indicates the mean dissipation rate of the flow. The latter, in turbulent flows of viscous fluids, can be set equal to $\nu\omega^2$, where ω is the average flow vorticity, which is calculated from the spatial derivatives of the fluid velocity and can be seen as a measure of the flow strength; consider also that, at scales larger than (or of the order of) η , the related flow behavior is expected to be universal, see, e. g., [18, 134, 131, 137]. The following step is to assume that ω^2 is approximately equal to the ensemble average of the experimentally obtained parameter ϑ^2 , see section 2.10. We can now re-use the formula 4.12 (and now we identify ℓ_c with ℓ_q), i. e., we assume that, for the studied oscillating obstacle flows, the average distance ℓ_q between quantized vortices is approximately equal to the length-scale obtained by adequately applying the definition of the Kolmogorov length-scale to flows of He II.

For He I, which is a viscous fluid, ν is tabulated in [5]. The values of the effective kinematic viscosity of turbulent He II reported in the literature (see, for example, [100] and references therein) are, in the investigated range of temperatures, of the same order of magnitude of the kinematic viscosity value of He I just above T_λ , that is, $\nu = 1.66 \cdot 10^{-8}$ m²/s [5], which can also be expressed as $\kappa/6$ [69]. Hence, for the sake of simplicity and consistency with the chapter 4, in order to estimate from equation 4.12 ℓ_q for the oscillating cylinder data obtained in He II, we set $\nu = \kappa/6$.

More generally, the just given length-scale definitions are based on several assumptions, whose main justification is that they lead to positive comparisons

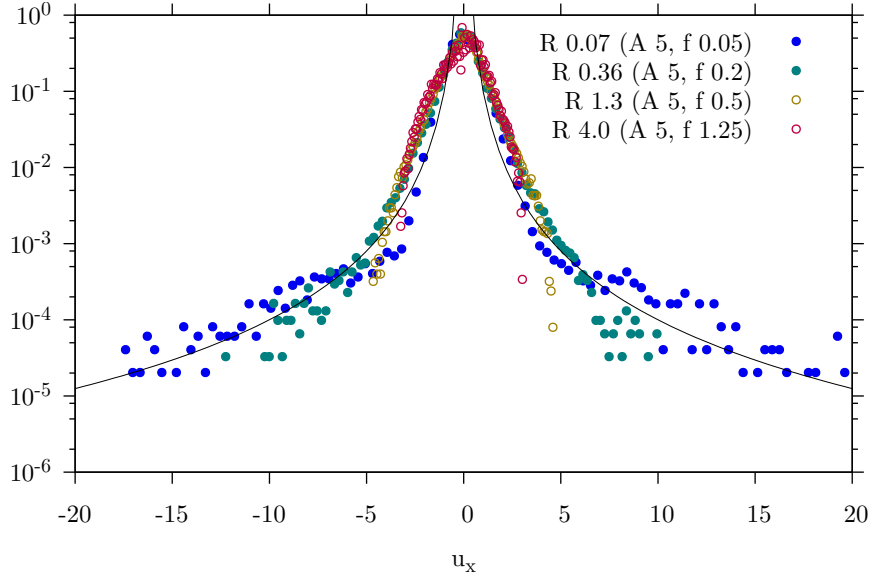


Figure 7.1: Probability density function (PDF) of the normalized horizontal velocity $u_x = (v_x - \langle v \rangle) / \sigma [v]$ of selected data sets of the oscillating obstacle experiment (compare with figure 4.12) with different values of the ratio R , A denotes the oscillation amplitude in mm, f is the frequency in Hz. The time step is $t = 10$ ms, all displayed data are from He II.

with experimental data, as shown below and in our publications [66, 126], the later also in chapter 4. However, the reader should not forget that they are indeed approximations, which are therefore not expected to capture entirely the physics of the problem.

7.4 Results

Our main result is shown in figure 7.1 and 7.2, where the probability density function (PDF) of the instantaneous horizontal component of particle velocity v_x normalized by its average and standard deviation, $u_x = (v_x - \langle v_x \rangle) / \sigma [v_x]$, is plotted. Here, $\langle v_x \rangle$ and $\sigma [v_x]$ indicate the mean value and the standard deviation of the particle horizontal velocity v_x , respectively (v_x is positive if directed from the left to the right of the field of view, toward the laser). The first figure 7.1 refers to the oscillating obstacle data, for more details about the conditions and results see chapter 4, and the second figure 7.2 contains the thermal counterflow data obtained far enough from the walls and the heater.

It is apparent that, at large particle velocities, both distributions, regardless of the type of flow, have the same power-law shape. To date, this feature was only observed by Paoletti et al. [138], in decaying counterflow, by us [64, 22], in steady-state counterflow, or in quantum turbulence in BEC by White et al. [129]. In the case of solid particles, whose motions are generally influenced by the quantized vortex tangle and by both velocity fields, the outcome can be justified by considering that particles trapped onto vortices can probe the occurrence of vortex reconnections [138, 139].

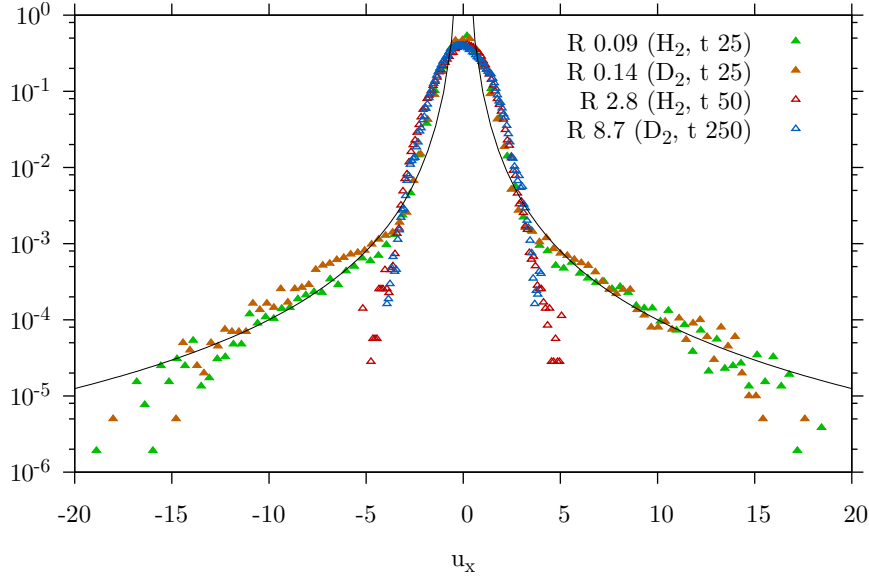


Figure 7.2: Probability density function (PDF) of the normalized horizontal velocity $u_x = (v_x - \langle v \rangle) / \sigma [v]$ of selected measurement of thermal counterflow obtained at a relative counterflow velocity of the normal and the superfluid component $v_{ns} = 6.8$ mm/s, t is the time step in ms, the first data set is obtained with hydrogen particles, the second with deuterium ones.

Note that the mechanically driven flows, at large enough scales, are expected to display features different from those observed in thermally driven flows [100]. This strongly suggests that, at length scales smaller than the quantum scale of the flow, particle motions are mainly influenced by quantized vortex dynamics.

The particle velocity distributions obtained from the oscillating obstacle experiment are clearly more scattered compared to those calculated from the counterflow experiments. This is likely due to the fact, that the total number of particle positions obtained in the former case is about one order of magnitude smaller than those corresponding to the latter one. That is caused by the lower seeding density in the former case, which has been decided to use in order to ensure correct trajectory connections as the spatial distribution of the velocity magnitude is strongly inhomogeneous. Nevertheless, the form of the oscillating obstacle distribution tails is consistent with the power-law shape expected in quantum flows, at small enough length-scales.

The result is reinforced by the observation that, at large R , the particle velocity distributions are nearly Gaussian, as observed in classical flows, see, for example, [134] and references therein, regardless of the imposed flow type.

This results are based on the statistical analysis of the particle velocities in the horizontal direction because the latter is perpendicular to the preferential direction of motion of the imposed flows. It is therefore easier to highlight our findings in the flow direction that, on average, is less influenced by the large-scale flow. However, interested reader can find also plots of the vertical velocity component distribution in the article [54] attached to this Thesis.

Figure 7.3 displays the distribution flatness, which is the 4th centered moment of the distribution calculated from the particle velocities as $F[v_x] = \langle (v_x - \langle v_x \rangle)^4 \rangle$.

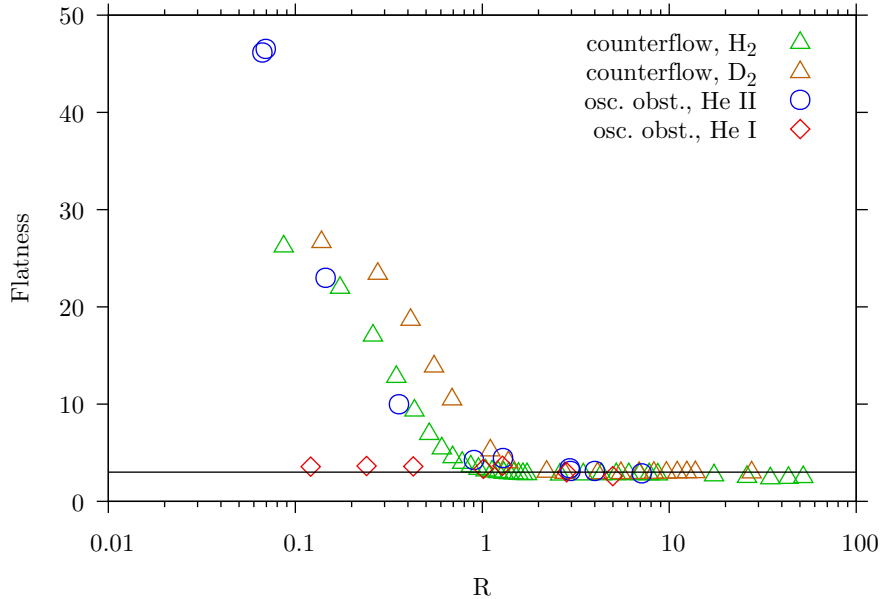


Figure 7.3: Flatness of the normalized horizontal velocity component $u_x = (v_x - \langle v \rangle) / \sigma[v]$ in dependence on the ratio R . Horizontal line corresponds to the flatness of Gaussian distribution. In the case of the counterflow data, the ratio R is changed artificially by increasing the time step t [66], while the different R in the oscillating obstacle data corresponds to different experimental conditions.

Flatness of a Gaussian distribution can be analytically calculated to be equal to 3, while it diverges for the $1/v^3$ distribution. Hence, when calculated numerically from the real obtained data, it depends on the large magnitude events, which are indeed rare, connected to the small-scales. Therefore, the flatness value of the power-law distribution has no sense itself, but it can be compared with values obtained at different R as shown in figure 7.3. We expect, however, that for large enough data sets (substantially larger than the present ones) the same (universal) flatness behavior should be observed at low R , when particle motions are influenced solely by the vortex tangle dynamics, as shown by the power-law form of the velocity distribution tails.

Nevertheless, the calculation of the velocity distribution flatness at various length scales can be useful to *estimate* the average intervortex distance – the quantum length-scale of the flow, if the latter is not already known. Such a scale should indeed be of the same order of the smallest scale at which the value of the distribution flatness becomes approximately equal to three, as seen in figure 7.3. In other words, visualization studies are capable of giving results that are usually obtained by other means, such as the second sound attenuation technique (see [140] or [141] and references therein). Additionally, as a consistency check, the flatness values calculated for the investigated oscillatory flows of He I do not appear to depend on R . The particle velocity distributions have quasi-Gaussian form at all scales, including those smaller than the dissipative scale η . To the best of our knowledge, this statistical property of classical turbulent flows has not been reported previously, likely due to the facts that (i) such small scales are difficult to probe experimentally in flows of viscous fluids, such as water or air, and that (ii) the flow behavior, at $d < \eta$, is not expected to be universal. However, this

result is not the focus of the present work and further investigations should be performed to address the issue in detail.

7.5 Conclusions of the chapter

Based on the analysis of the experimental data (both from thermal counterflow and from the flows due to oscillating objects) we have shown that, similarly as in classical (viscous) fluid turbulence, small-scale universality can be observed in quantum turbulence. Since postulated by Kolmogorov [17, 18], a large number of related studies has been performed in the field of classical turbulence, including the recent numerical investigations showing that small-scale universality holds already in various flows of moderate Reynolds number [131]. In viscous flows, however, the small scales are larger than the Kolmogorov length-scale η , below which the fluid motion is dissipated into heat by the action of the fluid viscosity, while in quantum flows the small scales are smaller than the average distance between quantized vortices, below which fluid motion may exist all the way down to the \AA scale – the size of the quantized vortex core. Additionally, in both cases, it is assumed that the flow small scales are appreciably smaller than the large scales of the flow, which are of the order of the experimental volume size.

In other words, the small-scale universality we observe can be seen as analogous to that reported to occur in viscous flows, but has also different features, as, to date, it is yet to be clarified how the Kolmogorov length-scale can be unequivocally linked to the average distance between quantized vortices, although it appears that, in most cases, flows of He II at scales larger than the quantum length-scale of the flow behave similarly to viscous flows at scales larger than η .

If, at scales larger than the average distance between quantized vortices, but still noticeably smaller than the flow large scales, universal features of quantum flows were observed, it would be possible to claim that the quantum length-scale of the flow might indeed be the quantum analogue of the Kolmogorov length-scale, and the latter could be possibly achieved by performing dedicated experiments, e. g., by collecting data sets larger than those currently available. Nevertheless, our statistical study of the motions of small particles in mechanically and thermally generated quantum flows of superfluid ^4He strongly suggests that the concept of small-scale universality is a fruitful one for the deeper understanding of the phenomenon of fluid turbulence in general.

Chapter 8

Conclusion

The Thesis represents a systematic study of various oscillatory flows of liquid helium performed in the Prague Visualization Laboratory - the first European laboratory capable of visualizing cryogenic flows of both classical viscous He I and superfluid He II using the methods of particle image velocimetry (PIV) and particle tracking velocimetry (PTV) utilizing micrometer-sized seeding particles of frozen hydrogen and deuterium. In order to keep the Thesis self contained and comprehensive, the author decided to restrict its content to mechanically generated oscillatory flows of cryogenic helium and to a detailed comparison of classical and quantum cases, which is at the same time, the topic of the author's the 3-year GAUK (Grantová Agentura Univerzity Karlovy) project number 1968214 *Studium oscilačních proudění a kavitace v kapalném héliu vizualizačními metodami*. Additionally, the author contributed to studies of the acceleration of small particles in quantum turbulence as well as visualization studies of steady counterflows past a circular cylinder. He is a coauthor of several papers published in impacted scientific journals - Physical Review B, Journal of Fluid Mechanics: Rapid communication and Journal of Low Temperature Physics, see the List of Publications and selected reprints attended to this Thesis.

The main results described in this Thesis can be characterized as follows:

1. We have observed that, in the case of mechanically driven coflow of He II, macroscopic vortical structures form in the wake of an oscillating obstacle of the shape of a prism. These structures are similar to those observed in He I, which is a classical viscous liquid. Their size is of the order of the obstacle size and, additionally, their structure exhibits a turbulent vortex core with an inviscid envelope, similar as in classical liquids [97]. (Chapter 4)
2. The author has introduced the PTV based pseudovorticity, a useful approximation of vorticity calculated from the particle trajectory data, which on one hand, highlights the classical-like vortical structures and, on the other hand, it shows different scaling with the Reynolds number, which is dependent on the ratio of the characteristic lengths probed by the PTV visualization and the characteristic small length-scales of classical and quantum flows, i. e. the Kolmogorov length η and the quantum length scale – the intervortex distance ℓ . (Chapter 4)

3. We have observed the *viscous streaming* (a well known flow in classical hydrodynamics usually connected with the Reynolds stresses and the curvature of the stream) generated in both He I and He II by a vibrating quartz tuning fork, which is a widely used tool for studying quantum turbulence. We have observed streaming cells of the order of the fork prong size situated between the corner axes and the side axes; according to their orientation, we have identified them as *outer streaming cells*, which are classically explained via viscous induction. (Chapter 5)
4. We have observed cavitation near an oscillating quartz tuning fork in He I and in He II just below the λ -transition, confirming previous results which show the critical cavitation velocity at the λ -transition steeply increases. The new result is that this heterogeneous cavitation produces a cluster of small bubbles and that these bubbles brake the fork motion more in He II than in He I. (Chapter 6)
5. We have found that in all studied quantum flows of He II, the statistical distribution of velocity exhibits a strong dependence on the ratio between the length-scale probed by the particles, and the flow characteristic length-scale, which is the Kolmogorov length in He I or the quantum length scale – the mean intervortex distance in He II. When the experimentally probed length-scale is smaller than the intervortex distance, the probability density distributions of turbulent velocity contain power-law tails, regardless of the type of large scale mean flow imposed, suggesting small scale similarity in quantum turbulence. At larger probed length-scales, as well as in He I, we have observed classical Gaussian-like distributions. (Chapter 7)

To summarize, the Thesis contributes to the general notion that superfluid He II, which is a quantum liquid, behaves as a classical viscous liquid at length-scales larger than the quantum length scale – mean intervortex distance – when the individual quantized vortices can be considered as a continuum, while at smaller length-scales, the quantum nature of such turbulence emerges, both in thermally and mechanically driven flows. It is shown that both these regimes are experimentally accessible and can be studied by visualizing suitable tracer particles, although the details of their interaction with the normal and superfluid components of He II are still poorly understood.

8.1 List of publications

Publications marked with * are reprinted in the attachment.

1. M. La Mantia, D. Duda, M. Rotter, and L. Skrbek. Lagrangian accelerations of particles in superfluid turbulence, *Journal of Fluid Mechanics*, **717** R9, DOI: 10.1017/jfm.2013.31, 2013.
2. M. La Mantia, D. Duda, M. Rotter, and L. Skrbek. Lagrangian velocity distributions in thermal counterflow of superfluid He-4. *Proc. of Conf. on Experimental Fluid Mechanics (EFM 12)*, Hradec Králové, NOV 20-23 2012, Book Series: *EPJ Web of Conferences*, 45, Article Number UNSP 01005, DOI: 10.1051/epj-conf/20134501005, 2013.

3. * M. La Mantia, D. Duda, M. Rotter, and L. Skrbek. On the Visualization of Thermal Counterflow of He II Past a Circular Cylinder. *Journal of Low Temp. Physics*, **175** No1/2 331-338, DOI: 10.1007/s10909-013-0961-z, 2014.
4. M. La Mantia, D. Duda, M. Rotter, and L. Skrbek. Vizualizace obtékání oscilující překážky supratekutým héliem. *Proceedings of the 28th Symposium on Anemometry* (Edited by Z. Chára and L. Klaboch, Institute of Hydrodynamics of the Academy of Sciences of the Czech Republic, Prague), pp. 7-13, ISBN 978-80-87117-11-8, 2014.
5. D. Duda, M. La Mantia, and L. Skrbek. Automated Data Processing in Superfluid Flow Visualization. *WDS'14 Proceedings of Contributed Papers - Physics* (MATFYZPRESS), pp. 73-78, ISBN 978-80-7378-276-4, 2014.
6. * D. Duda, P. Švančara, M. La Mantia, M. Rotter, and L. Skrbek. Visualization of viscous and quantum flows of liquid ^4He due to an oscillating cylinder of rectangular cross section. *Phys. Rev. B* **92**, 064519, DOI: 10.1103/PhysRevB.92.064519, 2015.
7. D. Duda, P. Švančara, M. La Mantia, M. Rotter, and L. Skrbek. Makroskopické víry v supratekutém héliu. *Proceedings of the 29th Symposium on Anemometry* (Edited by Z. Chára and L. Klaboch, Institute of Hydrodynamics of the Academy of Sciences of the Czech Republic, Prague), pp. 7-13, ISBN: 978-80-87117-13-2, 2015.
8. * M. La Mantia, P. Švančara, D. Duda, and L. Skrbek. Small-scale universality of particle dynamics in quantum turbulence. *Phys. Rev. B*, **94**, 184512, DOI: 10.1103/PhysRevB.94.184512, 2016.
9. D. Duda, P. Švančara, M. La Mantia, D. Schmoranzer, and L. Skrbek. Pozorování kavitačních bublin v kapalném héliu. *30th Symposium on Anemometry – proceedings* (Edited by Z. Chára and L. Klaboch, Institute of Hydrodynamics of the Academy of Sciences of the Czech Republic, Prague), pp. 7-14, ISBN: 978-80-87117-14-9, 2016.
10. * D. Duda, P. Švančara, M. La Mantia, M. Rotter, D. Schmoranzer, O. Kolosov, and L. Skrbek. Cavitation bubbles generated by vibrating quartz tuning fork in liquid ^4He close to the λ -transition. *J. Low Temp. Phys.*, **187** pp. 376-382, DOI: 10.1007/s10909-016-1684-8, 2017.
11. D. Duda, M. La Mantia, and L. Skrbek. Visualization of Large-Scale Flow Due to an Oscillating Tuning Fork in Normal and Superfluid Helium. *Proceedings Topical Problems of Fluid Mechanics 2017* (Edited by David Šimurda and Tomáš Bodnár, Prague), pp. 103-112, ISBN: 978-80-87012-61-1 (Print), DOI: 10.14311/TPFM.2017.014, 2017
12. * D. Duda, P. Švančara, P. Hrubcová, M. La Mantia, and L. Skrbek. Experimentální studium stacionárního pohybu částic v supratekutém héliu v okolí rychle kmitající překážky – vliv velikosti oblasti. *Proceedings of the 31th Symposium on Anemometry* (Edited by Z. Chára and L. Klaboch, Institute of Hydrodynamics of the Academy of Sciences of the Czech Republic, Prague), pp. 7-13, ISBN:978-80-87117-16-3, 2017.
13. * D. Duda, M. La Mantia, and L. Skrbek, Streaming flow due to a quartz tuning fork oscillating in normal and superfluid ^4He . *Phys. Rev. B*, 2017, in print

8.2 List of conference presentations

The presentations given by the author in the oral or poster (marked) form.

1. (poster) D. Duda, M. La Mantia, M. Rotter, Ladislav Skrbek, Dynamics of solid D_2 particles in quantum turbulence generated in thermal counterflow, Experimental Fluid Mechanics, Kutná Hora (2013)
2. D. Duda, M. La Mantia, and L. Skrbek, On automatized data processing in superfluid flow visualization, Week of Doctoral Students, MFF UK, Praha (2014)
3. Duda, La Mantia, Rotter, Skrbek, Visualization of selected quantum flows of superfluid helium 4, 7th European Postgraduate Fluid Dynamics Conference, Ilmenau, (2014)
4. (poster) D. Duda, M. La Mantia, M. Rotter and L. Skrbek, Dynamics of solid D_2 particles in quantum turbulence generated in thermal counterflow, Experimental Fluid Mechanics, Český Krumlov (2014)
5. Duda, Švančara, La Mantia, Skrbek, Visualization of the flow in the proximity of a rectangular cylinder oscillating in superfluid ^4He , Colloquium Fluid Dynamics, AV ČR, Praha (2014)
6. D. Duda, P. Švančara, M. La Mantia, M. Rotter, L. Skrbek, Makroskopické víry v supratekutém héliu, 29th Symposium on Anemometry, Litice (2015)
7. D. Duda, P. Švančara, M. La Mantia, M. Rotter, L. Skrbek, Liquid helium flows around an oscillating cylinder, 15th European Turbulence Conference 2015, Delft (2015)
8. D. Duda, M. La Mantia, P. Švančara, M. Rotter, L. Skrbek, Liquid helium flow visualization in Prague, EuHIT Cryogenic Turbulence Workshop, Grenoble (2015)
9. D. Duda, P. Švančara, M. La Mantia, D. Schmoranzer, L. Skrbek, Pozorování kavitačních bublin v kapalném héliu, 30th Symposium on Anemometry, Litice (2016)
10. (poster) D. Duda, P. Švančara, M. La Mantia, M. Rotter, D. Schmoranzer, L. Skrbek, Cavitation bubbles in liquid ^4He close to the λ -transition, Quantum Fluids and Solids 2016, Praha (2016)
11. D. Duda, P. Švančara, M. La Mantia, M. Rotter, D. Schmoranzer, L. Skrbek, Visualization of cavitation bubbles in liquid ^4He , 11th European Fluid Mechanics Conference, Sevilla (2016)
12. D. Duda, M. La Mantia, L. Skrbek, Visualization of Large-Scale Flow due to an Oscillating Tuning Fork in Normal and Superfluid Helium, Topical Problems of Fluid Mechanics 2017, Praha (2017)
13. D. Duda, P. Švančara, P. Hrubcová, M. La Mantia a L. Skrbek, Experimentální studium stacionárního pohybu částic v supratekutém héliu v okolí rychle kmitající překážky – vliv velikosti oblasti, 31th Symposium on Anemometry, Litice (2017)
14. D. Duda, P. Švančara, P. Hrubcová, M. La Mantia, M. Rotter and L. Skrbek, Visualization of oscillatory flows in He II, Workshop Measurement Methods in Turbulence, Grenoble (2017)

Bibliography

- [1] K. Lodders. Solar system abundances and condensation temperatures of the elements. *Astrophys. J.*, 591:1220–1247, 2003.
- [2] Y. I. Izotov, T. X. Thuan, and V. A. Lipovetsky. The primordial helium abundance: systematic effects and a new determination. *Astrophys. J. Suppl. S.*, 108:1–39, 1997.
- [3] R. Wieler. *Noble Gases in Geochemistry and Cosmochemistry*, volume 21. Geochemical Soc. America, 2002.
- [4] W. M. White. Helium not in store. *Nature*, 436:1095, 2005.
- [5] R. J. Donnelly and C. F. Barenghi. The Observed Properties of Liquid Helium at the Saturated Vapor Pressure. *J. Phys. Chem. Ref. Data*, 27:1217–1274, 1998.
- [6] Bureau International des Poids et Mesures. *Échelle internationale de température de 1990*. BIPM, 1989.
- [7] P. Skyba. *Superfluid ^3He as a model system for cosmology - Experimental point of view*, volume 718 of *Lect. Notes Phys.* Springer-Verlag, 2007.
- [8] C. F. Barenghi, V. S. L'vov, and P. E. Roche. Experimental, numerical, and analytical velocity spectra in turbulent quantum fluid. *P. Natl. Acad. Sci. USA*, 111:4683–4690, 2014.
- [9] P. J. Mohr, D. B. Newell, and B. N. Taylor. Codata recommended values of the fundamental physical constants: 2014. *Rev. Mod. Phys.*, 88(3), 2016.
- [10] T. Brauner, A. Feher, M. Grajcar, J. Hošek, Z. Janů, M. Jirsa, J. Kuriplach, J. Nyeki, M. Rotter, P. Samuely, B. Sedlák, L. Skrbek, P. Skyba, and P. Středa. *Fyzika nízkých teplot I + II*. Matfyzpress, 2011.
- [11] L. Pitaevskii and S. Stringari. *Bose-Einstein condensation*, volume 116 of *International series on monographs on physics*. Oxford Univ Press, 2003.
- [12] N. G. Berloff, M. Brachet, and N. P. Proukakis. Modeling quantum fluid dynamics at nonzero temperatures. *P. Natl. Acad. Sci. USA*, 111:4675–4682, 2014.
- [13] N. Berloff. Nonlocal nonlinear schrodinger equations as models of superfluidity. *J. Low Temp. Phys.*, 116(5-6):1–22, 1999.
- [14] F. Dalfovo. Structure of vortices in helium at zero temperature. *Phys. Rev. B*, 46(9):5482–5488, 1992.
- [15] A. Ghosh and H. J. Maris. Observation of new type of electron bubble in superfluid helium. *Phys. Rev. Lett.*, 95(26):265301, 2005.

- [16] N. P. Proukakis and B. Jackson. Finite temperature models of bose-einstein condensation. *J Phys B*, 41(20):203002, 2008.
- [17] A. N. Kolmogorov. The local structure of turbulence in incompressible viscous fluid for very large reynolds numbers. *Dokl. Akad. Nauk. SSSR*, 30:299, 1941.
- [18] A. N. Kolmogorov. Dissipation of energy in the locally isotropic turbulence. *Dokl. Akad. Nauk. SSSR*, 32:19, 1941.
- [19] L. Skrbek and K. R. Sreenivasan. Developed quantum turbulence and its decay. *Phys. Fluids*, 24(1), 2012.
- [20] A. C. White, B. P. Anderson, and V. S. Bagnato. Vortices and turbulence in trapped atomic condensates. *P. Natl. Acad. Sci. USA*, 111:4719–4726, 2014.
- [21] D. V. Osborne. The rotation of liquid helium ii. *Proc. Phys. Soc. A*, 63:909, 1950.
- [22] D. Duda. *Visualization of selected flows of superfluid helium using solid hydrogen tracer particles*. Faculty of Mathematics and Physics, Charles University, 2013.
- [23] R. Hänninen and A. W. Baggaley. Vortex filament method as a tool for computational visualization of quantum turbulence. *P. Natl. Acad. Sci. USA*, 111:4667–4674, 2014.
- [24] K. W. Schwartz. Three-dimensional vortex dynamics in superfluid ^4He : Line-line and line-boundary interactions. *Phys. Rev. B*, 31(9):5782–5804, 1985.
- [25] P. G. Saffman. *Vortex Dynamics*. Oxford University Press, 1992.
- [26] E. Varga. Spontaneous emergence of large vortical structures in 2d numerical simulations of superfluid turbulence. *28th Symposium on Anemometry*, 28, 2014.
- [27] D. Kivotides, C. J. Vassilicos, D. C. Samuels, and C. F. Barenghi. Velocity spectra of superfluid turbulence. *Europhys. Lett.*, 57:845–851, 2002.
- [28] V. S. L’vov and A. Pomyalov. Statistics of quantum turbulence in superfluid he. *J. Low Temp. Phys.*, 187(5-6):497–514, 2017.
- [29] V. S. L’vov, S. V. Nazarenko, and O. Rudenko. Bottleneck crossover between classical and quantum superfluid turbulence. *Phys. Rev. B*, 76(2), 2007.
- [30] A. W. Baggaley, J. Laurie, and C. F. Barenghi. Vortex-density fluctuations, energy spectra, and vortical regions in superfluid turbulence. *Phys. Rev. Lett.*, 109(20), 2012.
- [31] P. Walmsley, D. Zmeev, F. Pakpour, and A. Golov. Dynamics of quantum turbulence of different spectra. *P. Natl. Acad. Sci. USA*, 111:4691–4698, 2014.
- [32] S. N. Fisher, M. J. Jackson, Y. A. Sergeev, and V. Tsepelin. Andreev reflection, a tool to investigate vortex dynamics and quantum turbulence in $^3\text{He-B}$. *P. Natl. Acad. Sci. USA*, 111:4659–4666, 2014.
- [33] V. Tsepelin, A. Baggaley, Y. Sergeev, C. Barenghi, S. Fisher, G. Pickett, M. Jackson, and N. Suramlshvili. Visualization of quantum turbulence in superfluid $^3\text{He-B}$: Combined numerical/experimental study of andreev reflection. *ArXiv*, cond-mat(1706.01791), 2017.

- [34] C. F. Barenghi, L. Skrbek, and K. R. Sreenivasan. Introduction to quantum turbulence. *P. Natl. Acad. Sci. USA*, 111:4647–4652, 2014.
- [35] S. Babuin, M. Stammeier, E. Varga, M. Rotter, and L. Skrbek. Quantum turbulence of bellows-driven 4he superflow: Steady state. *Phys. Rev. B*, 86(134515), 2012.
- [36] P. Roche, C. F. Barenghi, and E. Leveque. Quantum turbulence at finite temperature: The two-fluids cascade. *Europhys. Lett.*, 87(5), 2009.
- [37] C. F. Barenghi, Y. A. Sergeev, and A. W. Baggaley. Regimes of turbulence without an energy cascade. *Scientific Reports*, 6, 2016.
- [38] R. H. Kraichnan. Inertial ranges in two-dimensional turbulence. *Phys. Fluids*, 10(7):1417–1423, 1967.
- [39] A. P. Ingersoll. Atmospheric dynamics of the outer planets. *Science*, 248(4953):308–315, 1990.
- [40] S. Cabanes, J. Aurnou, B. Favier, and M. Le Bars. A laboratory model for deep-seated jets on the gas giants. *Nat. Phys.*, 13(4):387–390, 2017.
- [41] P. K. Yeung. Lagrangian investigations of turbulence. *Annu Rev. Fluid Mech.*, 34:115–142, 2002.
- [42] E. Lévêque and A. Nasso. Introduction of longitudinal and transverse lagrangian velocity increments in homogenous and isotropic turbulence. *Europhys. Lett.*, 108:54004, 2014.
- [43] K. Chong, S. D. Kelly, S. Smith, and J. D. Eldredge. Inertial particle trapping in viscous streaming. *Phys. Fluids*, 25(3):033602, 2013.
- [44] M. R. Maxey and J. J. Riley. Equation of motion for a small rigid sphere in a nonuniform flow. *Phys. Fluids*, 26(4):883–889, 1983.
- [45] M. La Mantia and P. Dabnichki. Added mass effect on flapping foil. *Eng. Anal. Bound. Elem.*, 36(4):579–590, 2012.
- [46] V. Uruba. private communication.
- [47] W. Guo, M. La Mantia, D. P. Lathrop, and S. W. Van Sciver. Visualization of two-fluid flows of superfluid helium-4. *P. Natl. Acad. Sci. USA*, 111:4653–4658, 2014.
- [48] Y. A. Sergeev, C. F. Barenghi, and D. Kivotides. Motion of micron-size particles in turbulent helium ii. *Phys. Rev. B*, 74(184506), 2006.
- [49] E. Fonda, D. P. Meichle, N. T. Ouellette, S. Hormoz, and D. P. Lathrop. Direct observation of kelvin waves excited by quantized vortex reconnection. *P. Natl. Acad. Sci. USA*, 111:4707–4710, 2014.
- [50] D. Duda, M. La Mantia, M. Rotter, and L. Skrbek. On the visualization of thermal counterflow of he ii past a circular cylinder. *J. Low Temp. Phys.*, 175(1-2):331–338, 2014.
- [51] Y. A. Sergeev and C. F. Barenghi. Particles-vortex interactions and flow visualization in 4he. *J. Low Temp. Phys.*, 157(5-6):429–475, 2009.

- [52] T. Zhang and S. W. Van Sciver. Large-scale turbulent flow around a cylinder in counterflow superfluid ^4He (^4He (ii)). *Nat. Phys.*, 1(1):36–38, 2005.
- [53] C. Soullaine, M. Quintard, B. Baudouy, and R. Van Weelder. Numerical investigation of thermal counterflow of ^4He past cylinders. *Phys. Rev. Lett.*, 118(074506), 2017.
- [54] M. La Mantia, P. Švančara, D. Duda, and L. Skrbek. Small-scale universality of particle dynamics in quantum turbulence. *Phys. Rev. B*, 94(18), 2016.
- [55] M. La Mantia, T. V. Chagovets, M. Rotter, and L. Skrbek. Testing the performance of a cryogenic visualization system on thermal counterflow by using hydrogen and deuterium solid tracers. *Rev. Sci. Instrum.*, 83(5), 2012.
- [56] Thompson A. and Taylor B. N. *Guide for the Use of the International System of Units (SI)*. National Institute of Standards and Technology, nist special publication 811, 2008 edition edition, 2008.
- [57] T. M. Flynn. *Cryogenic Engineering*. CRC Press, 2005.
- [58] S. C. Bates. *Compilation of the engineering properties of solid hydrogen*. Glastonbury, 2002.
- [59] M. Blažková, M. Človečko, V. B. Eltsov, E. Gažo, R. de Graaf, J. Hosio, M. Krusius, D. Schmoranzler, W. Schoepe, L. Skrbek, P. Skyba, R. E. Solntsev, and Vinen W.F. Vibrating Quartz Fork — A Tool for Cryogenic Helium Research. *J. Low Temp. Phys.*, 150:525, 2008.
- [60] R. Blaauwegeers, M. Blažková, M. Človečko, V. B. Eltsov, R. de Graaf, J. Hosio, M. Krusius, D. Schmoranzler, W. Schoepe, L. Skrbek, P. Skyba, R. E. Solntsev, and D. E. Zmeev. Quartz Tuning Fork: Thermometer, Pressure- and Viscometer for Helium Liquids. *J. Low Temp. Phys.*, 146:537, 2007.
- [61] D. I. Bradley, M. Človečko, S. N. Fisher, D. Garg, E. Guise, R. P. Haley, O. Kolosov, G. R. Pickett, V. Tsepelin, D. Schmoranzler, and L. Skrbek. Crossover from hydrodynamic to acoustic drag on quartz tuning forks in normal and superfluid ^4He . *Phys. Rev. B*, 85(014501), 2012.
- [62] J. Hodic. *Interakce laserového záření a stopovacích částic v kapalném heliu*. Faculty of Mathematics and Physics, Charles University, 2013.
- [63] I. F. Sbalzarini and P. Koumoutsakos. Feature point tracking and trajectory analysis for video imaging in cell biology. *J. struct. biol.*, 151(2):182–195, 2005.
- [64] M. La Mantia, D. Duda, M. Rotter, and L. Skrbek. Velocity statistics in quantum turbulence. In *Procedia IUTAM*, volume 9, pages 79–85, 2013.
- [65] I. Zurbenko. *The spectral analysis of time series*. North-Holland, 1986.
- [66] M. La Mantia and L. Skrbek. Quantum, or classical turbulence? *Europhys. Lett.*, 105(4), 2014.
- [67] C. N. Phan, M. Aureli, and M. Porfiri. Finite amplitude vibrations of cantilevers of rectangular cross sections in viscous fluids. *J. Fluid Struct.*, 40:52 – 69, 2013.
- [68] L. D. Landau and E. M. Lifshitz. *Hydrodynamics*. Pergamon Press, 2nd ed. edition, 1987.

- [69] V. S. L'vov, L. Skrbek, and K. R. Sreenivasan. Viscosity of liquid ^4He and quantum of circulation: Are they related? *Phys. Fluids*, 26(041703), 2014.
- [70] G. H. Keulegan and L. H. Carpenter. Forces on cylinders and plates in an oscillating fluid. *J. Res. Nat. Inst. Stand.*, 60(5):423–440, 1958.
- [71] N. Riley. Steady streaming. *Annu Rev. Fluid Mech.*, 19(118108), 2001.
- [72] J. T. Stuart. Double boundary layers in oscillatory viscous flow. *J. Fluid Mech.*, 24(4):673–687, 1966.
- [73] K. Chong, S. D. Kelly, S. T. Smith, and J. D. Eldredge. Transport of inertial particles by viscous streaming in arrays of oscillating probes. *Phys. Rev. E*, 93:013109, Jan 2016.
- [74] C. Y. Wang. On high-frequency oscillatory viscous flows. *J.f Fluid Mech.*, 32(1):55–68, 1968.
- [75] C. H. K. Williamson. Vortex dynamics in the cylinder wake. *Annu. Rev. Fluid Mech.*, 28:477–539, 1996.
- [76] M. Coutanceau and R. Bouard. Experimental determination of the main features of the viscous flow in the wake of a circular cylinder in uniform translation - 1. steady flow. *J. Fluid Mech.*, 79(pt 2):231–256, 1977.
- [77] R. D. Henderson. Details of the drag curve near the onset of vortex shedding. *Phys. Fluids*, 7(9):2102–2104, 1995.
- [78] C. H. K. Williamson. The natural and forced formation of spot-like vortex dislocations in the transition of a wake. *J. Fluid Mech.*, 243:393–441, 1992.
- [79] C. H. K. Williamson, J. Wu, and J. Sheridan. Scaling of streamwise vortices in wakes. *Phys. Fluids*, 7(10):2307–2309, 1995.
- [80] J. Lin, P. Vorobieff, and D. Rockwell. Three-dimensional patterns of streamwise vorticity in the turbulent near-wake of a cylinder. *J. Fluid Struct.*, 9(2):231–234, 1995.
- [81] G. Schewe. On the force fluctuations acting on a circular cylinder in crossflow from subcritical up to transcritical reynolds numbers. *J. Fluid Mech.*, 133:265–285, 1983.
- [82] P. W. Bearman. On vortex shedding from a circular cylinder in the critical reynolds number regime. *J. Fluid Mech.*, 37(3):577–585, 1969.
- [83] A. Roshko. Experiments on the flow past a circular cylinder at very high reynolds number. *J. Fluid Mech.*, 10(3):345–356, 1961.
- [84] P. W. Bearman. Vortex shedding from oscillating bluff bodies. *Annu. Rev. fluid mech.*, 16:195–222, 1984.
- [85] P. W. Bearman. Investigation of the flow behind a two-dimensional model with a blunt trailing edge and fitted with splitter plates. *J. Fluid Mech.*, 21(2):241–255, 1965.
- [86] S. Taneda and H. Honji. Unsteady flow past a flat plate normal to the direction of motion. *J. Phys. Soc. Jpn*, 30(1):262–272, 1971.

- [87] L. Tao and K. Thiagarajan. Low kc flow regimes of oscillating sharp edges i. vortex shedding observation. *Appl. Ocean Res.*, 25(1):21 – 35, 2003.
- [88] W. F. Vinen and L. Skrbek. Quantum turbulence generated by oscillating structures. *P. Natl. Acad. Sci. USA*, 111:4699–4706, 2014.
- [89] W. F. Vinen. An introduction to quantum turbulence. *Philos. T. Roy. Soc. A*, 366(1877):2925–2933, 2008.
- [90] D. Schmoranzler, M. Král’Ová, V. Pilcová, W. F. Vinen, and L. Skrbek. Experiments relating to the flow induced by a vibrating quartz tuning fork and similar structures in a classical fluid. *Phys. Rev. E*, 81(6), 2010.
- [91] E. Zemma and J. Luzuriaga. Anomalous trajectories of h_2 solid particles observed near a sphere oscillating in superfluid turbulent $4he$. *J. Low Temp. Phys.*, 173(1-2):71–79, 2013.
- [92] E. Zemma, M. Tsubota, and J. Luzuriaga. Possible visualization of a superfluid vortex loop attached to an oscillating beam. *J. Low Temp. Phys.*, 179(5-6):310–319, 2015.
- [93] T. V. Chagovets and S. W. Van Sciver. Visualization of $he\ ii$ forced flow around a cylinder. *Phys. Fluids*, 27(4):045111, 2015.
- [94] M. Murakami, T. Yamazaki, and M. Hanada. Flow visualization study on large-scale vortex ring in $he\ ii$. *Jpn. J. of Appl. Phys.*, 26(S3-1):107–108, 1987.
- [95] G. Stamm, F. Bielert, W. Fiszdon, and J. Piechna. Counterflow-induced macroscopic vortex rings in superfluid helium: visualization and numerical simulation. *Physica B*, 193(2):188–194, 1994.
- [96] D. Duda, M. La Mantia, and Skrbek L. Automated data processing in superfluid flow visualization. *WDS’14 Proceedings of Contributed Papers - Physics*, pages 73–78, 2014.
- [97] E. Amromin. Analysis of vortex core in steady turbulent flow. *Phys. Fluids*, 19(118108), 2007.
- [98] V. Uruba. *Turbulence*. Nakladatelství ČVUT, 2009.
- [99] T. Xu and S. W. Van Sciver. Particle image velocimetry measurements of the velocity profile in $he\ ii$ forced flow. *Phys. Fluids*, 19(7):071703, 2007.
- [100] E. Varga, S. Babuin, and L. Skrbek. Second-sound studies of coflow and counterflow of superfluid $4he$ in channels. *Phys. Fluids*, 27(6):065101, 2015.
- [101] T. V. Chagovets, A. V. Gordeev, and L. Skrbek. Effective kinematic viscosity of turbulent $he\ ii$. *Phys. Rev. E*, 76:027301, Aug 2007.
- [102] S. Babuin, E. Varga, L. Skrbek, E. Lévêque, and P. E. Roche. Effective viscosity in quantum turbulence: A steady-state approach. *Europhys. Lett.*, 106(2), May 2014.
- [103] M. Murakami, Hanada M., and T. Yamazaki. Flow visualization study on large-scale vortex ring in $he\ ii$. *Jpn. J. Appl. Phys.*, 26:107, 1987.

- [104] G. Stamm, F. Bielert, W. Fiszdon, and J. Piechna. Counterflow-induced macroscopic vortex rings in superfluid helium: visualization and numerical simulation. *Physica B*, 193(2):188 – 194, 1994.
- [105] M. La Mantia and L. Skrbek. Quantum turbulence visualized by particle dynamics. *Phys. Rev. B*, 90:014519, Jul 2014.
- [106] H. Schlichting. *Grenzschicht-theorie*. Braun, 1951.
- [107] T. Holtsmark, I. Johnsen, T. Sikkeland, and S. Skavlem. Boundary layer flow near a cylindrical obstacle in an oscillating incompressible fluid. *J. Acoust. Soc. Am.*, 26(1):102, 1954.
- [108] A. Bertelsen, A. Svardal, and S. Tjøtta. Nonlinear streaming effects associated with oscillating cylinders. *J. Fluid Mech.*, 59(3), 1973.
- [109] C. Y. Wang. Nonlinear streaming due to the oscillatory stretching of a sheet in a viscous fluid. *Acta Mech.*, 72(3-4):261–268, 1988.
- [110] S. K. Kim and A. W. Troesch. Streaming flows generated by high-frequency small-amplitude oscillations of arbitrarily shaped cylinders. *Phys. Fluids*, 1(6):975–985, 1989.
- [111] D. Schmoranzer, M. La Mantia, G. Sheshin, I. Gritsenko, A. Zadorozhko, M. Rotter, and L. Skrbek. Acoustic emission by quartz tuning forks and other oscillating structures in cryogenic ^4He fluids. *J. Low Temp. Phys.*, 163(317), 2011.
- [112] J. Bahyl. *Measurement of quantum turbulence in superfluid helium using second sound attenuation*. Comenius University, Faculty of Mathematics, Physics and Informatics, 2016.
- [113] D. Schmoranzer, M. J. Jackson, V. Tsepelin, M. Poole, A. J. Woods, M. Človečko, and L. Skrbek. Multiple critical velocities in oscillatory flow of superfluid ^4He due to quartz tuning forks. *Phys. Rev. B*, 94(214503), 2016.
- [114] D. Duda, P. Švančara, P. Hrubcová, M. La Mantia, and L. Skrbek. Experimentální studium stacionárního pohybu částic v supratekutém heliu v okolí rychle kmitající překážky – vliv velikosti oblastí. *31th Symposium on anemometry - proceedings*, 31:7–13, 2017.
- [115] P. Hrubcová. *Statistika kvantové turbulence v tepelném protuproudu supratekutého hélia 4 ve volném objemu, v blízkosti stěny a v blízkosti zdroje tepla*. Faculty of Mathematics and Physics, Charles University, 2018, in preparation.
- [116] L. Skrbek and W. F. Vinen. *The use of vibrating structures in the study of quantum turbulence*, volume 16 of *Progress in Low Temperature Physics*. Elsevier, 2009.
- [117] M. Človečko, E. Gažo, M. Kupka, M. Skyba, and P. Skyba. High quality tuning forks in superfluid $^3\text{He-B}$ below $200 \mu\text{K}$. *J. Low Temp. Phys.*, 162(5-6):669–677, 2011.
- [118] S. Balibar. Nucleation in quantum liquids. *J. Low Temp. Phys.*, 129:363, 2002.
- [119] D. W. Oxtoby. Homogeneous nucleation: Theory and experiment. *J. Phys-Condens. Mat.*, 4(38):7627–7650, 1992.
- [120] D. W. Oxtoby. Nonclassical nucleation theory: An exactly soluble model. *Phys. Scripta*, 1993(T49A):65–69, 1993.

- [121] R. D. Finch. Hole Theory of Cavitation Nucleation. *Phys. Fluids*, 12(9):1775, 1969.
- [122] M. Blažková, T. V. Chagovets, M. Rotter, D. Schmoranzer, and L. Skrbek. Cavitation in Liquid Helium Observed in a Flow Due to a Vibrating Quartz Fork. *J. Low Temp. Phys.*, 150:194, 2008.
- [123] M. Blažková, D. Schmoranzer, and L. Skrbek. On cavitation in liquid helium in a flow due to a vibrating quartz fork. *Fiz. Nizk. Temp.*, 34:380, 2008.
- [124] H.J. Maris, S. Balibar, and M.S. Petersen. Nucleation of Bubbles in Liquid Helium. *J. Low Temp. Phys.*, 93:1069, 1993.
- [125] A. Qu, A. Trimeche, P. Jacquier, and J. Grucker. Dramatic effect of superfluidity on the collapse of he 4 vapor bubbles. *Phys. Rev. B*, 93(17), 2016.
- [126] D. Duda, P. Švančara, M. La Mantia, M. Rotter, and L. Skrbek. Visualization of viscous and quantum flows of liquid 4he due to an oscillating cylinder of rectangular cross section. *Phys. Rev. B*, 92(064519), 2015.
- [127] M. Tsubota, T. Araki, and S. K. Nemirovskii. Dynamics of vortex tangle without mutual friction in superfluid 4he. *Phys. Rev. B*, 62(17):11751–11762, 2000.
- [128] C. F. Barengi and D. C. Samuels. Scaling laws of vortex reconnections. *J. Low Temp. Phys.*, 136(5-6):281–293, 2004.
- [129] A. C. White, C. F. Barengi, N. P. Proukakis, A. J. Youd, and D. H. Wacks. Nonclassical velocity statistics in a turbulent atomic bose-einstein condensate. *Phys. Rev. Lett.*, 104(7), 2010.
- [130] A. C. White, N. P. Proukakis, A. J. Youd, D. H. Wacks, A. W. Baggaley, and C. F. Barengi. Turbulence in a bose-einstein condensate. *J. Phys.: Conference Series*, 318(SECTION 6), 2011.
- [131] J. Schumacher, J. D. Scheel, D. Krasnov, D. A. Donzis, V. Yakhot, and K. R. Sreenivasan. Small-scale universality in fluid turbulence. *P. Natl. Acad. Sci. USA*, 111:10961–10965, 2014.
- [132] K. R. Sreenivasan and R. A. Antonia. The phenomenology of small-scale turbulence. *Annu. Rev. Fluid Mech.*, 29:435–472, 1997.
- [133] F. Toschi and E. Bodenschatz. Lagrangian properties of particles in turbulence. *Annu. Rev. Fluid Mech.*, 41:375–404, 2009.
- [134] A. Tsinober. An informal conceptual introduction to turbulence: Second edition of an informal introduction to turbulence. *Fluid Mechanics and its Applications*, 92:385–437, 2009.
- [135] E. J. Yarmchuk and W. I. Glaberson. Counterflow in rotating superfluid helium. *J. Low Temp. Phys.*, 36(3-4):381–430, 1979.
- [136] W. F. Vinen and J. J. Niemela. Quantum turbulence. *J. Low Temp. Phys.*, 128:167–231, 2002.
- [137] F. Toschi and E. Bodenschatz. Lagrangian properties of particles in turbulence. *Annu. Rev. Fluid Mech.*, 29(435), 2009.

- [138] M. S. Paoletti, M. E. Fisher, K. R. Sreenivasan, and D. P. Lathrop. Velocity statistics distinguish quantum turbulence from classical turbulence. *Phys. Rev. Lett.*, 101(154501), 2008.
- [139] S. Zuccher, M. Calvari, A. W. Baggaley, and C. F. Barenghi. Quantum vortex reconnections. *Phys. Fluids*, 24(125108), 2012.
- [140] D. V. Osborne. Second sound in liquid helium ii. *Proceedings of the Physical Society-Section A*, 64(2):114–123, 1951.
- [141] M. R. Smith, R. J. Donnelly, N. Goldenfeld, and W. F. Vinen. Decay of vorticity in homogeneous turbulence. *Phys. Rev. Lett.*, 71(16):2583–2586, 1993.